2022

MEMS based atomic scale 3D printer for nanofabri

BOSTON UNIVERSITY

COLLEGE OF ENGINEERING

Dissertation

MEMS BASED ATOMIC SCALE 3D PRINTER FOR NANOFABRICATION

by

RICHARD W. LALLY

B.S., Stonehill College, 1979
M.S., University of Southern California, 1986
M.S., Naval Postgraduate School, 1990

Submitted in partial fulfillment of the

requirements for the degree of

Doctor of Philosophy

2022

Approved by

First Reader

David J. Bishop, Ph.D.
Professor of Electrical and Computer Engineering
Professor of Physics
Professor and Division Head of Materials Science and Engineering
Professor of Mechanical Engineering
Professor of Biomedical Engineering

Second Reader

Alice E. White, Ph.D.
Professor and Chair of Mechanical Engineering
Professor of Materials Science and Engineering
Professor of Biomedical Engineering
Professor of Physics

Third Reader

Soumendra N. Basu, Ph.D.
Professor of Mechanical Engineering
Professor and Associate Division Head of Materials Science and Engineering

Fourth Reader

Uday B. Pal, Ph.D.
Professor of Mechanical Engineering
Professor of Materials Science and Engineering

Acknowledgments

I would like to start my acknowledgements with a sincere thank you to Professor David Bishop both for allowing me the opportunity to be part of your lab and for your constant support along the way. Your leadership style and the lab climate were an excellent fit for this old dog trying to learn new tricks.

I cannot say enough for all the support from the members of the Bishop Research Group, both past and present: Matthias Imboden, Han Han, Jackson Chang, Tom Stark, Lawrence Barrett, Jeremy Reeves, Diego Perez, Pablo Del Corro, Alex Stange, Corey Pollock, Josh Javor, Nick Fuhr, Ryan Yao, Geoffrey Van Dover, and Noelle Pierce. Even though we were not born in the same decade or generation, you treated me as any other valued member of the group. I learned a lot from each of you and I can only hope to pay it forward. Most of all, thanks for your friendship over the years.

The staff of the Photonics Center have all been invaluable in my research pursuit. In particular, the training and follow on problem solving of Paul Mak, Anlee Krupp, and Alexey Nikiforov were unwavering. You certainly made my research and academic growth possible.

I am indebted to my organic chemistry professor, Mary Alice Moore. Her personal challenge influenced me to be a life long learner and to fulfill a promise.

My parents were wonderful role models for me growing up. They provided me with everything I needed to be successful. I am at this point in my life because of them. Thank you, I hope this makes you happy.

I have been blessed with three wonderful daughters, who all now have their own families. Their lives have changed considerably since I started this program; however, what did not change was their endless support of me and my endeavors. I thank them and their families for working around my different pursuits.

Last of course, I must thank my wife Gina for always being there for me and the girls. Without you this, nor the many other things before it, would not have been possible. If patience is a virtue, then you must be the most virtuous person ever. Thank you for your boundless encouragement and support during this venture and all the ones before this. Here's to many days ahead sitting at the water's edge!

Rich Lally

MEMS BASED ATOMIC SCALE 3D PRINTER FOR NANOFABRICATION

RICHARD W. LALLY

Boston University, College of Engineering, 2022

Major Professor: David J. Bishop, Ph.D.
Professor of Electrical and Computer Engineering
Professor of Physics
Professor and Division Head of Materials Science and Engineering
Professor of Mechanical Engineering
Professor of Biomedical Engineering

ABSTRACT

Additive manufacturing is revolutionizing the aerospace, transportation, energy, healthcare and various consumer product industries, replacing centralized manufacturing plants with more localized fabrication. 3D printing has become ubiquitous within these industries for prototyping and production. Currently, the smallest 3D printed features are on the order of a micron. While sufficient for some academic and industry applications, nanoscale features are required for the electronics industry and research endeavors. Optical lithography is still the workhorse for industrial nanofabrication utilizing large expensive commercial foundries. Here, an atomic scale 3D printer is presented with many of the features found in a complex semiconductor fabrication plant. This process is reproduced using three separate die with microelectromechanical systems (MEMS), which are bonded together to create an integrated 3D printer with the capability to print at the atomic scale. Due to the micro-

scale size and surface areas of MEMS devices, they are extremely sensitive with rapid response times. These onboard MEMS devices replicate the functions of a thermal evaporator, patterning mask, mass sensor, heaters, temperature sensors and Van de Pauw setups. The assembled 3D printer dimensions are 3.8 mm x 2.5 mm x 1.8 mm (LxWxH) and it is therefore ideal for cryogenic environments. Quenched condensed thin film metals can be deposited using the atomic scale thermal evaporators in varying thicknesses up to approximately 50 nm. Replacing the atomic scale evaporators with micro scale evaporators, the deposited film thickness can reach 3.5 μm. Evaporated films are monitored during and after the deposition with the embedded MEMS devices. While this particular 3D printing assembly is designed for research-scale investigations, the same technology could be extended to wafer-scale 3D printing with high resolution, rapid throughput, and reduced cost.

Contents

List of Tables

List of Figures

List of Abbreviations

AC	Alternating current
AFM	Atomic force microscope
Ag	Silver
ALD	Atomic Layer Deposition
Au	Gold
BSE	Backside Etch
CPD	Critical Point Dryer
DC	Direct current
DRIE	Deep Reactive Ion Etch
FC	Flip Chip
FEA	Finite Element Analysis
FIB	Focused Ion Beams
FoC	Fab on Chip
GND	Ground
HF	Hydroflouric Acid
Hz	Herz
LCC	Leadless Chip Carrier
LHS	Left Hand Side
LIA	Lock-in amplifier
MEMS	Micro-electromechanical systems
MUMPs	Multi-User MEMS Process
Ni	Nickel
Pb	Lead
PCB	Printed Circuit Board
PLL	Phase-locked loop
PolyMUMPs	Polysilicon micromachining process
PSG	Phosphosilicate
PVD	Physical Vapor Deposition
PWM	Pulse width modulation
RHS	Right Hand Side
RIE	Reactive Ion Etch
RT	Room Temperature
SEM	Scanning electron microscope
SOI	Silicon-on-insulator
SOIMUMPs	Silicon-on-insulator micromachining process
UHV	Ultra High Vacuum
UV	Ultraviolet

Chapter 1

Introduction

1.1 Additive Manufacturing and Nanofabrication

There is a growing need for new materials to meet the challenges associated with emerging technologies [de Leon et al., 2021, Goh et al., 2022, Lin et al., 2019]. In particular, nanomaterials are a key to solving these challenges. Typically, one describes a nanomaterial as a structure that has one dimension that is between 1-100 nm. Currently, nanomaterials are in everyday products such as paints and fabrics, and more sensitive components, such as electronic devices, sensors and computer storage. Rapidly growing industries like healthcare, energy and environmental remediation are also supported with nanoscale materials. These nanomaterials have unique features due to their increased surface area and aspect ratios. Many nanomaterials display enhanced electromagnetic, optical, thermal and mechanical characteristics than their bulk material counterparts [Wu et al., 2020].

Creating nanomaterials tends to bifurcate into bottom-up and top-down approaches [Imboden and Bishop, 2014, Zhang et al., 2004, Isaacoff and Brown, 2017, Oh et al., 2021]. The bottom-up approaches are biologically inspired, with complex systems and organisms arising from a set of rules at the local level that allow the fundamental elements to self-assemble. While capable of creating systems of great complexity (human beings, for example), the rules are highly complex and our understanding of how to do this is only slowly emerging. This is a high entropy solution to the problem.

The alternative approach, based on how we manufacture integrated circuits, is top-down. In this approach, we have deterministic control over the structures and devices and completely specify what goes where and what it does. This approach endeavors to reduce the effects of entropy to zero, completely controlling where everything goes and minimizing the effects of randomness to as great an extant as possible. While Moore's law has proven to be an excellent guide for circuit fabrication, current industrial fabrication techniques limit this trend [Moore, 2006, Burg and Ausubel, 2021]. Typical fabrication procedures involve either depositing or growing metal films that use complicated multi-step patterning by either optical or e-beam lithography. These top-down approaches have been extremely reliable for structures down to the tens of nanometers [Ito and Okazaki, 2000]. However, in order to continue the Moore's Law trend, new approaches must be identified which can pattern structures at the atomic scale. Several bottom-up approaches have been identified which offer the advantage of resist-free patterning. Many of the other additive approaches require a complex positioning system such as scanning probe lithography [Garcia et al., 2014]. Such complex positioning systems limit the integration of these techniques with other systems, the materials that can be deposited, and the rate of production. While static stencils can also provide patterning and a high rate of production [Wasserman et al., 2008], they limit the geometric patterns that can be produced.

Additive manufacturing in the form of 3D printing has been successfully integrated into the manufacturing process during the past decade. Aerospace, transportation, medical, energy, and consumer products industries all use 3D printing in their prototyping and production of products. Due to its high-speed, low cost and environmentally friendly parameters, 3D printing is a logical choice for new technologies and

products. Currently, the finest resolution of 3D printing is approximately 2 microns with promising technologies on the horizon to enhance that resolution [Vyatskikh et al., 2018, Wen et al., 2021]. While adequate for large scale components, the electronics industry requires orders of magnitude better. The manufacturing standard for electronic circuits remains optical lithography with resolution of 10's of nanometers, high throughput and low cost. Concurrently, advances in additive manufacturing have slowly captured more production market share with additional types of materials that can be quickly printed with higher resolution and lower costs. It seems a natural progression to apply this same 3D printing principle to nanoscale fabrication.

Matter is composed of atoms and atomic scale 3D printing is a universal and highly sought after goal by the researchers in this field [Jesse et al., 2016]. Hence, the ultimate nanomaterial goal for 3D printing is the ability to deposit any atom, anywhere, anytime with high speed. Such a printer would allow one to build any structure or device one wishes, even metastable crystalline structures or molecules that naturally occur via normal kinetic pathways. This will enable additive manufacturing to move beyond building items we already know about at high speed and low cost and begin to explore structures that chemistry cannot produce.

The motivation and emphasis of this dissertation is to demonstrate the construction of just such an atomic scale 3D printer. An overview of the design and fabrication of die that make up the atomic scale 3D printer is discussed in the remainder of this introduction.

1.2 Micro-electromechanical Systems (MEMS)

MEMS is a process technology using integrated circuit techniques to create integrated devices that combine mechanical and electrical components [Judy, 2001]. The technique uses the integrated electronic circuit manufacturing process and adds a micro-machining process to etch away layers to form MEMS structures. Typically, a silicon wafer is used as the substrate. Bulk micromachining can be performed to etch away large sections of the silicon base. Surface micromachining creates the structures on top of the silicon wafer by adding single feature layers one at a time. Clean rooms with specialized, expensive equipment and a great deal of time are required to create MEMS devices at the research level. At the production level, the fabrication facilities or foundries are completely automated with similar, but more expensive equipment and refined processes. Due to the automated processes, the time and cost per device is insignificant.

The MEMS components can range from a few microns to a few millimeters. The advantages of MEMS devices are their small size and mass, low power consumption, low cost, high frequency capability, small thermal constant, high reproducibility, vibration resistance, and large parallel batch processing. Some disadvantages include the increased cost for design and research applications, required expensive equipment and knowledge base, and polysilicon's brittleness. Based on the advantages noted, MEMS devices created by this technology are therefore excellent sensors and actuators. Sensors measure a force or energy that is translated into an electrical signal. Actuators convert an electrical signal into action. Due to the micrometer size of these sensors they are very sensitive and can measure with a high degree of resolution. Likewise, owing again to their size, MEMS actuators present extraordinary precision in movement. Therefore, MEMS devices are ideal candidates for research that involves

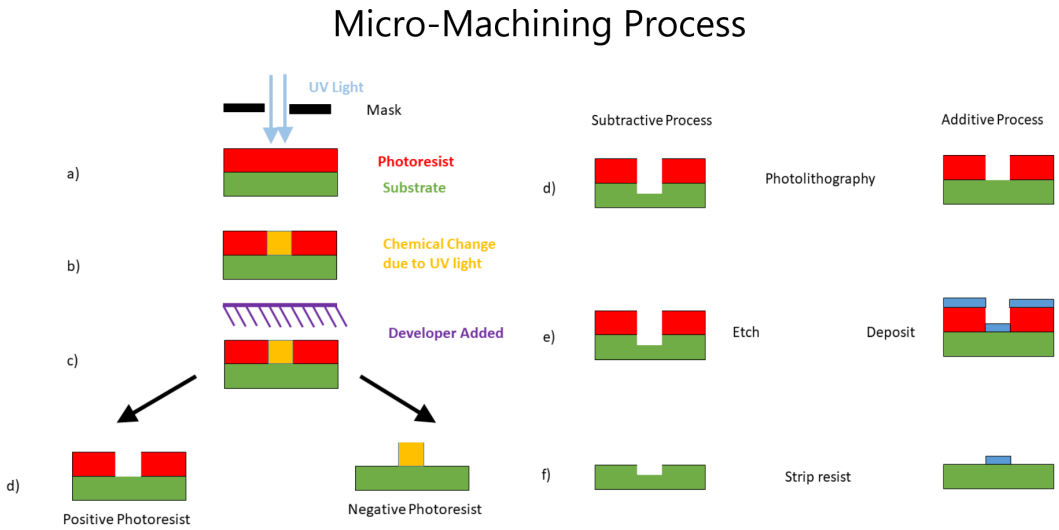

Figure 1·1: Micro-machining process showing on the LHS the photolithography steps and on the RHS is the additive or subtractive processes.

the accuracy and sensitivity of these devices [Bell et al., 2005]. Our atomic scale 3D printer is a system of micro-electromechanical systems. The embedded MEMS devices on the three die set that make up our 3D printer are a collection of various sensors and actuators. The actual process of design and fabrication of these die will be described in the next sections.

1.3 MEMS Fabrication Process

As discussed earlier photolithography is still one of the most relied on processes for integrated circuit and MEMS device production. In the case of MEMS devices, surface micro-machining remains a heavily used process to produce MEMS features. Most MEMS devices require multiple layers of micro-machining to form the desired device [Mamilla and Chakradhar, 2014]. Each layer requires multiple steps. For illustration, the steps of one such layer are presented in Figure 1·1. MEMS lithography

refers to patterning a photosensitive polymer (photoresist) by exposing a masked or unmasked portion with ultraviolet light (UV). Therefore, the first step is to spin a layer of photoresist on the silicon substrate. Next, a mask is positioned over the substrate and exposed with UV light (Figure 1·1a). The exposed region of photoresist undergoes a chemical reaction (Figure 1·1b) and can then be stripped away using a developer solution (Figure 1·1c) . Depending on the application, there are two types of photoresist, positive and negative. Figure 1·1d demonstrates the outcome from each of these types of resists. At this stage of preparation, the substrate with patterned photoresist is ready for either a subtractive or an additive process. Using the positive resist outcome Figure 1·1d, the substrate with photoresist can be subjected to a Reactive Ion Etch (RIE) plasma which selectively etches the exposed silicon layer. After the etching process, the remaining photoresist can be stripped with a chemical treatment leaving the feature in Figure 1·1f. Similarly, the additive process starts again with Figure 1·1d. Depending on the type feature required, the desired metal, polysilicon or silicon oxide can be deposited on both the photoresist and the exposed substrate. Once again, the photoresist is stripped off with a chemical treatment. In this case, the photoresist removal also removes the deposited material attached to the photoresist (Figure 1·1f). This pattern transfer process is commonly referred to as the lift-off method. For MEMS devices in the atomic scale 3D printer, many layers must be created each with precision, reproducibility, and within a reasonable timeframe. Therefore, instead of creating these devices locally, a Multi-User MEMS Process (MUMPs) is employed. MUMPs are processes used by commercial foundries which fabricate MEMS devices for multiple users simultaneously using identical design rules. The result are MEMS devices, which are reliably, rapidly, and cheaply produced [Esashi, 2021].

The PolyMUMPs process by MEMSCAP, Inc. is a noted MUMPs that provides cost effective, proof of concept MEMS fabrication to universities, industries, and governmental laboratories [Cowen et al., 2013]. Specifically, this process has eight different masks and offers seven layers, including two structural and two sacrificial layers. Each layer has standardized thicknesses and minimum design features (2 μm). The user patterns each layer following the design rules using a hierarchical physical layout editor software. One disadvantage to the PolyMUMPS process is the lack of flexibility in the amount, type and order of layers. Additional micromachining must be performed by the user locally if additional features or functionality are necessary that cannot be achieved with the standard process. A brief description of each layer and the various available options follows.

The PolyMUMPs process begins with a 150mm n-type (100) silicon wafer that is approximately 600 μm thick and is highly doped with phosphorus. The first layer deposited is 600 nm of silicon nitride forming a layer that is electrically insulated from the substrate. The second deposited layer is 500 nm of polysilicon (designated the poly 0 layer), which is masked and then etched according to the user submitted pattern. The third layer consists of 2.0 μm of phosphosilicate glass (PSG) creating the first sacrificial oxide layer. The sacrificial layers will later be removed by the user to free the polysilicon MEMS structures. This sacrificial layer can also be patterned with dimples (small 750 nm deep holes etched into the oxide) or an anchor hole allowing connection between the Poly 0 layer and the Poly 1 layer. The fourth layer (Poly 1 layer) is another layer of polysilicon which is 2.0 μm thick and forms the first structural layer. Layer five is the second sacrificial oxide layer which is 750 nm thick. This oxide layer can also be patterned. With the ANCHOR2 pattern both oxide layers are etched away and the POLY1-POLY2-VIA pattern allows a direct connection

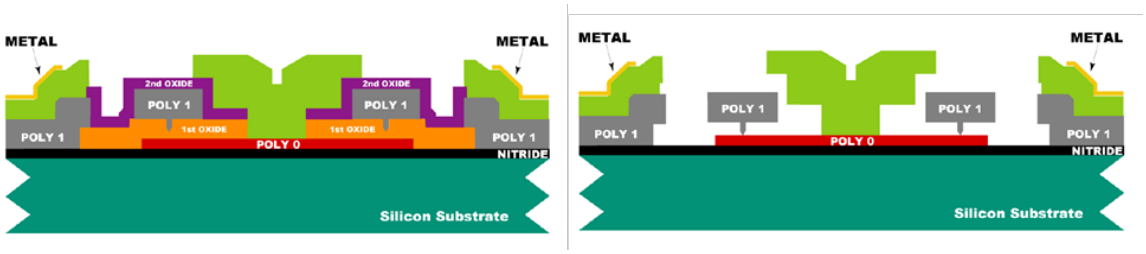

Figure 1·2: MEMSCAP PolyMUMPs process illustrating the mechanical and sacrificial layers of polysilicon (on the LHS) and the removal of the sacrificial silicon oxide. [Cowen et al., 2013]

between the Poly 1 and Poly2 layers. The sixth layer (Poly 2) is the second and last structural layer of 1.5 μm of polysilicon. The seventh and last layer of the process is a 500 nm metal layer used for connecting electrically, bonding, probing and reflective mirrors. Each of these layers require multiple steps with depositing, patterning mask and etching. The surface of the die is then coated with a layer of photoresist to protect the micro-machined features from damage during shipment, handling, or additional processing. Figure 1·2 demonstrates how the various layers are patterned: the left hand side shows the patterned layers with the sacrificial layers; and right hand side is when the MEMS device has been released and the sacrificial layers have been removed.

Using the PolyMUMPs process has numerous advantages over the alternative. In each production run, MEMSCAP fabricates up to 16 user unique designs on the 2.5 cm x 2.5 cm space available to the subscriber. Fifteen identical copies of the 2.5 cm x 2.5 cm design are sent to the user. Available production runs typically occur every 2-3 months. Consequently, the user can concentrate on the design and characterization of the received devices rather than the fabrication. PolyMUMPs has proved to be effective, responsive, and reproducible process that is ideal for rapid prototyping of MEMS devices.

1.4 Design Concept of the Atomic Scale 3D Printer

The design of an atomic scale 3D printer requires essentially three things: a material with a dispensing system, a positioning system, and print bed [Shakor et al., 2019]. Similarly, a nanofabrication process needs an evaporation method, a patterning system, and a substrate. Therefore, an atomic scale 3D printer could be interchangeable with a Fab on a Chip (FoC) when referring to nanofabrication. Throughout the remainder of this thesis, these terms will be referenced with similar characteristics and functions. Ultimately, this atomic scale 3D printer is replicating the functions found in a large scale foundry. There are MEMS devices that can perform material deposition, patterning with a reusable mask, mass sensor, temperature sensor, heaters, and substrate for deposited material with film diagnostic electrical connections. The idea of creating a FoC was first formed in 2014 [Imboden et al., 2014a] and a number of successive MEMS technologies have made this possible [Imboden et al., 2017]. Essentially, the FoC functions are laid out onto three PolyMUMPs fabricated die. Each die has a unique function as typically found in a 3D printer design.

Figure 1·3 provides the conceptual arrangement of the atomic scale 3D printer with the appropriate functions of a FoC. In fact, one could view this as an upside down 3D printer where the materials emanate from the bottom die and are patterned on the top die. The bottom die is referred to as the source die. Here, heater plate like MEMS devices evaporate metals upward toward the middle die. The middle die is referred to as the writer die or dynamic mask and is responsible for patterning the evaporant. This is made possible by etching a large opening through the back of the writer die exposing the moveable writer plate. An aperture created in the writer plate allows the evaporated material to reach the top die. The last die, known as the target die, is where the patterned material is deposited. The target die incorporates

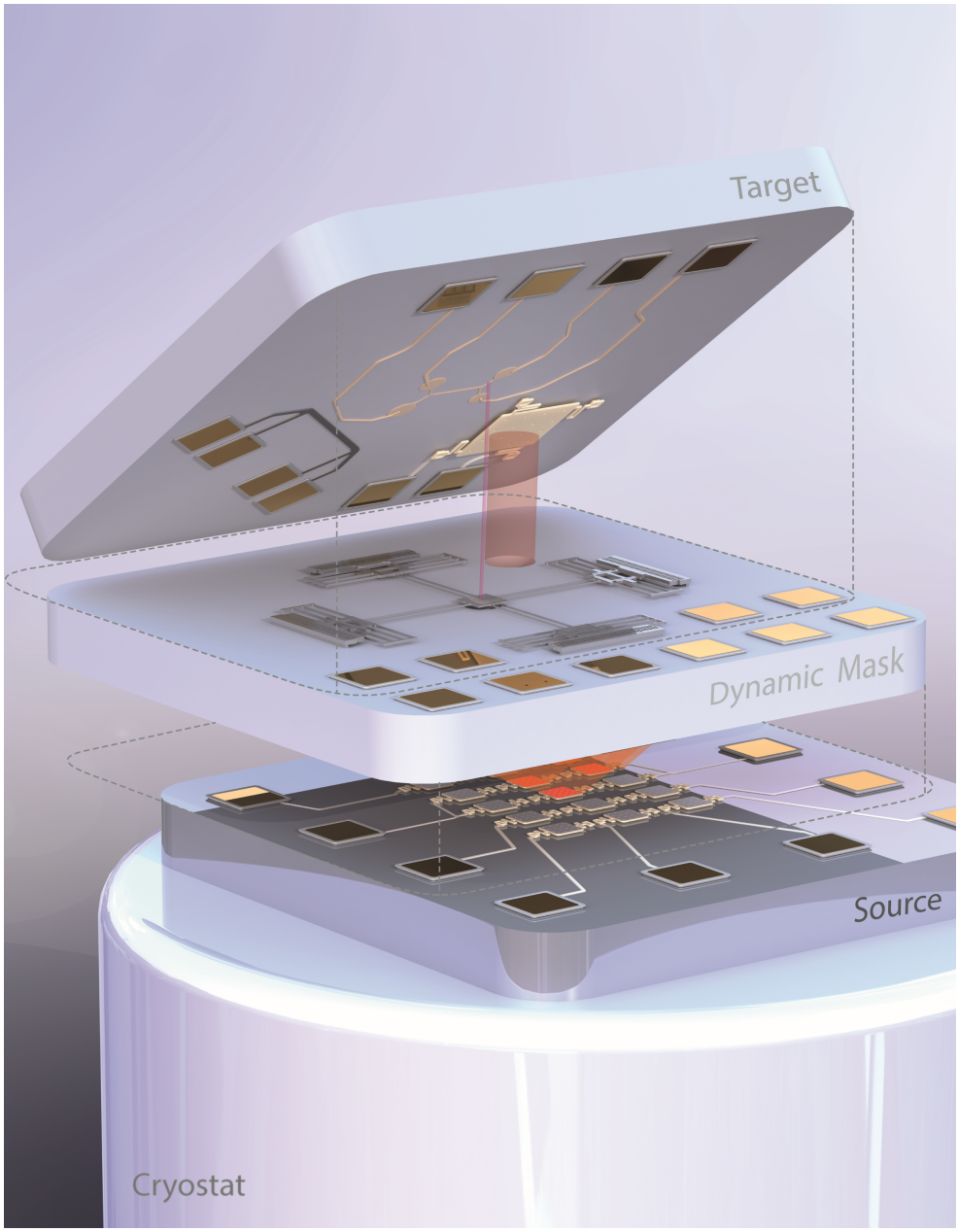

Figure 1·3: Shown is the high level concept for our atomic scale, 3D printer. It consists of three layers, each a separate silicon die. The bottom layer is the atom source layer that produces the atoms for writing. The middle layer is the dynamic mask lithography tool that determines where the atoms land and the top layer is the target die upon which we write.

.

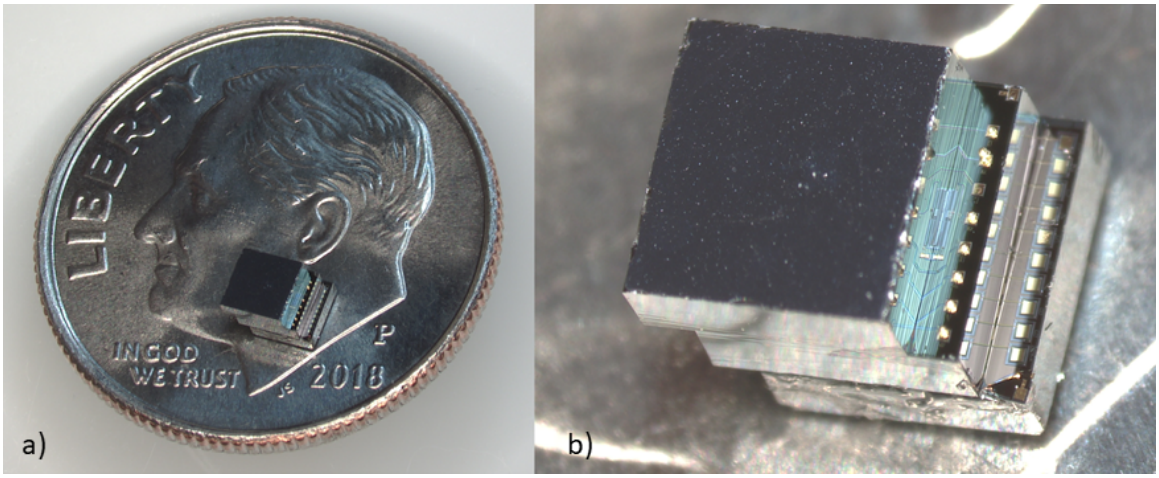

Figure 1·4: Optical images of Atomic Scale 3D Printer: (a) Image showing the scale of FoC. (b) Close up image of FoC.

a mass sensor, temperature sensor and electrical leads. Each of the three die are created separately using the PolyMUMPs process, then further functionalized, and later assembled. With these three stacked dies we are able to reproduce the foundry fabrication process. One of the particularly important advantages of the atomic scale 3D printer is the extremely small footprint. Figure 1·4 shows the scale of a fully assembled printer in comparison to a dime. With single millimeter dimensions, this atomic scale 3D printer can be adapted for unique applications and easily used in cryogenic environments for in situ measurements. The films and structures created by the atomic scale 3D printer are at the nanometer scale and are therefore influenced by quantum effects [Słowik et al., 2016]. In this regard, MEMS devices have been particularly useful in investigating quantum effects such as the Casimir force [Stange et al., 2019].

The remainder of this work will provide an in depth discussion of each die, the processing and assembly of the atomic scale 3D printer, and results from the 3D printer. The last section will summarize this work and provide an outlook on what the future may hold for nanofabrication.

Chapter 2

Micro Source Evaporator

2.1 Source Design

In this section, the atomic source die design and characteristics are discussed. As described earlier the atomic source die is a MEMS device fabricated using the MEMSCAP PolyMUMPS process. The purpose of this die is to provide a system that can evaporate various metals and nonmetals using a Physical Vapor Deposition (PVD) method. The two most widely used PVD methods are thermal and e-beam depositions. Creating an e-beam evaporator for this application would be impractical based on the size and required materials and electronics; hence, the thermal evaporator is used. Thermal evaporation, as the name suggests, uses resistive heating of a crucible to evaporate the material contained inside the crucible. When depositing these films using this method, it must be accomplished in high vacuum. The removal of air molecules from the evaporating chamber allows for a longer mean free path for the depositing material. Consistent with conventional thermal PVD, a thermal evaporator can be formed using the PolyMUMPS method without any additional processing [Han et al., 2015]. The original micro source (also referred to as an atomic scale source, since small numbers of atoms, as you will see, can be controllably evaporated by the source) was designed with a 50 μm x 50 μm x 1.5 μm plate suspended by two small springs, all fabricated from the polysilicon 2 layer. Since the springs are 2 μm wide and 1.5 μm thick, this constriction adjacent the plate causes Joule heating when a direct voltage is applied. Figure 2·1 shows a single source plate with

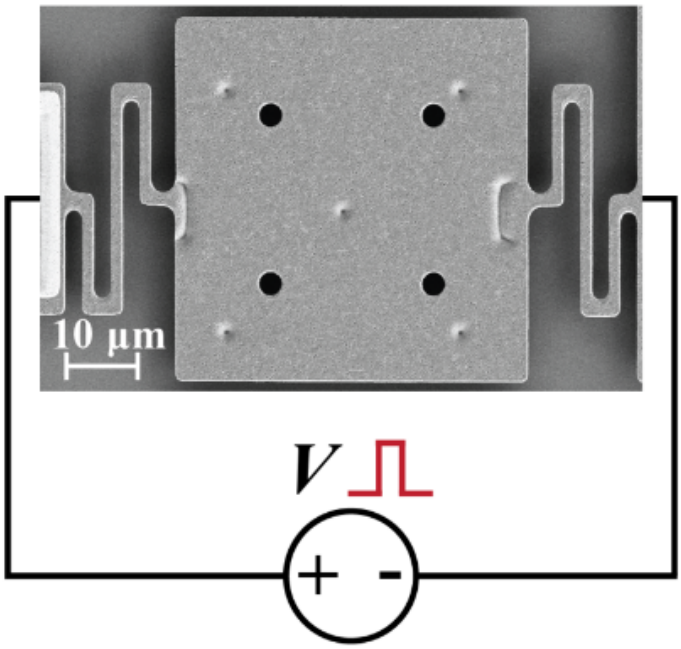

Figure 2·1: SEM image of individual source plate and the related circuitry. Reproduced from [Han et al., 2015] with permission from the Royal Society of Chemistry.

its associated heater springs. The serpentine design of the springs also allows for the expansion when heated and reduces the possibility of failure from fracture. Earlier designs with straight, constricted connecting leads to the plate did not survive the thermal expansion that occurred when higher voltages were applied. However, the current spring configuration is capable of exceeding 1200 K without spring failure. A conventional PVD process is used to deposit metals on the source plates. We use both thermal and e-beam evaporation to load the source plates typically at rates of 2 angstroms per second or less. Before loading any metals onto the source die, a 20 nm layer of Al_2O_3 is first applied. This sapphire layer protects the polysilicon source plate from the deposited metal, reducing the formation of silicides at higher temperatures. Many metals with low melting points such as Pb, In, and Sn do not require this layer. However, metals such as Au, with a much higher melting temperature, may require the replacement of the Al_2O_3 with a layer of Tungsten. Individual source plates can

be formed into an array of source plates as illustrated in figure 2·2. Source arrays provide increased amounts of source material for sufficient deposition thickness of the metal. Source arrays can be formed with each source plate having a unique electrical connection. This allows each source plate to be individually controlled. By using a shadow mask individual source plates can be loaded with different metals. This results in the ability to deposit multiple metals either sequentially or simultaneously.

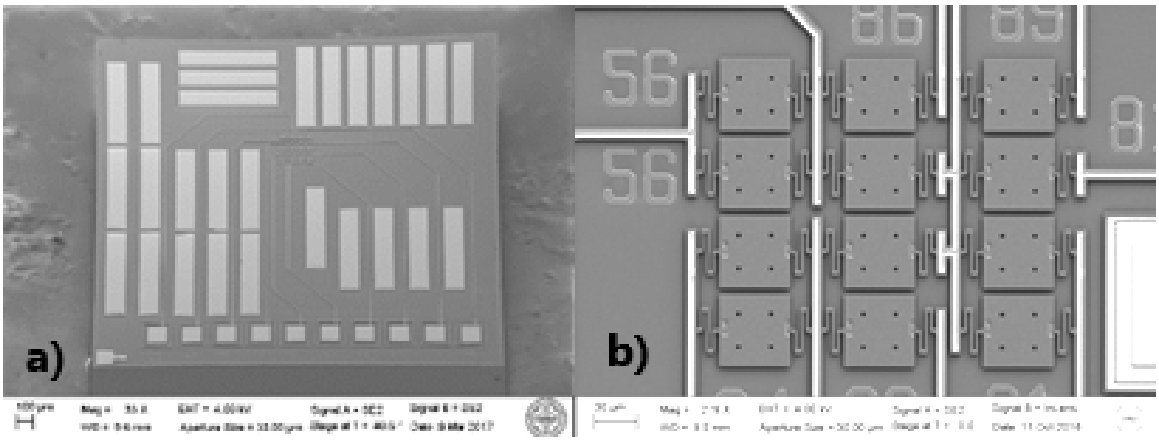

Figure 2·2: Source array. a) SEM image of source die and bonding pads. b) Close up image of source array.

2.2 Source Characterization

Finite Element Analysis (FEA) of this source plate design has shown that the heaters provide uniform heating across the source plate. The FEA is depicted in Figure 2·3 [Han et al., 2015]. Here, thermal energy is added symmetrically to both heaters until an equilibrium temperature is reached. Finite element simulations indicate that above 1000 K radiation effects become more and more significant.The dependency of thermal radiation density is given by the Stefan–Boltzmann law, equation 2.1, where j is the total energy radiated per unit surface area, σ is the Stefan-Boltzman constant,

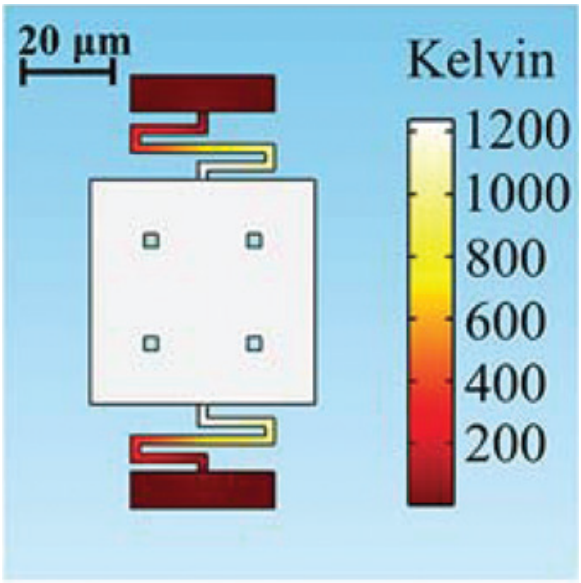

Figure 2·3: FEA simulation of heater. Reproduced from [Han et al., 2015] with permission from the Royal Society of Chemistry.

and T is the body's thermodynamic temperature.

$$j = \sigma T^4 \tag{2.1}$$

Since in this equation the temperature is raised to the fourth power, the temperature uniformity is improved across the plate. When the plate is heated to 1300 K the thermal uniformity of the plate changes by as little as 1 K [Han et al., 2015]. You can also see in the simulation the uneven heating across the length of the connecting springs. Over a distance of ≈ 60 μm the spring rises from a base temperature to over 1,200 K. This FEA model is confirmed using a thermal camera images shown in Figure 2·4. A sweep of voltage up to 3 V shows resistive heating first in the springs and then a consistent temperature across the plate. Notice, also that the heat is dissipated primarily by thermal conductance to the substrate. When a single source is heated as depicted in figure 2·4c, none of the surrounding plates or adjacent substrate area are appreciably heated. As will be discussed, these micro sources use small amounts

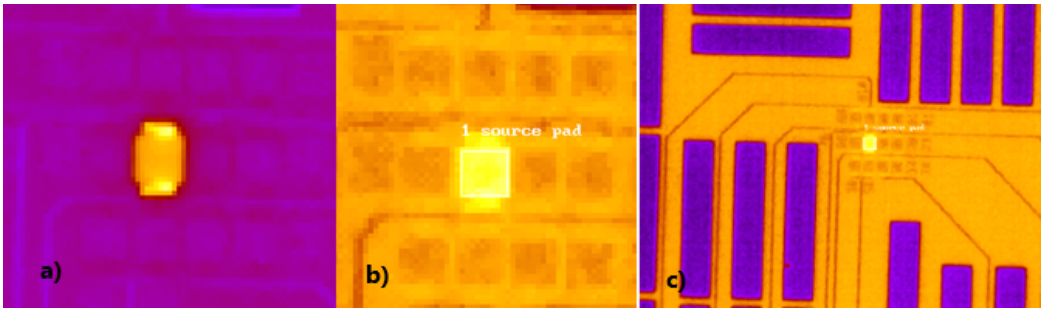

Figure 2·4: Thermal camera images of heater plate. a) Springs show increased heat. b) Uniform heating of plate. c) Individually heated plate causing minimal heating to adjacent plates.

of power. Thus, this leaves the substrate cool, even though only a few microns away, the springs and plate remain hot. With the inclusion of the flexible springs that are 1.5 μm thick, these sources are very robust and can be continuously heated or pulsed thousands of times [Han et al., 2015]. While technically the source die is reusable, it is unlikely a source die would be reused due to deposited material residue and handling damage when dismantling. Typically, various amounts up to 500 nm of a metal are deposited on the source plates. In this condition when the source plate is heated the entire amount of metal can be evaporated. The atomic flux from the source can be estimated with the Hertz-Knudsen equation 2.2

$$j \approx \frac{mP_{vap}(T)}{\sqrt{2\pi mkT}} \tag{2.2}$$

where m is the atomic mass, k the Boltzman constant, T is the temperature, and $P_{\mathrm{vap}}(\mathrm{T})$ is the temperature dependent vapor pressure [Hołyst and Litniewski, 2009] This temperature dependent vapor pressure proves to be an important variable for the metal evaporation since according to a simplified version of the Clausius–Clapeyron equation 2.3 [Barrow, 1953], a small increase in temperature has a significant increase in the vapor pressure.

$$\ln(P_{\mathrm{vap}}) = A - \frac{B}{T} \tag{2.3}$$

In equation 2.3, A and B are empirical constants. This allows the source plate to control the evaporation rate of metals with minimal temperature change resulting in low power consumption [Han et al., 2015]. Reviewing figure 2·5, finite element simulation of the source's mechanical deformation due to thermal expansion [Han et al., 2015] demonstrates again the non-uniform heating of the springs. The stress incurred across the spring length is similar to that of figure 2·3. However, this stress causes the spring to deform and the plate to be tilted on the order of 200 nm for the 50 μm x 50 μm x 1.5 μm plate. When depositing $\approx$ 500 nm of material this tilting has minimal effect in the deposition process or the amount of material deposited. This does become a factor when larger source plates are incorporated and more material is loaded on the plates, which will be discussed later. The source plates use a voltage

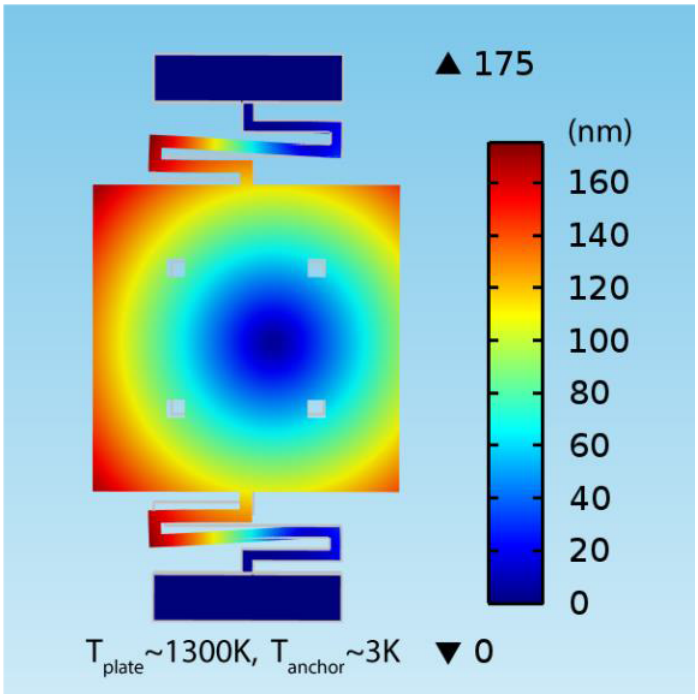

Figure 2·5: Finite element simulation of the mechanical deformation due to thermal expansion of the source. Reproduced from [Han et al., 2015] with permission from the Royal Society of Chemistry.

bias to prevent heat runaway due to the non-Ohmic behavior of the polysilicon.

Figure 2·6 [Han et al., 2015] is a graph of applied voltage with the resulting current and recorded resistance. Where the resistance and current lines intersect, the source becomes unstable. Also shown in the RHS of figure 2·6 is the power consumption for this measurement. Using the voltage bias minimizes the power consumption and brings the source to thermal equilibrium quickly and efficiently. As mentioned earlier,

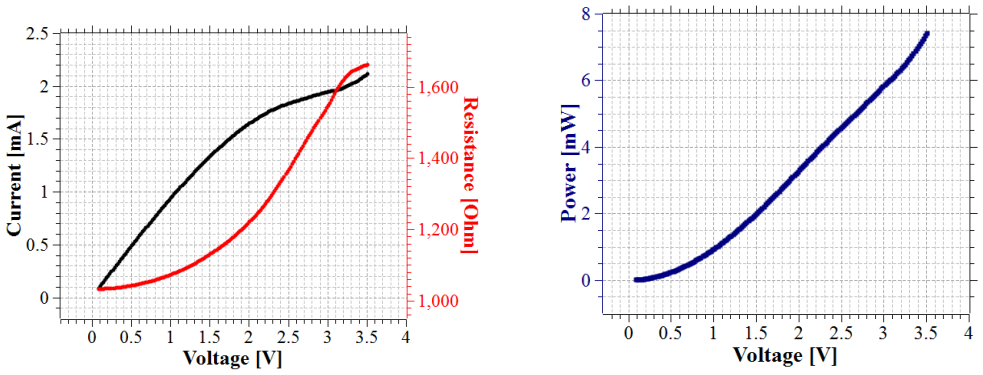

Figure 2·6: Voltage Sweep of Source Plate: LHS shows the current and resistance from a voltage sweep from 0 - 3.5 V, RHS shows corresponding power during the voltage sweep. Reproduced from [Han et al., 2015] with permission from the Royal Society of Chemistry.

due to the microscale size of the source, it has a rapid thermal response to a voltage basis. In figure 2·7 one can see the response time for these source plates has been estimated to be about 5 ms [Han et al., 2015]. In this figure you can also see the latent heat of melting the metal (Ag) reduces the response time by an additional 10 ms. This is an important criteria when metals are loaded onto the plate in various thicknesses. Even at 15 ms this is still a rapid response rate of the source plates. This charateristic allows the sources to be pulsed rather than just continuously heated. While a shutter could be used to control the atomic flux on the substrate, pulsing can also control the amount of material deposited while limiting the power consumed. Pulse Width Modulation (PWM) with these sources significantly reduces the power and is suitable for low temperature environments. Using a MEMS mass sensor, various pulse widths

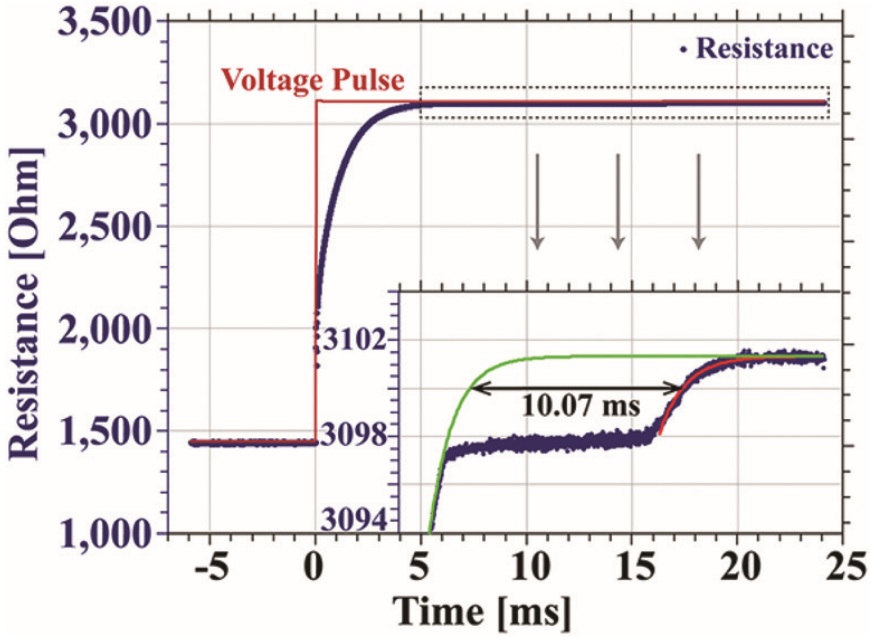

Figure 2·7: Thermal response time of the source plate with an insert showing the latent heat of depositing silver. Reproduced from [Han et al., 2015] with permission from the Royal Society of Chemistry.

and amplitudes have been recorded with this source plate configuration (figure 2·8) [Han et al., 2015]. Converting the frequency shift in the mass sensor provides the

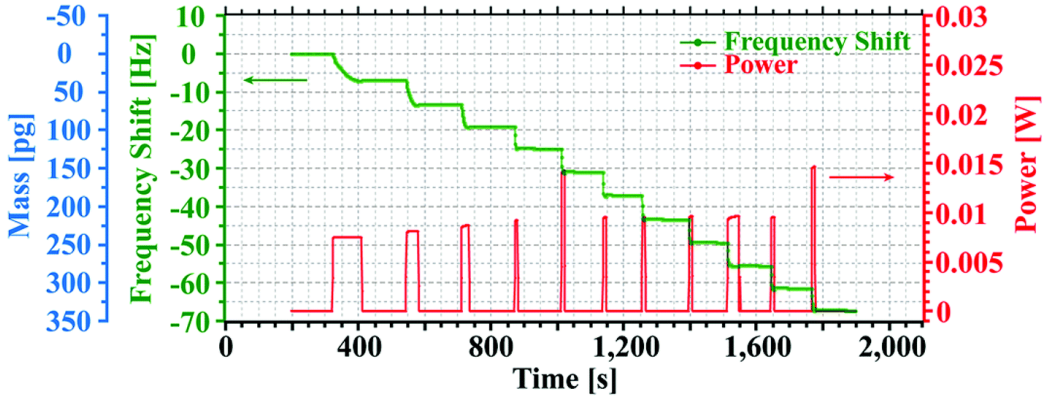

Figure 2·8: Graph of micro source pulses corresponding to mass and power measurements. Reproduced from [Han et al., 2015] with permission from the Royal Society of Chemistry.

amount of mass deposited. Eleven pulses are graphed with pulse widths between 9

and 90 seconds using around 10 mW. In addition to limiting the power consumption, controlling the PWM and bias voltage can precisely moderate the atomic flux rate and determine the amount deposited. Further results show (Figure 2·9) [Han et al., 2015] that the source plates can deposit materials over seven orders of magnitude and by manipulating the pulse width and voltage so that the desired evaporation rates and mass amounts can be achieved. Providing continuous voltage allows one to

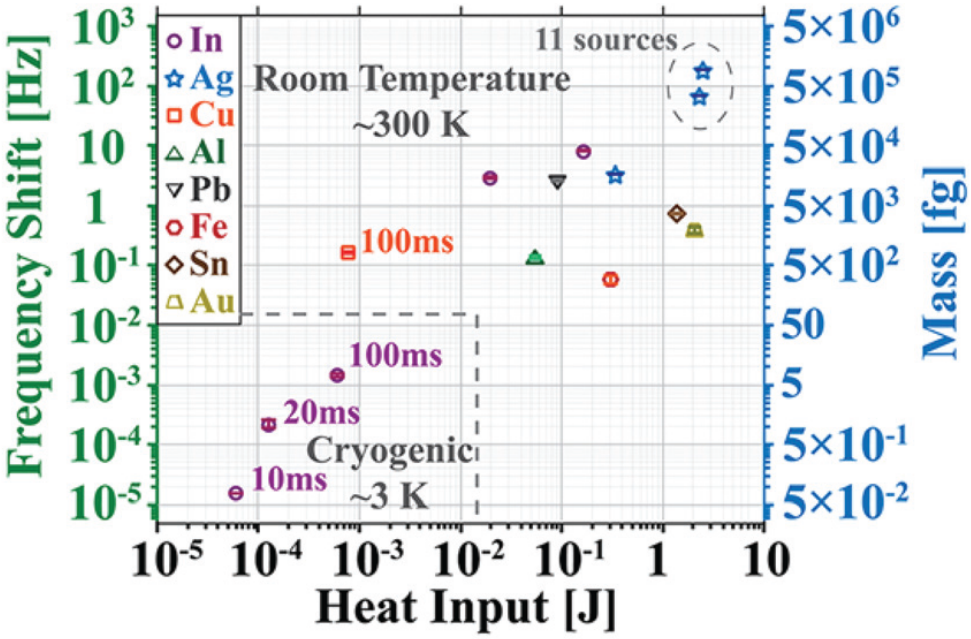

Figure 2·9: Graphs of metal depositions Illustrating the minimal heat required for deposition. Reproduced from [Han et al., 2015] with permission from the Royal Society of Chemistry.

deposit a large amount of materials quickly but results in higher power and thermal considerations. The micro-scale size of the source plates using PWM reduces the amount of power making small amounts of atoms deposition possible and suitable for a cryostat environment.

2.3 Alternative Source Designs

After characterization of the source plates, there were a number of design changes which are required to facilitate its use in a 3D atomic scale printer. These design changes will be discussed throughout the rest of this section. When the source plate is loaded with a small amount of metal < 150 nm, the metal tends to evaporate completely off the plate. Plates with loaded metals thicker than this may tend to form metallic spheres on the plate. Since the springs are also exposed during the loading of the metal onto the source plate, the springs are also covered in a film of metal. The metal on these springs, since they are heated first, also forms spheres. These spheres can reduce the effectiveness of the plate as a heater. The metal spheres can short out the applied current, as the resistance of the spring is much higher than that of the metal. The spheres on the springs can also act as a thermal short, increasing the power usage and reducing the precision of the amounts being deposited. A couple of methods were applied to resolve this issue. The first method integrates a mask into the PolyMUMPs design. In figure 2·10 [Han et al., 2015], a shadow mask was patterned to cover each source plate. When the plate is released, Au bimorphs raise the shadow mask structure off of and about 10 μm above the source plate. This design keeps the springs free of deposited metals during the load sequence. There are also a couple of disadvantages to this design. By adding the bimorph structures, the possible connection geometries to the source plates are reduced. The size and length of the bimorph can also interfere with other features on the source die or with the backside of the writer die. However, as a standalone die, this is an effective and simple method for eliminating the formation of spheres on the heaters.

Another solution for isolating the heaters from metal deposits during the loading process is to use a customized traditional shadow mask. A Ni shadow mask was cre-

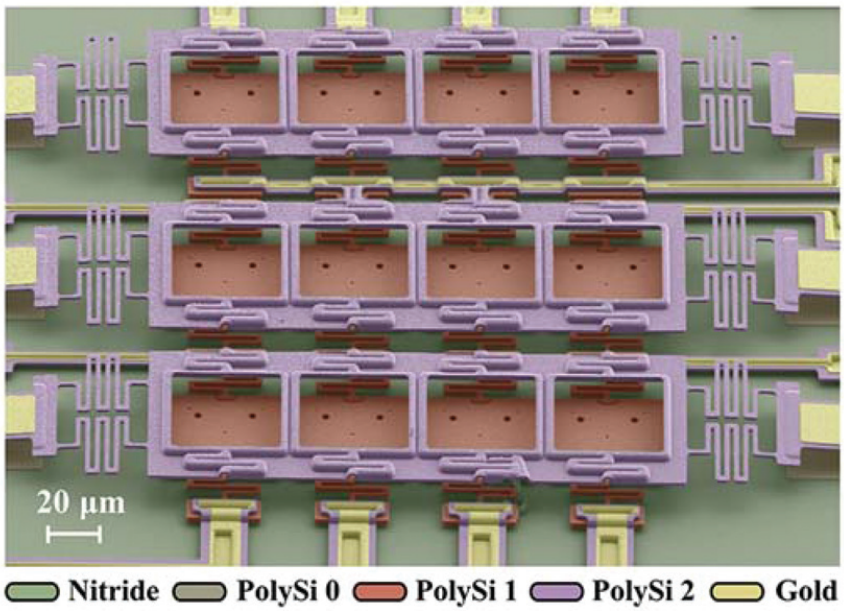

Figure 2·10: Colorized SEM image of source array with integrated mask using bimorphs. Reproduced from [Han et al., 2015] with permission from the Royal Society of Chemistry.

ated specifically for this application. This reusable mask after alignment covers the springs while leaving the plates accessible for the metal deposition. The advantage to the Ni mask over the bimorph approach is that depositing metal onto the source die goes only on the plates. This means the ball bonding pads, electrical leads, and area surrounding the plate are not covered with metal. Masking the ball bonding pads is important since forming a ball bond through the deposited metal onto the Au ball bond pad is often difficult to impossible. The biggest disadvantage to the Ni mask usage is proper alignment. Perfect alignment with the assistance of a probe station is challenging depending on the number of plates being masked. Another necessity for this Ni mask method is a proper standoff mechanism on the die substrate to maintain separation distance above the source plates.

The standoff mechanism for the source die is a column of stacked PolyMUMPs layers

as depicted in figure 2·11. Here, both silicon oxide layers are encapsulated with the

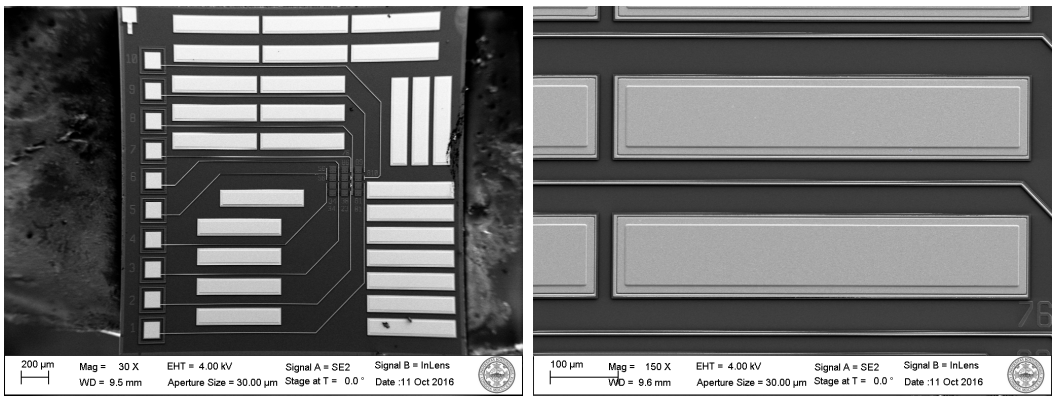

Figure 2·11: SEM images of source standoffs seen as the light colored rectangles. Standoffs prevent damage to source plates and electrical leads.

Poly 1 and 2 layers. The resulting stack of layers is 6.75 μm above the nitride layer. This height provides a 2.5 μm separation from the top of the standoff column to the top of the source plate surface as seen in figure 2·12. There are multiple standoff

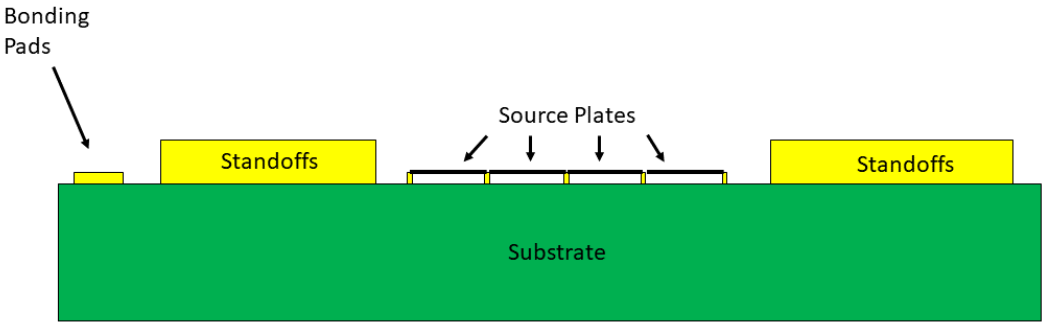

Figure 2·12: Diagram showing the side view of a source die with standoffs.These standoffs are designed to be higher than the source plates to protect them from damage during preparation and assembly of the die.

columns surrounding the plates and along the edges of the dies. These columns pro-

tect the source dies as discussed above when a Ni shadow mask is being aligned. The columns are very robust with their Au caps and can handle the agitation accompanying an optical alignment of the shadow mask. The standoff columns also protect the electrical Au leads that connect the source plate springs to the Au bonding pads. Lastly, the standoff columns along the edges, act as retaining walls to prevent the cyanoacrylate adhesive from wetting between the source die and the writer die and seeping onto the source die. The placement of each of these columns has been maximized to reduce the damage to the critical elements of the source die and they are effective in doing so.

As outlined in the introduction, this atomic scale 3D printer is able to evaporate different metals or materials using these source plates. The goal of being able to print Josephson Junctions or fabricate combinatorial materials, therefore, requires a minimum of two different materials. With the proper masking techniques, two or more metals can be loaded and then evaporated. Redesigning the source die for the evaporation of two metals resulted in the array in figure 2·13. In this array, the six source plates at the top of the die array, are arranged for a shadow mask to cover the lower portion of this array during loading. This arrangement allows one type of metal to be loaded at a time, reversing the shadow mask in between. Another aspect of this design and important to the array arrangement, is reducing the number of off die connections. As will be discussed later, the cryostat used in these experiments has 8 AC connections and 10 DC connections. With the number of MEMS devices contained within the atomic scale 3D printer, these connections have to be optimized. Thus, each set of six source plates will evaporate as a group being connected in series and parallel. The ground for each circuit uses the same one for the entire die. Rather than using a Ni shadow mask for loading, another die design (Figure 2·14) was cre-

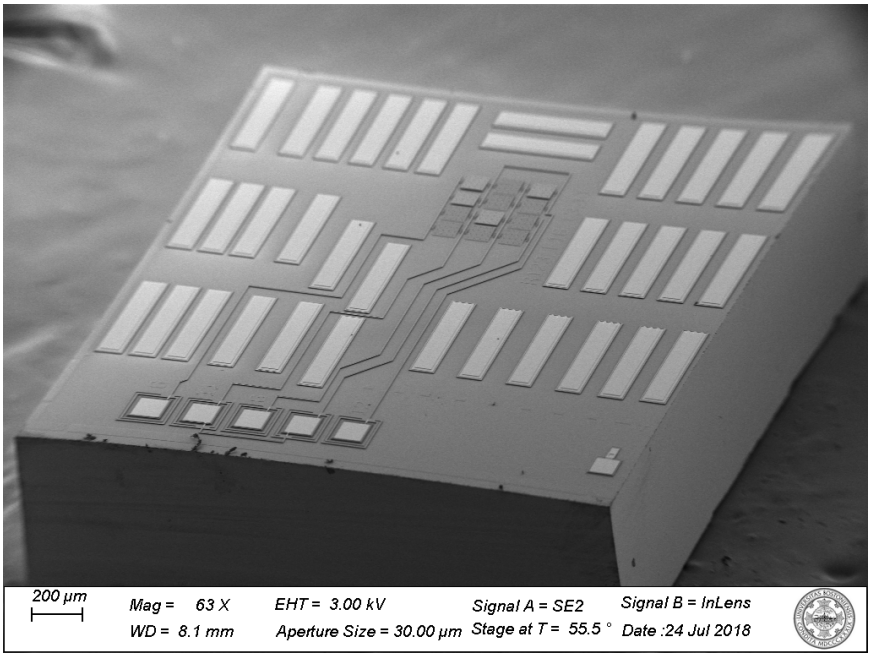

Figure 2·13: SEM image of source die with 3x4 array for evaporating two materials.

ated. Here, two masks, 225 μm x 450 μm, are created with the PolyMUMPs process Poly 2 layer. The masks are separately hinged to the substrate with $\approx$ 100 μm x 225 μm hinges. The standoff column adjacent the array and opposite the hinge, acts as a stop for the mask. Upon release, the two hinges can be operated independently to cover half the array of sources. Once one set of sources have been loaded, opening the opposite mask and closing the other mask allows for the second metal deposition. Opening and shutting the masks requires a probe station.

After depositing with a 3 x 4 array of 50 μm x 50 μm source plates, it was determined that there would be insufficient material deposited at a distance of $\approx$ 600 μm through a small aperture. Therefore, designs were made to increase the amount of evaporated material from the source die. The first step in this quest was to increase the source plate size from 50 μm x 50 μm to 100 μm x 100 μm. By increasing the

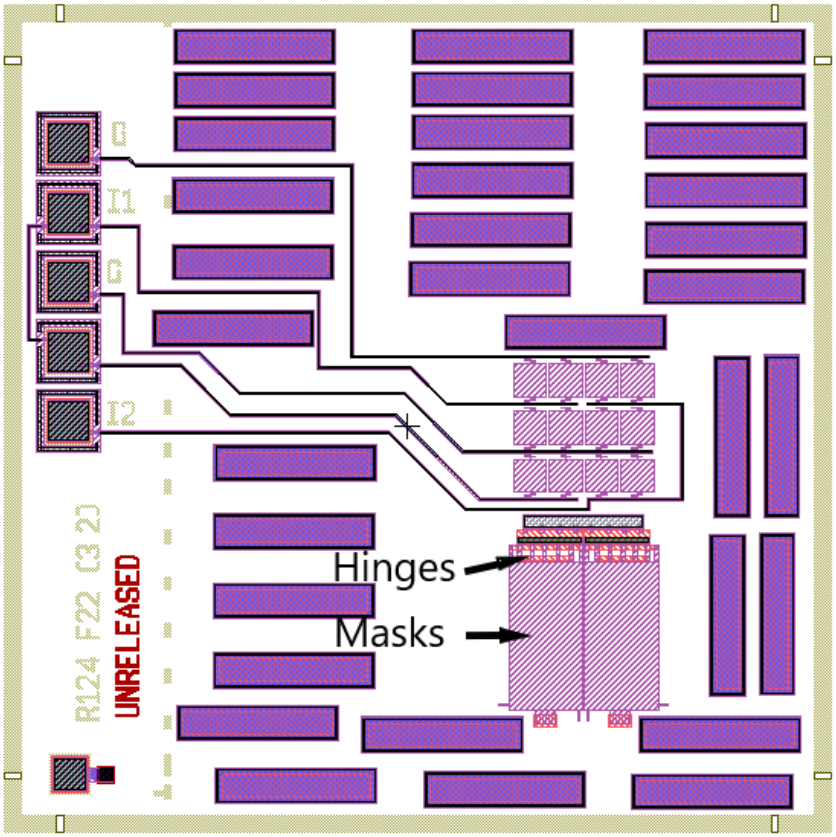

Figure 2·14: L-Edit image of 3x4 array with folding masks for evaporating two different materials

surface area and loading the same amount of material, the deposition should increase by a factor of four. Therefore, the designs were made with the 100 μm x 100 μm source plates and similar characterization as for the smaller version was conducted. Not surprisingly, the results were similar since the design used the same exact springs as heaters but with the larger plate surface. In an effort to further, increase the atomic flux and deposition yield, another design was created increasing the 3 x 4 array of source plates to a 5 x 6 array. As seen in figure 2·15, the arrangement of the array again facilitated the loading and evaporation of two metals and minimized the number of external die connections. As will be described later, this configuration yielded $\approx$ 50 nm through a 7 μm aperture.

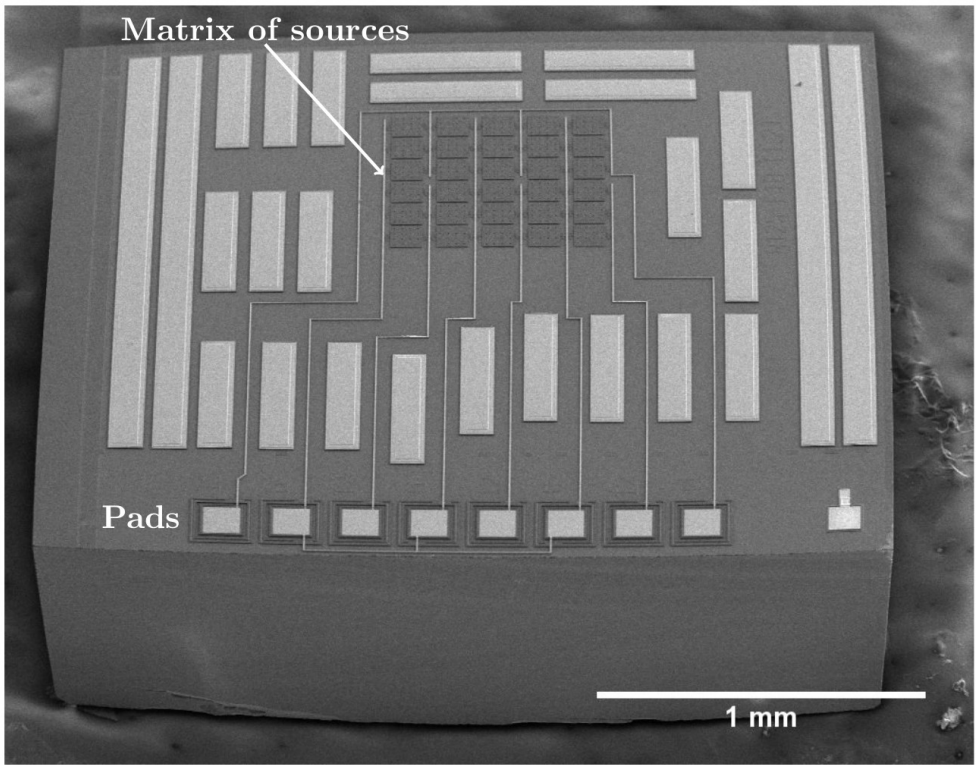

Figure 2·15: SEM image of source die with 5x6 array for evaporating two materials

In the evolving effort to increase the amount of material which could be evaporated form a source plate, another approach was designed. This source plate employs the MEMSCAP foundry but uses a different process. The SOIMUMPs process is a simpler process with just three layers [Cowen et al., 2011]. This process starts with a Silicon on Insulator (SOI) wafer which has a 400 μm handle, 2 μm layer of oxide and a top layer of 25 μm of silicon. Figure 2·16 shows an example of a released MEMS device using the SOIMUMPs process. The process allows one to pattern all three layers. In fig 2·16, the handle is indicated by blue, the insulator by black, and the top layer by red. The substrate is etched from the bottom and the top layer from the top. A gold layer can be added to the doped 25 μm top layer (shown in figure

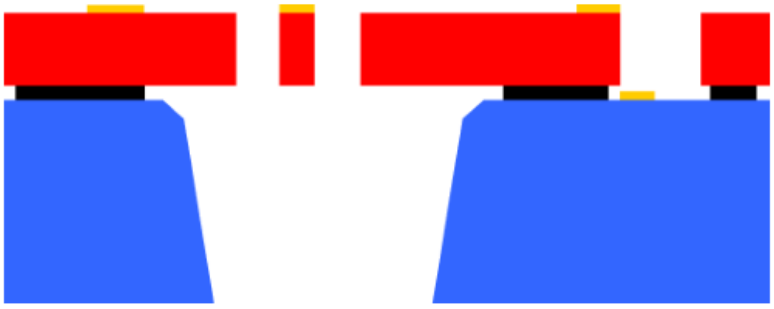

Figure 2·16: Image of SOIMUMPS process [Cowen et al., 2011]

2·16 as yellow). This gold layer provides the ability to connect the MEMS devices externally. Using the SOIMUMPs process a 400 μm x 400 μm x 25 μm plate was connected by similar type springs that again act as heaters. The springs are 6 μm x 25 μm by a total length of about 150 μm (figure 2·17 [Barrett et al., 2020]). A FEA

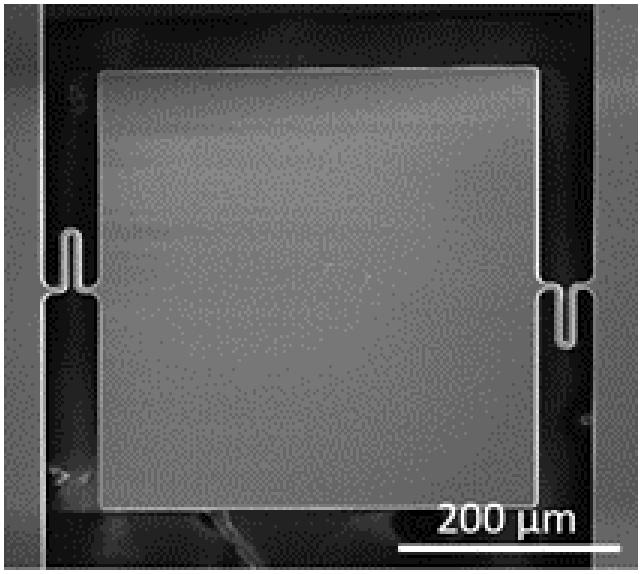

Figure 2·17: Image of 400 μm x 400 μm source made with the SOIMUMPs process. [Barrett et al., 2020]

of this source yielded figure 2·18 [Barrett et al., 2020]. The results are very similar to that of the 50 μm x 50 μm source. One sees that the plate is uniformly heated by the two springs. One major difference due to the size of this source plate is the thermal

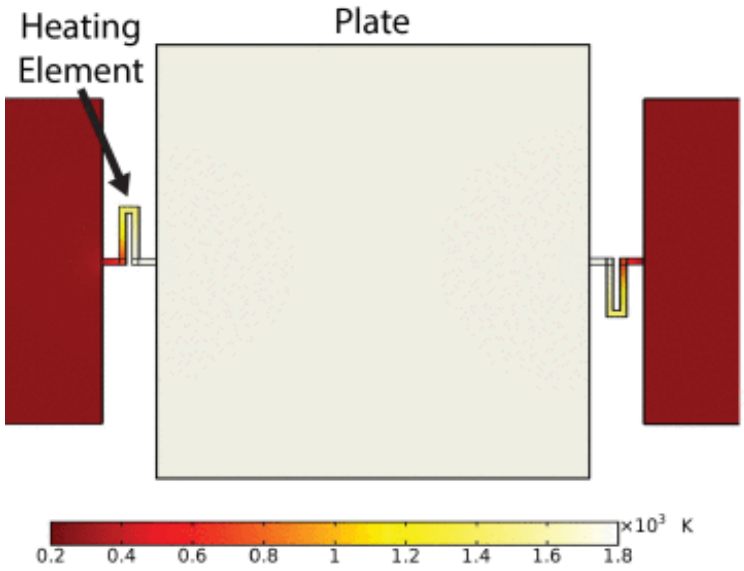

Figure 2·18: FEA of thermal response to voltage applied to 400 μm x 400 μm source [Barrett et al., 2020].

time constant. With equation 2.4 you can determine the thermal time constant,

$$\tau_{\text{th}} = \frac{\rho V C}{h A_s} \tag{2.4}$$

where, ρ is the density, V is the volume, C is the specific heat, h is the convective heat transfer coefficient, and A_s is the surface area. Since the volume and surface area are the determining factors for similar materials, it is not surprising that the thermal response time increases from 5 ms for the unloaded 50 μm x 50 μm x 2 μm source plate to 38 ms for the unloaded 400 μm x 400 μm x 25 μm source plate. When a depositing material is added such as lead the thermal response time increases to 1.46 seconds. PWM for this device is possible but is much less advantageous than the smaller PolyMUMPs source plates. However, with the robustness of the thicker plate and heater springs, this source plate can be loaded with a large amount of material. In fact, instead of using a conventional PVD setup to load the large source plate, one can load it manually with a probe station. By cleaving a Pb pellet,a small amount

($\approx$ 250 μm x 250 μm) can be placed on the surface of the source plate. Figure 2·19 shows the evaporation rates of the source plate with various voltages applied. At the

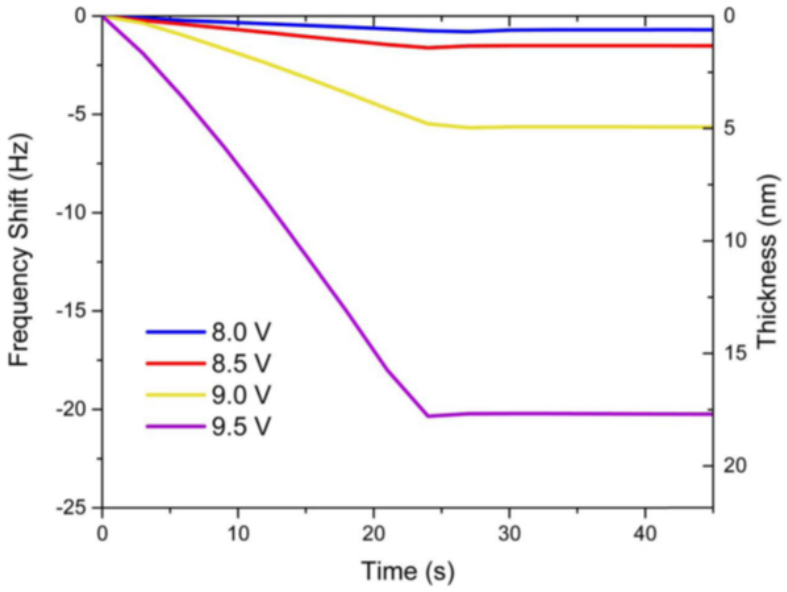

Figure 2·19: Pb deposition rates are shown in this figure using the 400 μm x 400 μm source [Barrett et al., 2020].

peak voltage of 9.5 V, the deposition rate reaches 7.2Å s^{-1}.

This completes the discussion of the source die and its ability to provide sufficient material onto the target die. This section has also shown that small increments of materials can be deposited with PWM lowering the power consumgption and making it ideal for a cryostat environment. The next section will cover the atomic scale 3D printer method of patterning.

Chapter 3

Patterning with the Writer Die

3.1 Writer Die Design and Patterning

Having seen that micro scale sources can evaporate sufficient amounts of metal, an atomic scale 3D printer requires a patterning process. Here, we incorporate a method dubbed "atomic calligraphy" [Imboden et al., 2013] to pattern evaporating metal onto the target. This die is also fabricated with the PolyMUMPs process but undergoes a number of post fabrication processes, which will be discussed in the Assembly Section. The design uses a writing plate attached to and moved by four electrostatic comb actuators to create a pattern on the substrate. The general design consists of a 150 μm x 150 μm writer plate which is suspended by thin (2 μm), long ($\approx$ 500 μm), tethers. These tethers are supported by floating, folded springs, which terminate into one side of the comb drive. The other side of the comb drive is anchored to the substrate and is electrically connected for activation. The SEM image in Figure 3·1 a illustrates the layout of the MEMS writer die with respect to the writer plate and comb drives. Figure 3·1b provides a closer view of the comb drive and figure 3·1c the writer plate. These two features are the key to the atomic calligraphy dynamic writing and are at center of the atomic scale 3D printer, figuratively and literally. First, we will review the electrostatic motor. Figure 3·2 [Imboden et al., 2014b] provides a close look at the MEMS features that create the comb drive.

Figure 3·2a [Imboden et al., 2014b] illustrates how the static combs in red will have

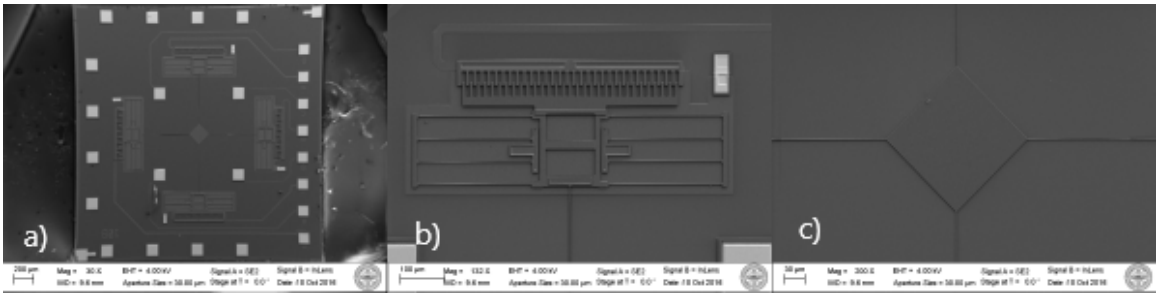

Figure 3·1: SEM images of a) writer die, b) closeup of comb drive, c) closeup of writer plate.

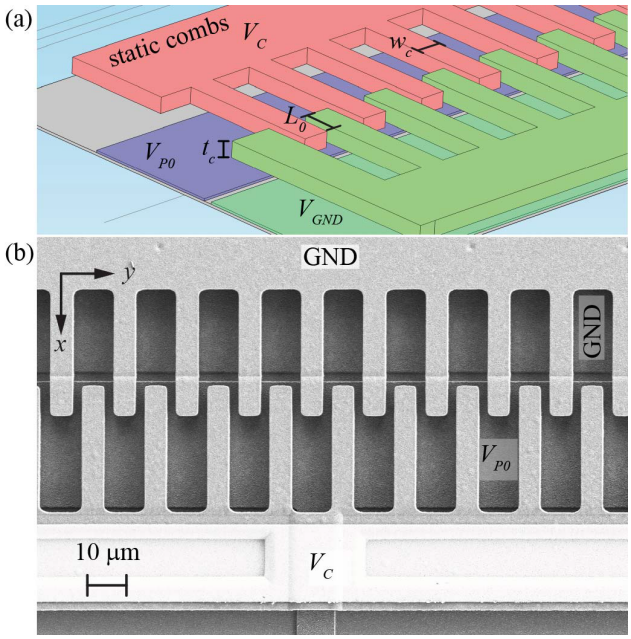

Figure 3·2: Comb Drive images of a) electrostatic comb drive rendering b) close up SEM of comb drive. © [2014] IEEE. Reprinted, with permission, from [Imboden et al., 2014b]

a voltage V_c applied. The other set of comb drives (green) are kept at ground V_{gnd}. Therefore, when the voltage is applied to the static comb, the grounded moveable comb will shift in the direction of the applied electrostatic force. Since the writer plate is tethered to the comb drive, the plate moves with it. On the opposing side of the same axis, the moveable comb will also be pulled by the tethers attached to the plate. The springs act as a restoring force so that the plate returns to the original

location when the applied voltage is removed. The same outcome applies to both x and y axis electrostatic motors. Therefore, by manipulating all four comb drives any 2D pattern can be created by the motion of the writer plate due to the force exerted on it. There are two forces acting in the comb drive assembly which are in equilibrium when the plate is stationary. Equation 3.1 represents the electrostatic force of the capacitor, where V is the applied voltage and $\frac{dC}{dx}$ is the rate of change of the capacitance with displacement of the comb drives.

$$F = -\frac{V^2}{2}\frac{dC}{dx} \tag{3.1}$$

The restoring force of the spring follows Hooke's Law as in Equation 3.2, where k is the spring constant and x is the displacement.

$$F = -kx \tag{3.2}$$

Since the two forces are balanced at any given position, equations 3.1 and 3.2 are combined (equation 3.3) and the displacement x can be solved for as in equation 3.4.

$$F = -kx = -\frac{V^2}{2}C' \tag{3.3}$$

$$x = -\frac{C'}{2k}V^2 \tag{3.4}$$

With the capacitance remaining unchanged over small ranges the $\frac{C'}{2k}$ term can be treated as a constant. Therefore, the displacement is proportional to the squared voltage. Figure 3·3 is a graph of the displacement of the writer plate versus V^2. Applying voltages of up to 100 V can move the writer plate in any direction on the x-y plane $\approx$ 10 μm. Since the writer plate can move 10 μm in both the positive and negative directions of the x-y plane, the writeable area is 20 μm x 20 μm. The

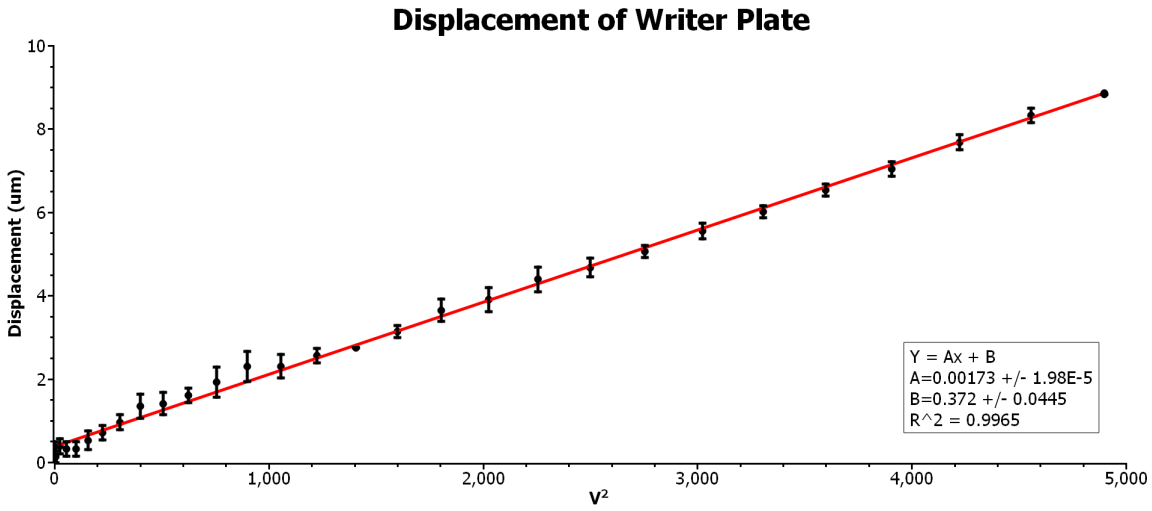

Figure 3·3: Graph of the displacement of the writer plate versus the square of the applied voltage.

precision of this particular comb drive displacement has been calculated to be on the order of a few nanometers [Imboden et al., 2013]. This is again owing to the accuracy that can be achieved with MEMS devices created at this scale.

The second important component of the writer is the plate itself. It is remarkable how robust the writer plate is with 2 μm x 1.5 μm x 500 μm tethers. The 150 μm x 150 μm plate surface provides amble space for atomic scale 3D printing compatibility. Single apertures or arrays of apertures can be milled into the plate with a FIB. Various sized and shaped apertures down to the limit of the FIB ($\approx$10 nm) can be formed with pre-thinning [Imboden et al., 2013]. Below are two structures (Figure 3·4) that have been deposited using these type writer plates and actuators. Neither of these structures can be created using a static mask. Also of interest is the aperture that was used to form the Mobius loop. The orientation of the aperture when depositing forms a "calligraphy like" appearance and has been termed "Atomic Calligraphy". [Imboden et al., 2013]

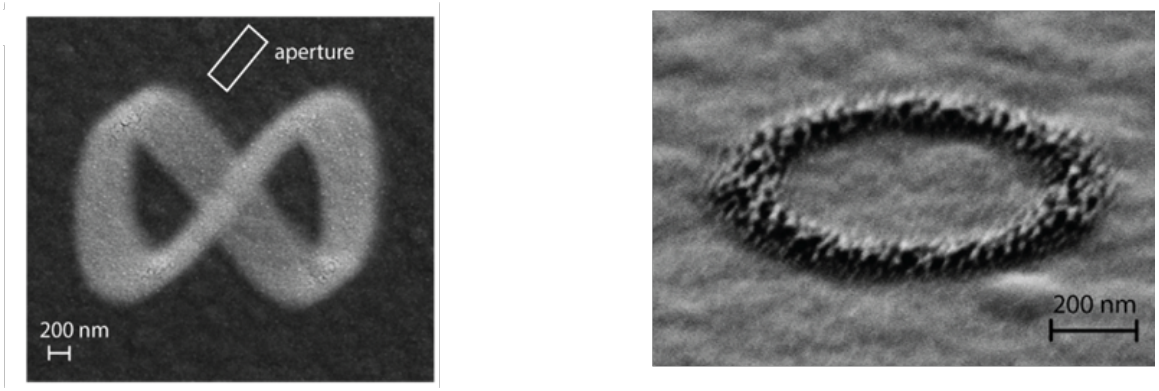

Figure 3·4: SEM Images showing the versitility of Atomic Calligraphy. The LHS illustrates how the writer plate aperture orientation deposits material in a similar way as calligraphy. The RHS shows atomic calligraphy can create small sized unique structures. Reprinted with permission from [Imboden et al., 2013]. Copyright (2013) American Chemical Society.

3.2 Enabling Writer Die Inclusion

For the atomic scale 3D printer to be functional as depicted in figure 1·3, the writer die requires a series of changes from the type used for atomic calligraphy on the attached substrate. As seen in figure 3·1, single tethers suspend the plate and an electrostatic shutter was incorporated. For this purpose, a more robust design is needed and the single tether in each direction is replaced with two tethers (figure 3·5) and rotating the plate 45 degrees. This configuration is more reliable during the back side etch and release process. It is particularly helpful during the assembly process where the die is transferred and bonded multiple times. In the previous section, it was shown that the source die by itself can evaporate small quantities of atoms with PWM. With that capability, a shutter to control the evaporation is not required and is not used in the atomic scale 3D printer.

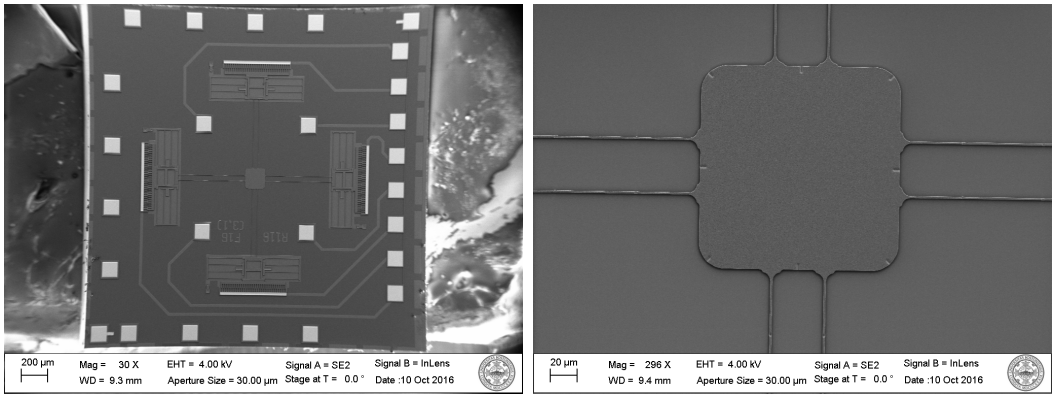

Figure 3·5: SEM Images of writer die (LHS) and the writer plate (RHS)

As shown in figure 1·3, the target die is placed on top of the writer die. This results in two issues. Since the target die is upside down, electrical connections cannot be made through a conventional ball bond. The other concern is that the writer plate may contact the substrate or structures on the target die. Therefore, additional features are incorporated on both die to allow for electrical connections, structural stability, and a minimal standoff distance. The writer die shown in figure 3·5 has a series of gold-capped squares (100 μm x 100 μm) along the perimeter of the die. These squares (seen in figure 3·6) are composed of the three polysilicon layers, encapsulating the two oxide layers. This layering creates features that are 7.35 μm above the insulating nitride layer. None of these structural pads are electrically connected to the rest of the die.

There are also four pads equally spaced around the writer plate. These pads are fabricated using the same method as the structural pads. Besides providing some structural support, these four pads are also each connected to a bonding pad at the edge of the die. Signals from the target die can be transferred through these pads and the signal collected off the writer die via the bonding pads.

Since the only way we can communicate with the target and writer die is through

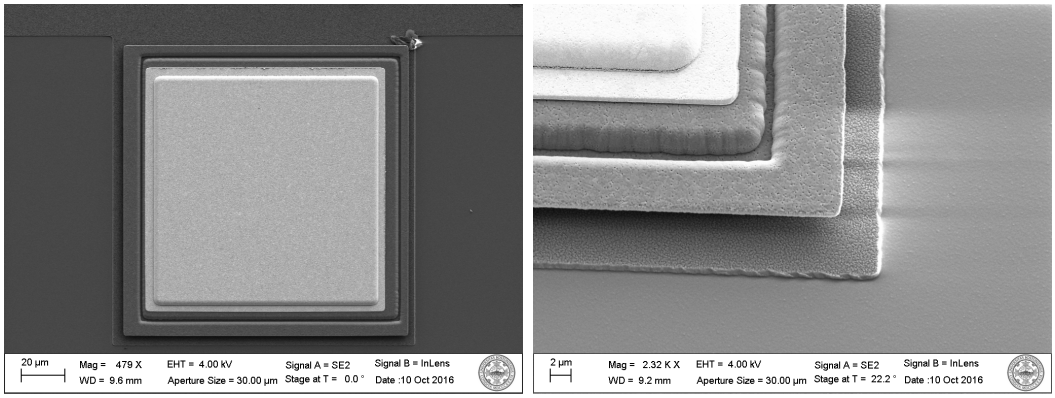

Figure 3·6: SEM Images of structural pad (LHS) and a closeup of the pad's profile (RHS)

the ball bond pads at the edge of the writer die, access to these pads is important. The capillary tube on a ball bonder widens to over 400 μm in diameter from its tip at a height of around 600 μm (the height of the target die). The edge of the target die must be positioned far enough back to allow access to the bonding pads. Repositioning the structural and interconnecting pads is necessary with the goal of keeping the writer plate centered exactly between the source die and the target die. The offset necessary between the edges of the writer die and target die is $\approx$ 450 μm. Since each die is normatively 2,500 μm x 2,500 μm, roughly 20 percent of the target die is hanging off the writer die. The same is true in the case of the source die, which means 40 percent of the target die is not aligned with the source die.

Galvanic attack is a known issue for PolyMUMPs fabricated die [Cowen et al., 2013]. Connections between the Poly 0 layer and the gold layer are prime for galvanic attack. All of the leads on the writer die utilize the poly 0 layer which are attached to the gold bonding pads. The highly n-type doped polysilicon and the gold pads creates the situation of two dissimilar metals being in contact. During the HF release the thin polysilicon is etched and oxidized. Under long releases, >10 minutes, serious damage can be done to the polysilicon leads. Discoloration, reduction in thickness

and significant increases in resistance are observed after galvanic attack of the poly 0 layer. The solution has been to ground the bonding pads to the handle of the die with a poly 2 layer tether as seen in the bottom right of figure 3·7. The Poly 0 lead can be seen connecting to the gold layer on the upper left side of the figure. After the die is released the tether will be floating above the nitride layer and can easily be broken with a probe tip or the gold ball of the ball bonder. This approach has been incorporated into all the newer writer designs.

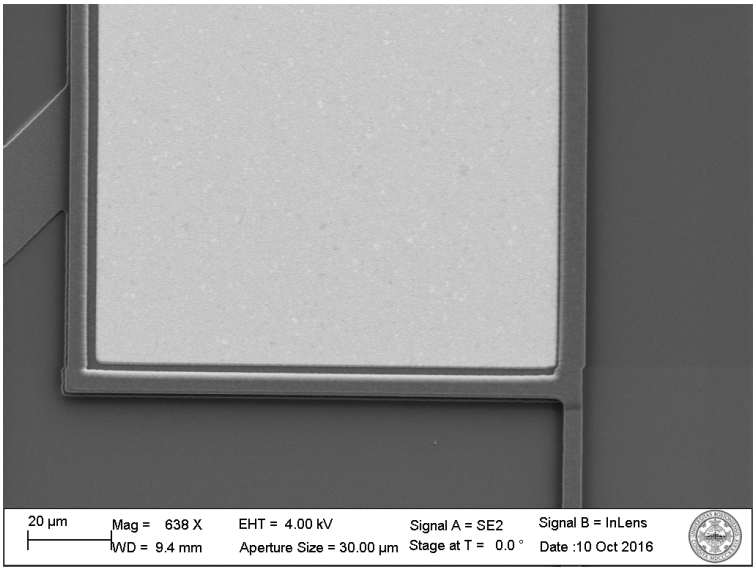

Figure 3·7: SEM Images of writer die bonding pad with Poly 2 tether.

For the atomic scale 3D printer to be fully operational, a mass sensor and temperature sensor need to be incorporated. Their inclusion requires six additional bonding pads. Under the constraints of the PolyMUMPs process, the minimum space between bonding pads does not allow more than 12 pads excluding the handle ground pad. The writer in figure 3·5 has eight bonding pads, four for the target die and four for the writer's comb drives. In figure 3·8 two of the comb drive leads have been sacrificed to accommodate the addition of the mass sensor and the temperature sensor.

Correspondingly, conductive interconnects have been positioned on the writer die to interface with the target die. This design is still capable of creating unique circuits and combinatorial materials. The results of this design are shown in Chapter 6.

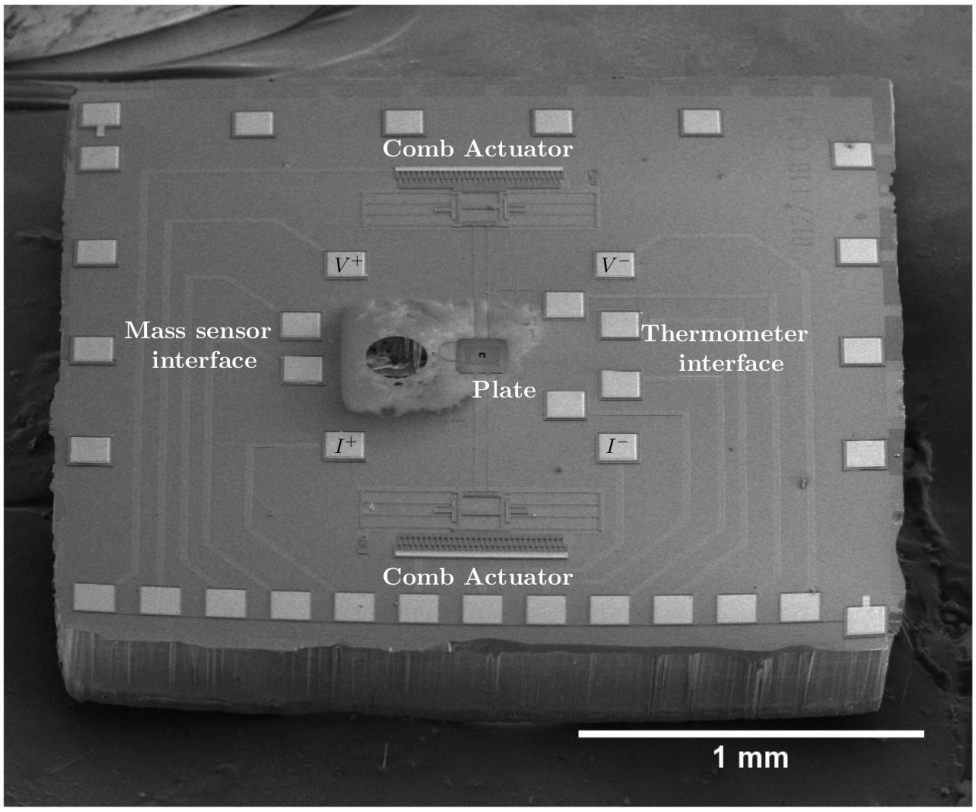

Figure 3·8: SEM Image of enhanced writer die with connections for the mass and temperature sensors.

Chapter 4

Sensing with the Target Die

In the last chapter, the primary focus was on the comb drives that positioned the writer plate. The comb drives are MEMS actuators, which provide the nanoscale movement of the writer plate, based on their size and geometry. The source plates in chapter two are also MEMS actuators. In this chapter, however, we will discuss three sensors, which provide the ability to characterize the evaporating material. Again, due to the sensors size and geometry, precise measurements can be recorded.

4.1 Thin Film Resistance Measurement

The target die uses the van der Pauw method as seen in figure 4·1a [Chwang et al., 1974] for resistance measurements. This method allows the resistance measurement of any two dimensional arbitrary shape by placing four probes on the perimeter of the sample. This arrangement allows the average resistance to be measured as opposed to a linear four point probe which measures resistance in the sensing direction (see figure 4·1b). Using Ohm's law, which can be seen in equation 4.1, the resistance can be determined by measuring the current along one edge 12 and the voltage along the opposite edge 34. With the van der Pauw formula two resistance measurements are made, one along the horizontal edge $R_1 2, 34$ and the other along the vertical edge $R_2 3, 41$. The sheet resistance can then be found with the van der Pauw formula shown in equation 4.2.

$$R_{12,34} = \frac{V_{34}}{I_{12}} \tag{4.1}$$

$$e^{\frac{-\pi R_{12,34}}{R_s}} + e^{\frac{-\pi R_{23,41}}{R_s}} = 1 \tag{4.2}$$

From the van der Pauw measurements one can derive the sample's properties such as resistivity, doping type, majority carrier and mobility. Given a van der Pauw configuration and an appropriately milled aperture, a linear four point probe method can also be used to measure the resistance of the sample as seem in figure 4·1c.

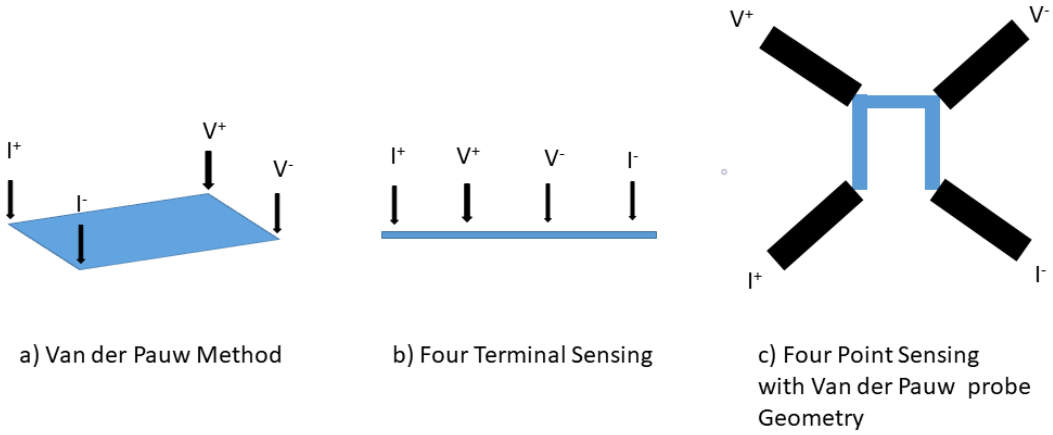

Figure 4·1: Schematic of various probe setups: a) van der Pauw setup b) linear sensing setup c) linear setup with Van der Pauw geometry

A typical target die shown in figure 4·2 is also fabricated using the PolyMUMPs process. The main features are the probes, which form the van der Pauw geometry for resistance measurements [Hemenger, 1973].

These probes consists of four long ($\approx$ 500 μm), thin ($\approx$ 2 μm) low profile gold electrical leads. The leads as shown in Figure 4·2a, converge diagonally from bonding pads ($\approx$ 100 μm x 100 μm) to within $\approx$ 4.5 μm. The four contact pads at the corners of the cross make electrical contact to four similar pads on the writer die as discussed in chapter 3. From there the signal is led off chip by wire bonds. The remaining gold pads on the die are used for structural support in the die stack assembly. These

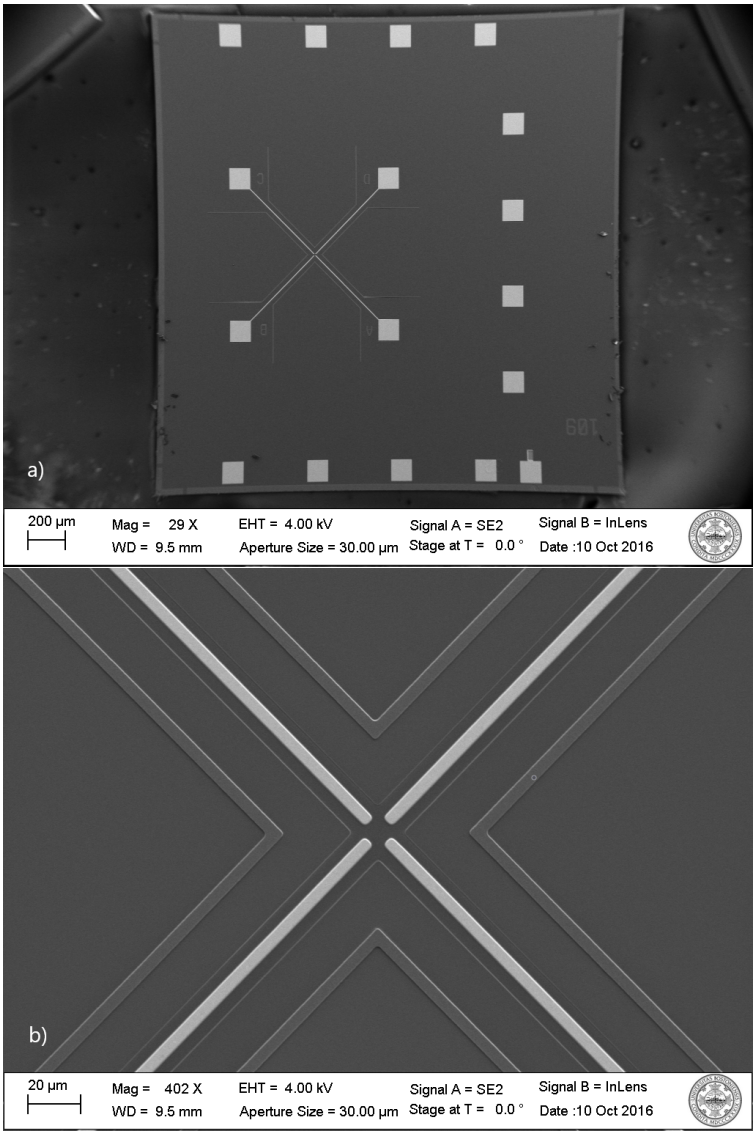

Figure 4·2: Target Die images of a) Overhead of standard target die b) close up of target leads.

structural gold pads are patterned right on the nitride layer. However, before the gold pads are deposited, the nitride layer is thinned and smoothed using the dimple and poly1-poly2 via layers of the PolyMUMPs process. Both of these steps slightly etch into the nitride layer and reduce the protrusion of the gold pad from the typical height of 500 nm above the native nitride layer to $\approx$ 235 nm as seen in figure 4·3. This step reduces the standoff distance between the writer plate and the four probes.

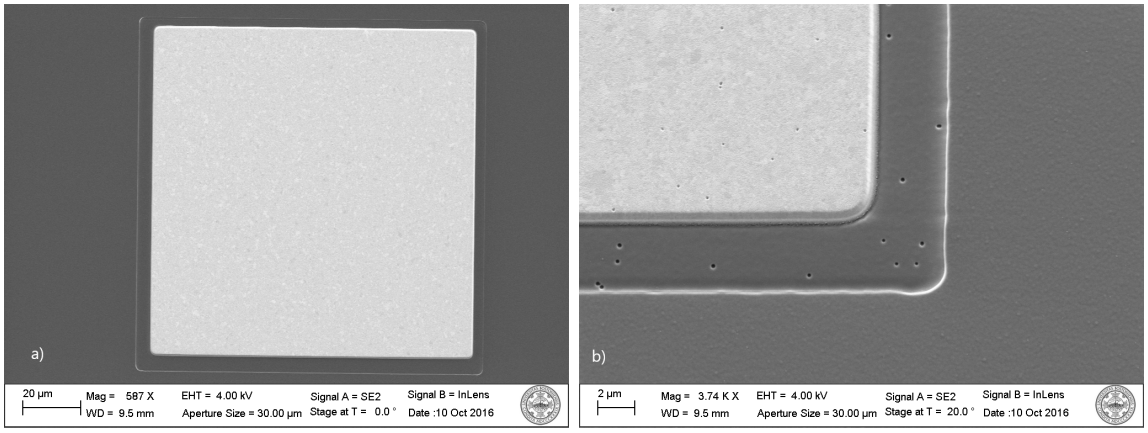

Figure 4·3: Target Die images of a) Connecting pad b) Close up of connecting pad.

The films that can be produced with the atomic scale 3D printer can be quite thin ($\approx$ 2 - 10 nm) [Imboden et al., 2017], so special care must be taken to provide an insulating, very smooth surface for the patterned deposition [201, 2010]. The leads are also fabricated by using the native PolyMUMPs gold placed on the nitride layer that has been thinned by outlining each lead with a 5 μm wide dimple layer plus a Poly1/Poly2 Via contour. The result of this process creates roughly a 10 μm x 10 μm space at the intersection of the leads, where films can be deposited either statically or dynamically (since this is well within the motion limits of the writer plate). The other important result of this nitride thinning process is that the gold layer forms an ohmic connection site for the thin film. This process produces a gold film whose edges bleed out onto the substrate making it easier for electrical contact to be made with atomically thin films on a smoother surface. The result of this process is shown in figure 4·4. Using this approach to create the leads allows thin film measurements down to $\approx$ 2 nm [Imboden et al., 2017].

In figure 4·2a, the leads are not centered on the die. This offset accounts for the

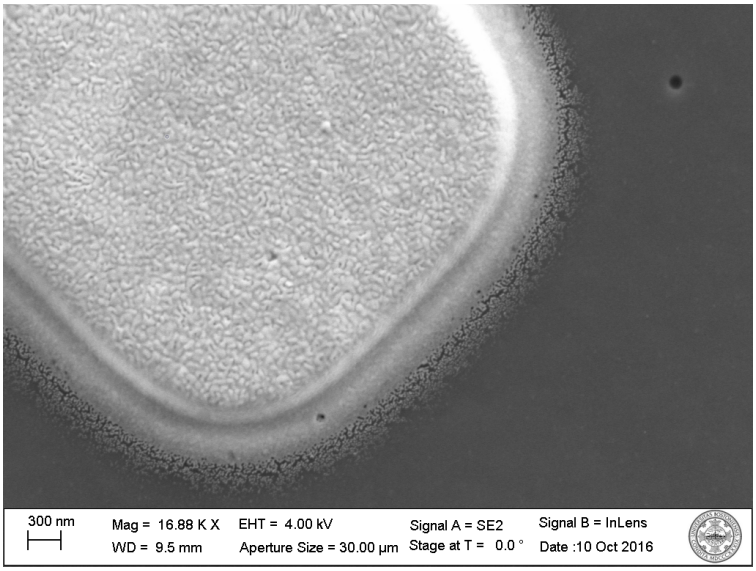

Figure 4·4: Image of target lead tip showing the tapering of the gold layer.

20 percent overhang that allows access to the ball bonding pads on the edge of the writer die. The position of the leads and structural pads on the target die are fabricated to align with the attached writer plate and corresponding structural pads. When the writer die and the target die are stacked together, without any applied force to the comb drives or any bonding material between the bonding pads, the distance between the writer plate and electrical leads is ≈ 3.6 μm. Due to the levitation of the comb drives during activation, this distance decreases. However, at this standoff distance, shadowing effects of deposited materials are minimal.

4.2 Film Thickness Monitor

The next MEMS sensor located on the target die is a film thickness monitor. As with any PVD or fabrication process, monitoring the evaporation rate and the thickness of the depositing material is essential. In this case, the film thickness monitor is a MEMS trampoline design shown in Figure 4·5 [Imboden et al., 2014a] [Park et al., 2012]. Four 4 μm wide by 130 μm long Poly 1 layer springs are attached to the

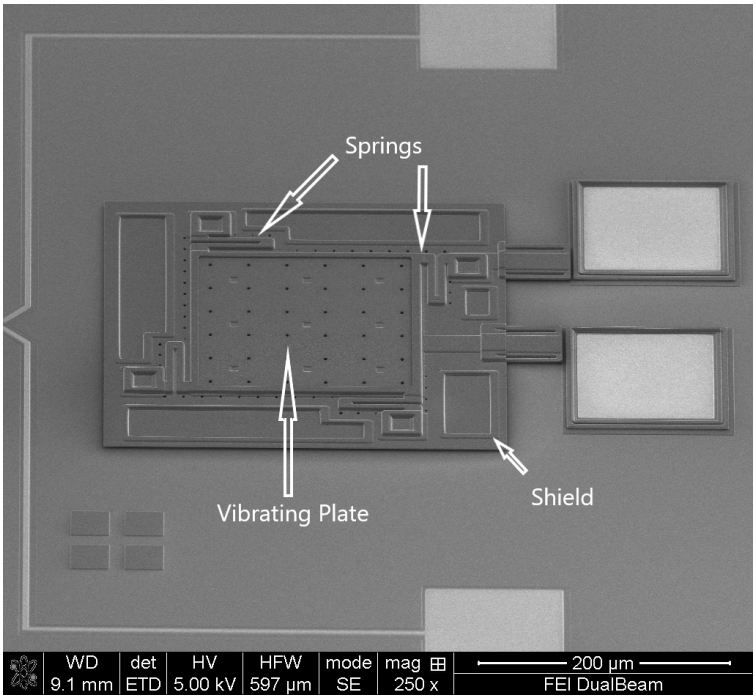

Figure 4·5: Image of mass sensor seen at an angle.

four corners of the moveable plate. The other end of the springs are anchored to the substrate. The plate, suspended by the springs, is 190 μm x 190 μm Poly 1 layer. Above the Poly 1 plate layer is a Poly 2 layer that exposes 170 μm x 170 μm of the Poly 1 plate, but covers the springs. Below the suspended Poly 1 plate is a static plate fabricated from the Poly 0 layer. Bonding pads and Poly 0 leads are attached to the static plate and the spring enabled plate. These bonding pads allow the top plate to be driven to the resonant frequency while the bottom plate measures the capacitance between the two plates. With the addition of a frequency counter, the resonant frequency can be monitored. The device is designed so that the springs, seen in the print through of the structure surrounding the plate, are shielded from the atoms landing on the surface. The depositing atoms then change the mass of the plate and not the spring constant of the structure. Thus, as atoms land on the structure, its resonant frequency is reduced by an amount proportional to the

added mass. By approximating the mass-spring model, the resonance frequency can be shown as equation 4.3.

$$f_o = \frac{1}{2\pi}\sqrt{\frac{k}{m_{eff}}} \tag{4.3}$$

The mass sensitivity can then be expressed as equation 4.4

$$\frac{\Delta f_o}{f_o} = -\frac{1}{2}\frac{\Delta M_{\text{eff}}}{M_{\text{eff}}} \tag{4.4}$$

Here f_o is the resonant frequency of our mass sensor, M_{eff} is the effective mass of the moveable plate and springs, and k is the spring constant. Since as mentioned the springs are covered, the spring constant should remain unchanged. With equation 4.4 one can readily determine the amount of mass deposited. Conducting a frequency sweep with the mass sensor one can establish the resonant frequency for that device. Once the resonant frequency is found, a self-oscillating Phase Locked loop (PLL) can be generated. Under this condition, the resonant frequency will decrease as mass from the deposition coats the mass sensors vibrating plate. At this point equation 4.4 can be used to determine the amount of mass deposited based on the frequency change determined from the PLL signal.

This device has a resonant frequency of $\approx$ 80kHz, as seen in figure 4·6. The device can have a Q of $\approx$ 50,000 when measured in an open loop frequency sweep under ultra high vacuum. Using a lock-in amplifier and a closed loop setup, the allan devisation provides the frequency stability and as a result the mass sensor sensitivity. With 10 seconds of averaging as little as $\approx$ 2.5 fg can be measured, which is roughly 5 million atoms or 10^{-5} monolayers (of Au), resulting in about 175 atoms/μm^2 [Imboden et al., 2014a]. Besides being a very sensitive film thickness monitor, the mass sensor is also very sensitive to temperature changes. This particular mass sensor can resolve temperatures in the mK range. The response of the mass sensor to tempera-

ture change can be calibrated and removed from the mass sensor measurement. This effect will be demonstrated in a later chapter.

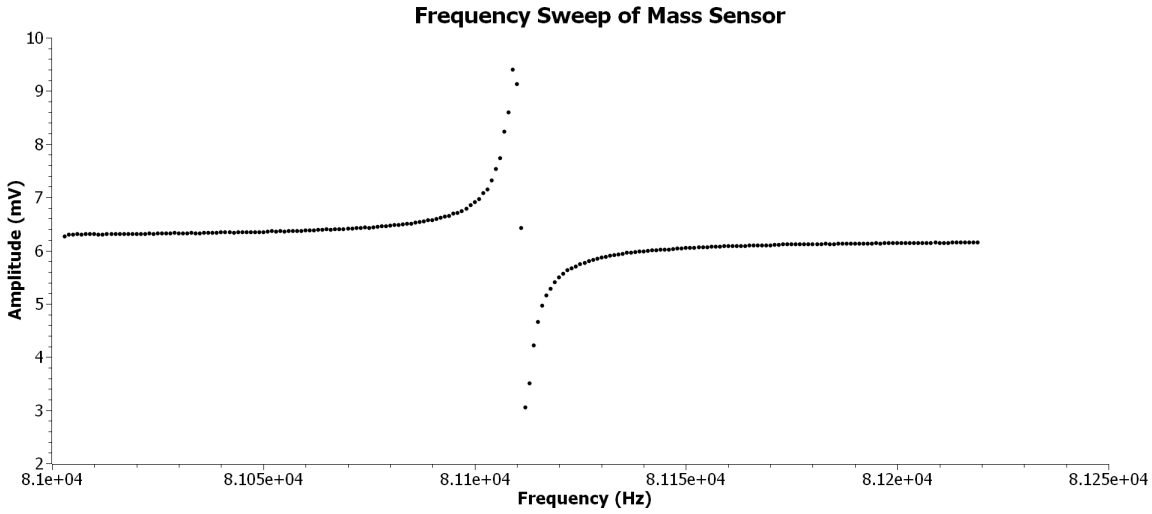

Figure 4·6: Graph of frequency sweep of mass sensor showing resonant frequency.

The film thickness monitor should be placed as close the targeted area as possible. However, due to the height of the mass sensor and that of the writer plate, they cannot overlap. As shown in figure 4·7, the placement of the mass sensor has been carefully oriented so as not to interfere with the resistance measuring probes or the writer plate. When assembled there is a 10 μm separation between the edge of the writer plate and that of the mass sensor. Based on the 5 x 6 array of sources, which covers 640 x μm 680 μm, the shift of the mass sensor by approximately 175 μm off center will have minimal effect and a tooling factor can be employed as in full sized PVD evaporator systems to recalibrate the measurements.

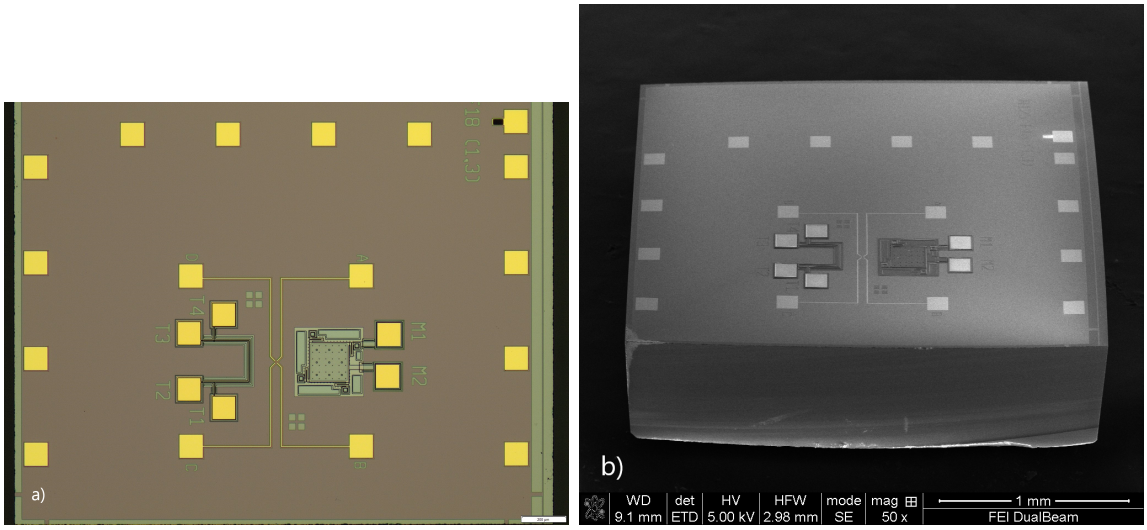

Figure 4·7: Target Die with sensor: a) optical image of target die with sensors b) SEM image of target die with sensors.

4.3 Temperature Sensing

The last of the MEMS sensors on the target die is for monitoring temperature. During an evaporation at cryogenic temperatures, it is essential to monitor the temperature of the substrate. Thin films are very sensitive to temperature changes and any annealing due to the evaporation process or post deposition could damage the sample. A temperature sensor may also be necessary if you want to evaluate a circuit fabricated with the atomic scale 3D printer. The temperature sensor incorporated on the target die is shown in Figure 4·8. It consists of a 10 μm wide polysilicon layer (Poly 1) directly deposited onto the nitride layer of the POLYMUMPS process. The Poly 1 layer lead is the actual sensing element. The Poly 1 layer is protected by a polysilicon layer (Poly 2) from any errantly deposited material. The Poly 1 layer is also connected to four bonding pads which align with similar pads on the writer die. The four pads allow a 4 point method of resistance measurement to be conducted. Using a conventional resistance bridge, we can resolve mK range of temperature changes [Imboden et al., 2014a].

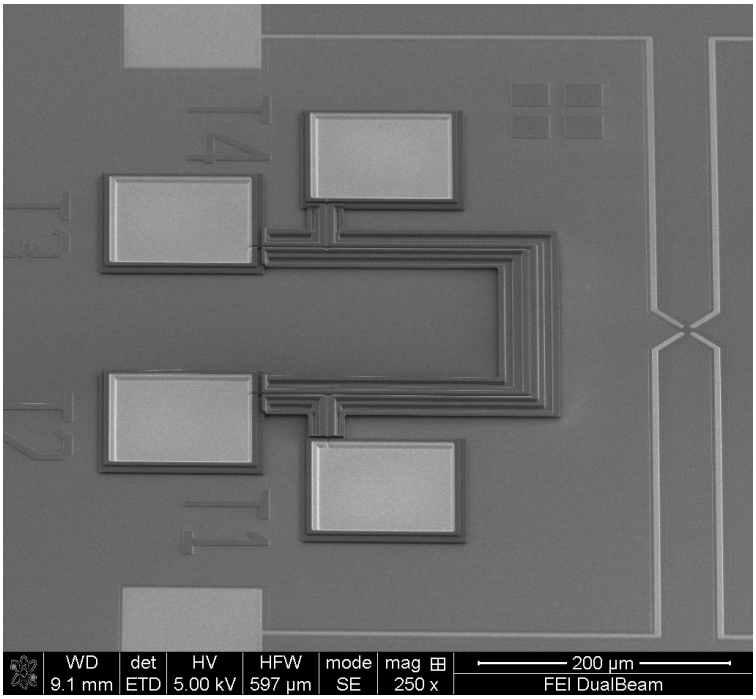

Figure 4·8: Image of temperature sensor

The resistance of a metal typically follows equation 4.5, where R_T is the resistance at temperature T, R_o is the initial resistance at temperature T_o, T_o is the initial temperature, and α is the temperature coefficient of resistivity of the metal.

$$R_T = R_o[1 + \alpha(T - T_o)] \tag{4.5}$$

This yields a linear function between the temperature and the resistance. The polysilicon layer is a highly n-type doped polysilicon layer that reduces the freeze out effect at cryogenic temperatures. Figure 4·9 shows the resistance of this structure as a function of temperature. As captured in figure 4·9 the resistance remains linear as a function of temperature from room temperature down to about 25 K. The resistance trace around 25 K appears to flattens out the slope until approximately 6 K. Below 6 K the resistance falls off significantly. However, each section of this curve can be

calibrated to provide a reliable temperature for the given resistance.

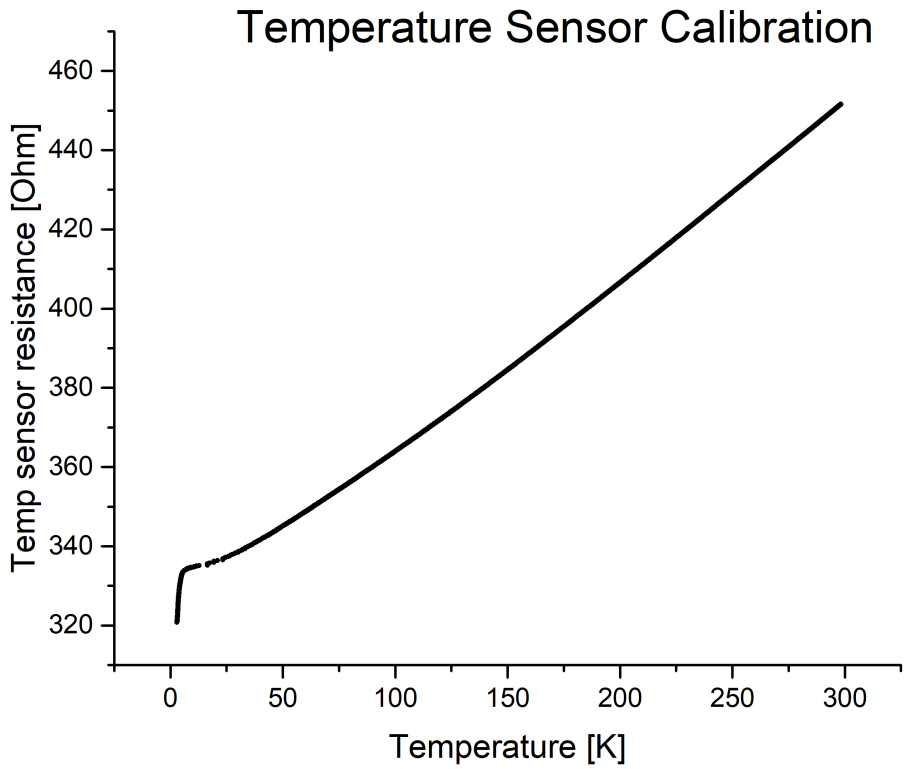

Figure 4·9: Graph of temperature sensor measurements from room temperature to ≈ 3 K

Positioning the temperature sensor as close to the area to be patterned is again desirable. The Poly 1 layer of the sensor is in good thermal contact with the nitride layer. This sensing layer is routed from the connecting pads to within 50 μm of the edge of the writer plate. The same constraints apply here as with the mass sensor on placement. The temperature sensor can also be used as a heater by increasing the voltage. This location is also ideal for its use as a heater. The next chapter will discuss the post processing, preparation, alignment, bonding, assembly, and setup of the three die, resulting in the atomic scale 3D printer.

Chapter 5

Assembling the Atomic Scale 3D Printer

5.1 Post Fabrication Processing

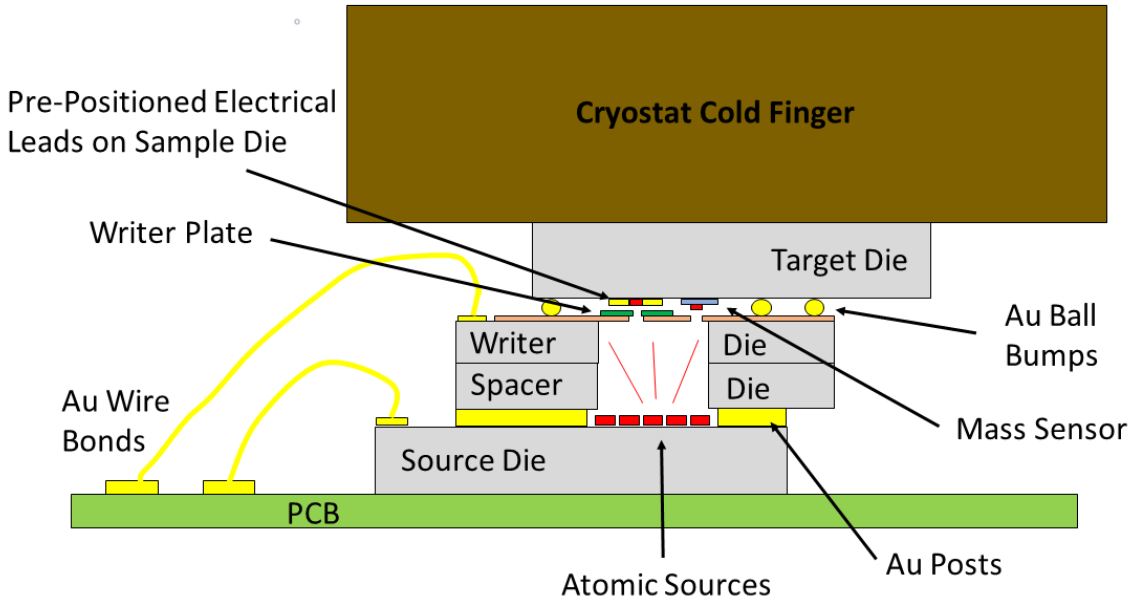

Figure 5·1: Schematic of atomic scale 3D printer

Upon review of the concept figure 1·3 and figure 5·1, there needs to be a pathway created for the evaporated material of the source die to pass through the writer die and deposit on the target die. Therefore, before the atomic scale 3D printer can be assembled, the writer die must be further processed. To allow this evaporation from the source die to the target, a backside etch (BSE) (Figure 5·2) process must be performed on the writer die. The BSE applies the Bosch DRIE process, which

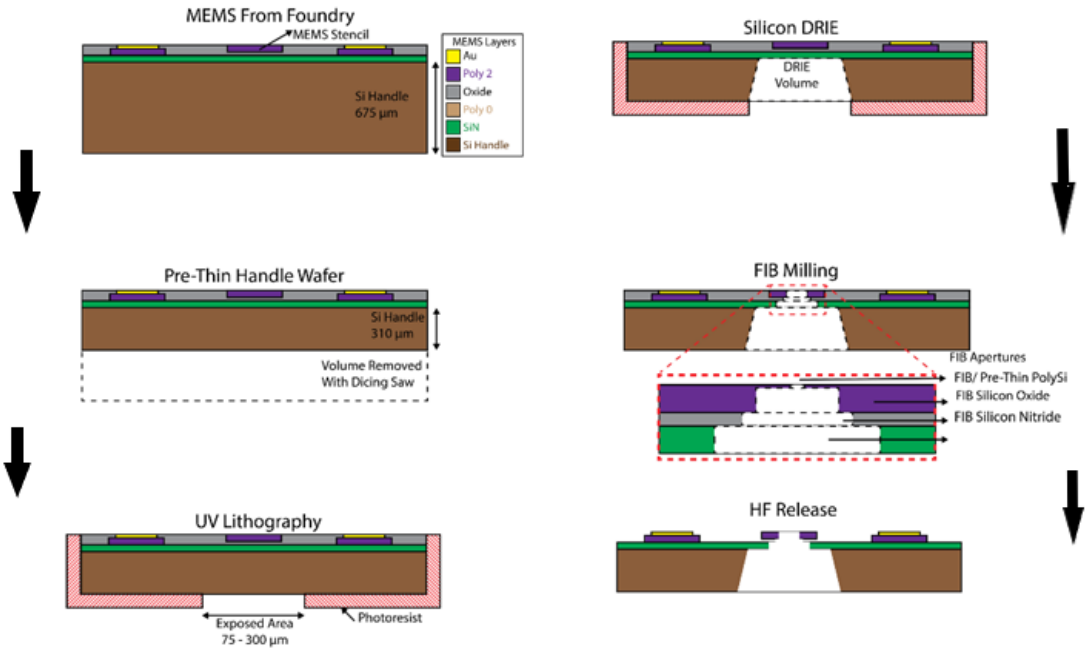

Figure 5·2: Diagram showing the steps in the BSE process.

has a high aspect ratio of about 30:1. Etching through entire wafers is possible with this process but can be problematic depending on the stopping layer. Pre-thinning the die can help alleviate this issue. The writer die is $\approx$ 675 μm thick. Using the dicing saw one can shave the backside (non-MEMS side) from the 675 μm to $\approx$ 310 μm using a two-step process. First, fine shallow cuts are made across the diagonal of the die to prevent chipping and damage to the die. This is followed by the coarse cut which brings the thickness of the die to $\approx$ 310 μm. Once the die has been thinned, the backside is patterned for the DRIE process.

The die is mounted upside down on a glass slide and the MEMS devices are still protected with the photoresist from the PolyMUMPs process. Similar to the PolyMUMPs process steps, a thick layer of photoresist, which covers the groves left by the dicing saw, is spun on the backside of the die. Since the die is placed on the mask

aligner with the backside up, the mask is aligned using the features on the bottom side of the die with the underside cameras. A pre-designed mask with $\approx$ 150 μm x 150 μm pattern in the center is aligned with the plate. The exposed area is dependent on the size of the source array. BSE openings $\approx$ 500 μm x 500 μm and larger have been created with this process. The mask also patterns the streets, which will allow each die to be separated from the others in the group. After exposing the pattern with UV light, the die is developed and baked.

The next step is to perform the DRIE etching which will not etch through the thick photoresist. The exposed area is therefore subjected to the DRIE plasma which etches through the silicon substrate until contact is made with the silicon nitride layer. Here the etch rate decreases since the silicon nitride forms a natural barrier from penetrating the MEMS device layers. This DRIE process is completed in 430 cycles after about 1.5 hours. Even when using the nitride layer as an etching stop, care should be taken so that under or over etching does not occur. Under etching will leave stringers as in figure 5·3. Additional DRIE cycles can remove these features. Etching can also attack the sides of the die so photoresist should be added prior to commencing the DRIE process. Over etching also occurs when insufficient rest time is placed between the cycle groups and the number of cycles is too high. Additionally, damage to the nitride layer and MEMS features can happen if the die is not properly mounted to the carrier wafer before loading into the DRIE. Any space between the die set and the wafer will cause unexpected etching to occur to the die sides and MEMS devices on the front side.

Upon completion of the DRIE process the photoresist can be stripped and the die set carefully separated. The PolyMUMPs process sends 15 die sets, each having a 4 x 4

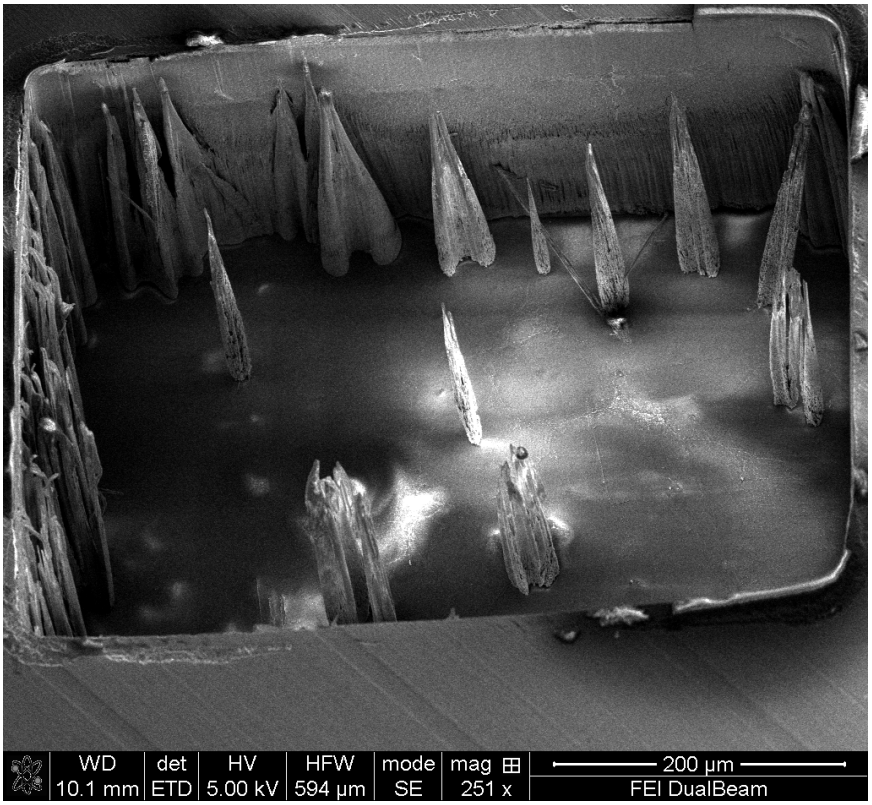

Figure 5·3: Image shows silicon stringers left after incomplete DRIE process.

array of unique MEMS patterns. At this point, the 600 nm thick nitride layer should be the only thing holding the group of 16 die together. Rough handling can cause the nitride layer to crack on adjacent die and render them unusable.

Now that the 365 μm tunnel has been created, a FIB is used to complete the access to the writer plate. The nitride layer is the only structural layer that needs to be breached to expose the writer plate. The writer die is inverted on a specially modified FIB pedestal so that it can be milled through the backside opening. A 90 μm ring, circumscribed with a 95 μm ring, are milled in parallel. This reduces the milling time to a reasonable amount and improves the quality of the cut. During the HF release process the nitride layer circles will be removed. Since the FIB milling is done

prior to the release of the device, the silicon oxide layer protects the writer plate from damage. A second access point is milled into the nitride layer for the mass sensor. Concentric circles of 200 μm and 195 μm are again used to reduce the milling time and improve quality. This 200 μm diameter circle's center is located 250 μm from the center of the previously milled circle. Surprisingly, the nitride layer for this 500 μm by 750 μm BSE opening remains intact over such a large expanse after multiple millings.

The FIB can also mill through the oxide layer and the back side of the polysilicon writer plate can be thinned. With a thinned writer plate, apertures can be milled to a minimum size of about 10 nm. [Imboden et al., 2013] The aperture can be milled from either the top or the bottom of the die. Milling from the top provides for a more accurate positioning of the aperture. When milling through the BSE, the SEM cannot view the milling location due to the high aspect ratio of the DRIEy and large angle, so only FIB imaging is possible. It may also be preferable to FIB after the writer die is released. Survival of a functioning writer die after release is about 50 percent. The DRIE process, FIB milling, and handling during the release process all factor into this success rate. Additionally, over milling with the FIB through the oxide layer causes residue between the nitride layer and the writer plate which is difficult to remove.

5.2 Die Preparation

Once the apertures are milled all three die can be released. Each die is immersed in a Hydrofluoric Acid (HF) bath for varying amounts of time depending on the amount of the oxide layers that are covered by polysilicon. Release times which are too short or too long will effect the operation and the precision of the MEMS device.The HF

dissolves the oxide layer and the Poly 1 and 2 layers are released. With the limited space between the polysilicon layer and the substrate as well as the smoothness of the surfaces, adhesive forces dominate and stiction can be a problem. [Tas et al., 1996] Stiction is a particular concern for the writer die due to the long tethers attached to the plate. Therefore, after the release is complete each die is dried in a Critical Point Dryer (CPD). The die is removed from the deionized water and placed directly into the methanol solution within the CPD. Usage of the CPD reduces but does not eliminate the stiction issue with the writer plate. Consequently, a probe station is used to free the plate from the substrate.

The source die requires preparation also. First, a 20 nm layer of AL_2O_3 is deposited using an ALD process. On top of the insulating layer is deposited $\approx$ 500 nm of the metal to be evaporated. Typically, the metal deposition is performed with a thermal or e-beam evaporator. With certain metals, the bulk metal loaded source die should be used within 72 hours to prevent oxidation of the metal, which could affect the deposition and quality of the deposited metal. In the first approach, the source die was loaded by evaporating metal over the entire die. With certain metals like lead, the ball bonding became impossible through the lead layer. This was resolved by using a Ni mask, which covered the ball bonding pads (See Appendix A for details on mask and holder). Around the same time, it was determined that more metal needed to be evaporated. However, depositing greater than ≈ 1.75 μm caused shorting between the source die plates and the substrate. Therefore, another Ni mask was designed and fabricated. This mask served two purposes, it covered the springs and it kept the metal from shorting out with the substrate. Figure 5·4 shows a loaded source with Pb after using the Ni mask. Positioning the Ni mask requires the use of a probe station and can be moderately difficult.

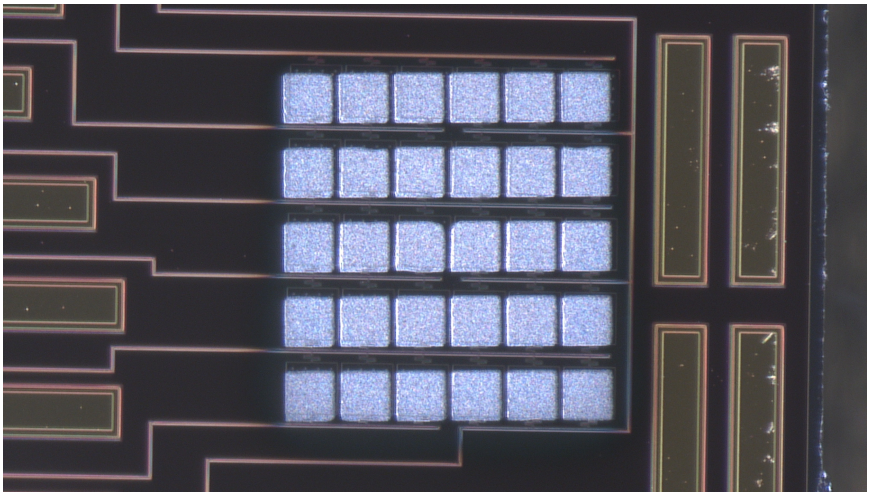

Figure 5·4: Image shows 5 x 6 array of source plates loaded with Pb after using Ni mask.

The only preparation of the target die is to check the mass sensor to ensure it is functional. The mass sensor's moveable plate is also subject to stiction, but unlike the writer die, there is little one can do after the CPD process. The moveable plate can adhere to the Poly 1 layer below it, typically in one corner or massively in the middle. A 3D optical profiler can be used to determine the health of the mass sensor. Ideally, the plate will be concave and proportionally rising in all directions from the middle.

5.3 Bonding Preparation

This section discusses the die preparation for Flip Chip (FC) bonder alignment and bonding. While all three die must be structurally bonded together to form the atomic scale 3D printer, only the writer die and the target die must be electrically bonded and accurately aligned. When choosing bonding materials, one must weigh competing factors such as cure time, glass temperature, viscosity, pot life, and shear strength. A number of potential bonding materials were reviewed. The FC bonder used in

assembly is located offsite in Harvard's Center for Nanoscale Systems. Therefore, a relatively long pot life is necessary. Since the materials also have to withstand ball bonding, the shear strength is equally important. Lastly, a high viscosity was needed to allow transfer of the material to the bonding pad without any tackiness. The EpoTek H20S Ag epoxy was selected and tested and used extensively. It met all the properties necessary for bonding these two die. Gold ball bumps offer another possibility with a thermo-compression bond. Gold ball bumps are routinely used in industry and research programs [Zhang et al., 2004] [Ferrando et al., 2000]. However, most applications required high temperature, large force, and ultrasonic bonding. In addition, a significant amount of surface preparation is necessary above plasma asher cleaning. According to [Ang et al., 2006] weakly formed Au-Au bonds can begin with 100 C - 300 C and 200 -600 g/bump. Figure 5·5 indicates that at low temperature thermo-compression bonds can be formed. Ultimately, the gold ball bumps were tested and found acceptable except for the increase in separation between the writer plate and the target die causing an increase in blurring around the periphery of the deposited sample.

Another consideration was the ability to adhere the bonding material to the bonding pad. Initially, a transfer station was employed using glass pipettes for the Ag epoxy. However, the epoxy's viscosity limited this approach . Instead, a probe station is used to transfer the Ag epoxy. Dipping the probe tip into the prepared epoxy a few times causes sufficient wetting of the tip. Placing the tip onto the gold bond pad the epoxy wets and transfers to the bonding pad. There are 22 of these bonding pads, all requiring the transfer of Ag epoxy. Alternatively, one can use the ball bonder and create gold ball bumps on the bonding pads. After placing the first ball bond on the

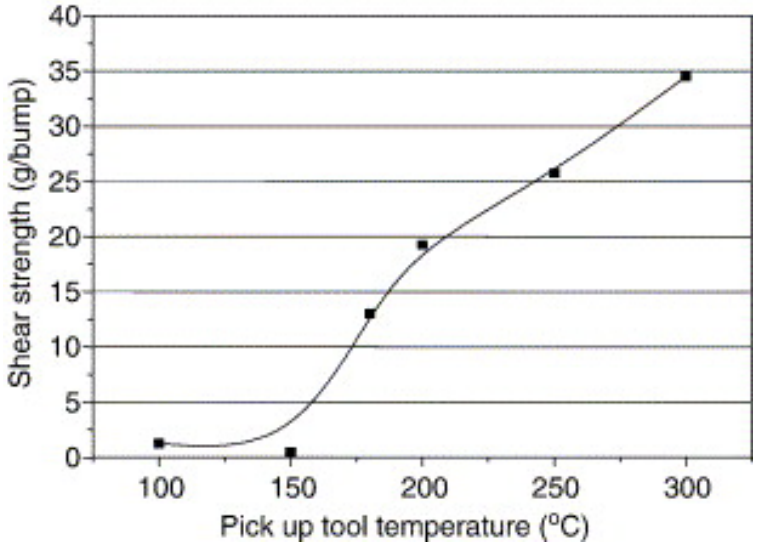

Figure 5·5: Graphs shows the bonding condition and shear strength for a Au - Au bond. Copyright © 2005 Elsevier B.V. reprint with permission [Ang et al., 2006]

bonding pad you can then remove its tail, leaving the ball bump or stud. The size of the ball bump can be adjusted between 16 – 40 μm in height.

The comparison of the two bonding materials (Ag epoxy and Au ball bumps) favors the Ag epoxy. When FC bonding with Ag epoxy the temperature reaches 175 C with 1 N of force for 5 minutes. In the case of the Au ball bump, the required temperature is 200 C with 20 N for 5 minutes. The shear strength of both bonding materials are sufficient to withstand the subsequent transfer, handling and ball bonding force. Measurements were recorded of the die to die edge separation after bonding with these materials. The Ag epoxy resulted in $\approx$ 11 μm separation and the gold ball bump depending on the size ball used were both greater. Using the smaller formed ball resulted in $\approx$ 16 μm separation and with the larger ball, $\approx$ 40 μm separation. Minimizing the separation between die is essential and Ag epoxy has the advantage.

Assembling and bonding the writer die set requires the target to be placed upside down so that the vacuum of the bonding head can pick up the die. To prevent damage to the target die when placed on the bonding stage a chip holder was designed and fabricated (see figure 5·6). The two-step recess of the holder allows the corners

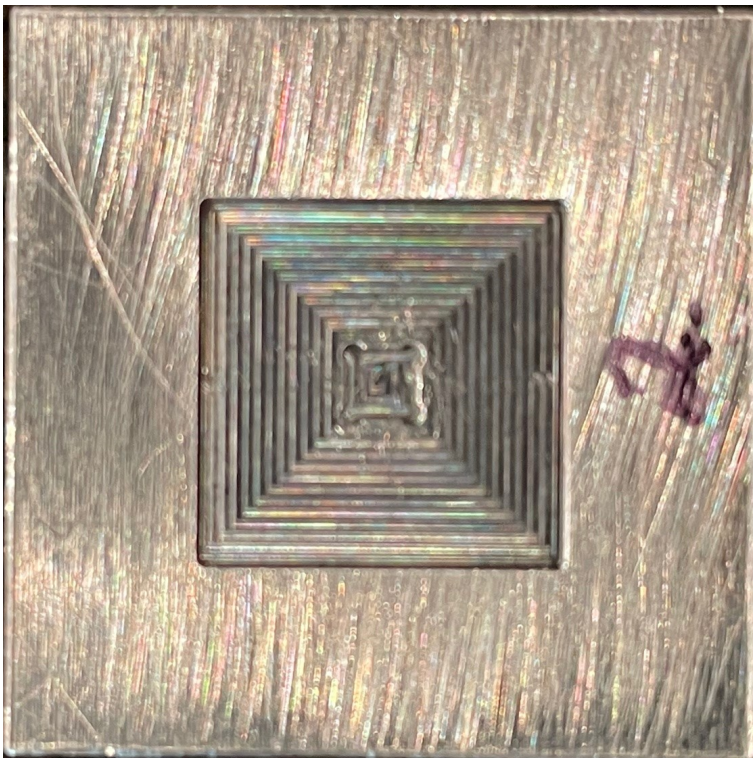

Figure 5·6: Image of die holder for the flip chip process.

to contact the aluminum holder while the MEMS area remains elevated. A second aluminum holder was created to fix the writer die in place. The FC bonder stage does have vacuum to keep the die in place but because of the BSE opening of the writer die, the writer plate is exposed and would be damaged. This holder has been problematic due to jagged and uneven edges of the writer dies. As discussed, the streets separating the die sets are made during the DRIE process. Due to mask pattern alignment inconsistencies, over or under etching by DRIE, and separation techniques, each die has 2 to 3 irregularly shaped edges. Ultimately, the die was

either too small allowing it to move within the holder or too big causing the die to be at an angle in the holder. Neither situation allows the precise alignment necessary between the two die. As such, a different method was created by attaching the die to a glass slide by the corners with super glue. The glass slide can then take advantage of the vacuum of the FC bonder stage and remain stationary during the bonding process.

During early testing, blurring was observed as an outer fringe on deposits using the assemble atomic scale 3D printer due to geometric dispersion. Equation 5.1 describes the relationship between the aperture opening, the source width, distance between aperture and target, and distance between the source and the aperture. [Vazquez-Mena et al., 2009]

$$d_g = \frac{h_a(d_s + d_a) + h_s d_a - \frac{d_s t_s}{2}}{h_s + \frac{t_s}{2}} - d_a \tag{5.1}$$

Equation 5.1 can be simplified to equation 5.2 based on the small thickness of the writer plate and the narrow aperture size.

$$d_g \approx \frac{d_s}{h_s} h_a \tag{5.2}$$

The diagram in figure 5·7 illustrates the geometric dispersion caused by the array of source plates and its relative position to the target. This dispersion can be minimized in two ways; reduce the distance between the writer plate and the target or increase the distance between the writer plate aperture and the source. The distance between the writer plate and the target is fixed by the PolyMUMPs process, however, the distance between the writer plate and the source can be modified. To increase this distance, a spacer die is created using a generic silicon wafer and the same BSE process as the writer die (see figure 5·8) . A 500 μm x 500 μm opening is etched into the center of the die with a venting feature connecting the center opening to one of the edges of the die. This allows access for the Ultra High Vacuum (UHV) to the

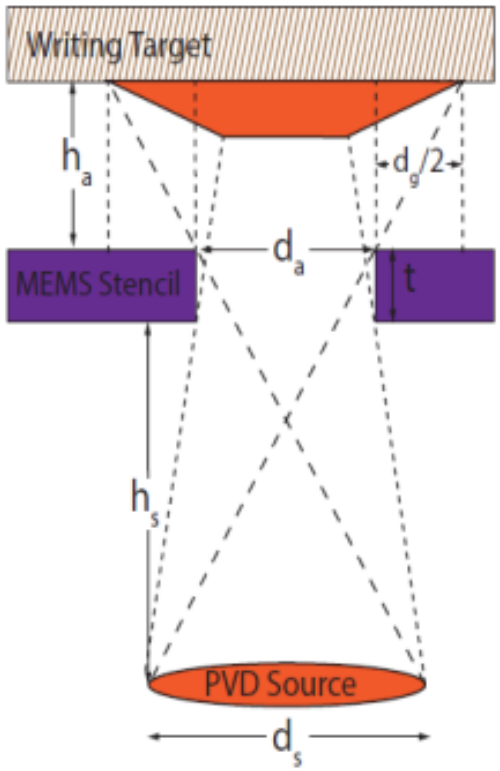

Figure 5·7: Diagram shows the factors which effect blurring.

stack of MEMS devices. Inserting this spacer die into the assembly stack doubles the distance between writer plate and target.

5.4 Bonding

The atomic scale 3D printer is assembled using the FINEPLACER® lambda FC bonder by Finetech. This bonder can apply a temperature of up to 400 C and 20 N of force. The fine adjustments of the bonding stage in the x, y, z and theta directions allow a placement accuracy of +/- 0.5 μm. This piece of equipment is particularly useful in research and development applications owing to its flexible and unique capabilities. A custom pickup tool specifically designed for the PolyMUMPs sized die permits the heating of the top die through the bonding head while the bottom die is

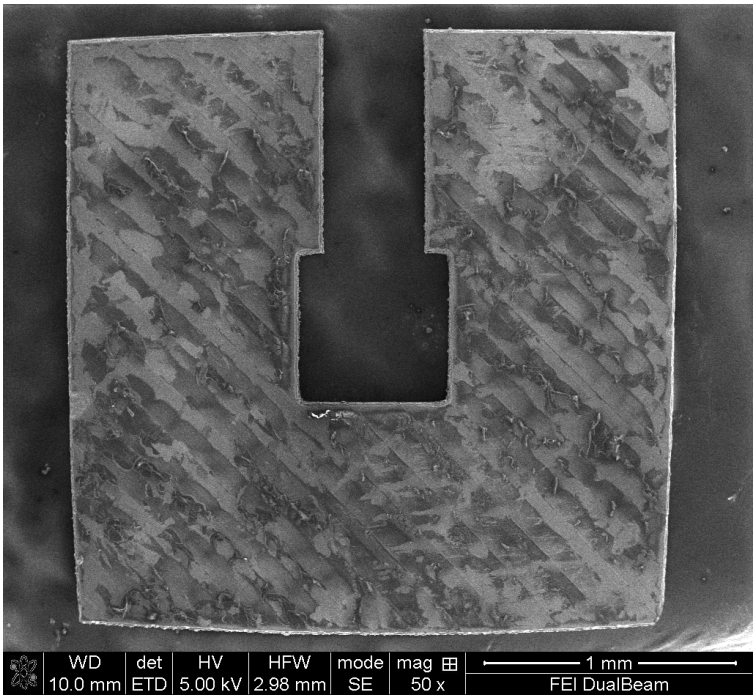

Figure 5·8: SEM image of the spacer die.

heated from the bonding stage. The FC bonder has two cameras, one of the top and the other on the side. The image from the top camera goes through a beam splitter to align the two die. The side camera allows the user to see the actual contact between the two die. Figure 5·9 shows a schematic of a generic FC bonder. [Lin et al., 2012]

As stated, the assembly process begins when the inverted source die is lifted up via the FC bonder pickup tool. The writer die is then positioned on the bonder stage. With the use of the beam splitter, the two die are aligned as in figure 5·10a (before) and 5·10b (after) using superimposed images and the alignment marks on both die. Depending on the accuracy of the milled aperture into the writer plate, additional fine alignment must be made to place the aperture exactly above the four probes on the target die as in figure 5·11. Once aligned, the two die are brought into contact. Figure 5·12 is an image from the side camera of the two die in contact. After the

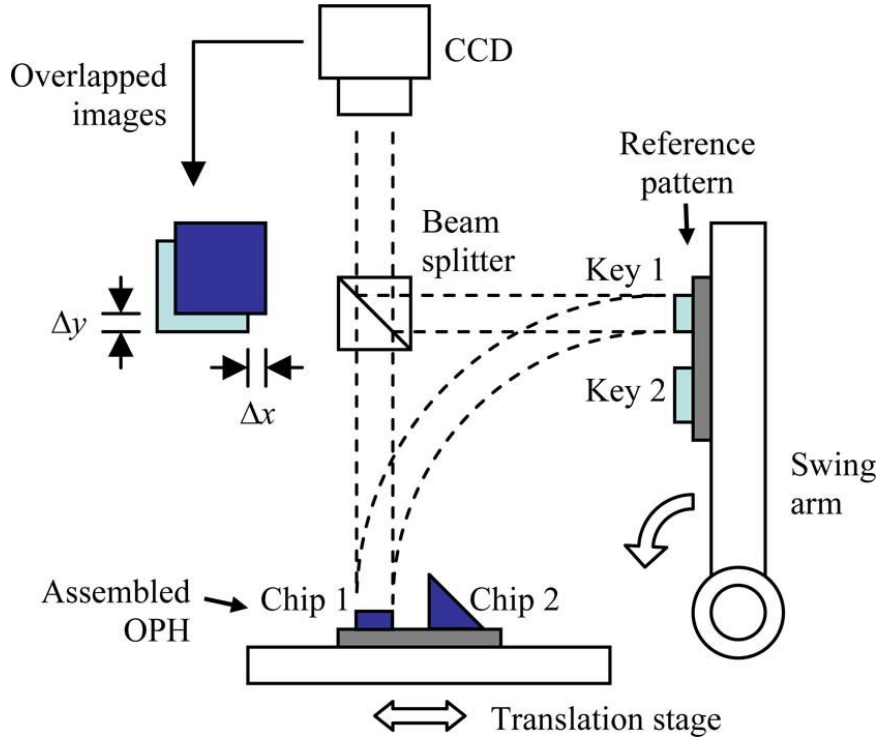

Figure 5·9: Schematic of generic Flip Chip Bonder. Copyright [2012] IEEE. Reprinted with permission from [Lin et al., 2012]

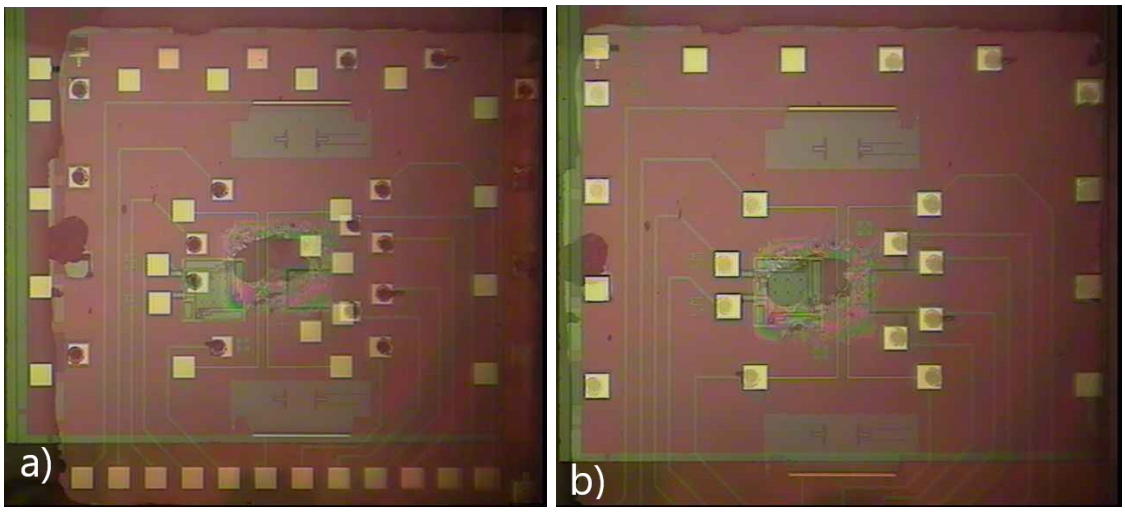

Figure 5·10: Images of the alignment process using the flip chip bonder: a) Superimposed images before alignment, gold pads with and without Au ball bumps not aligned. b) Superimposed images after alignment with all gold pads aligned.

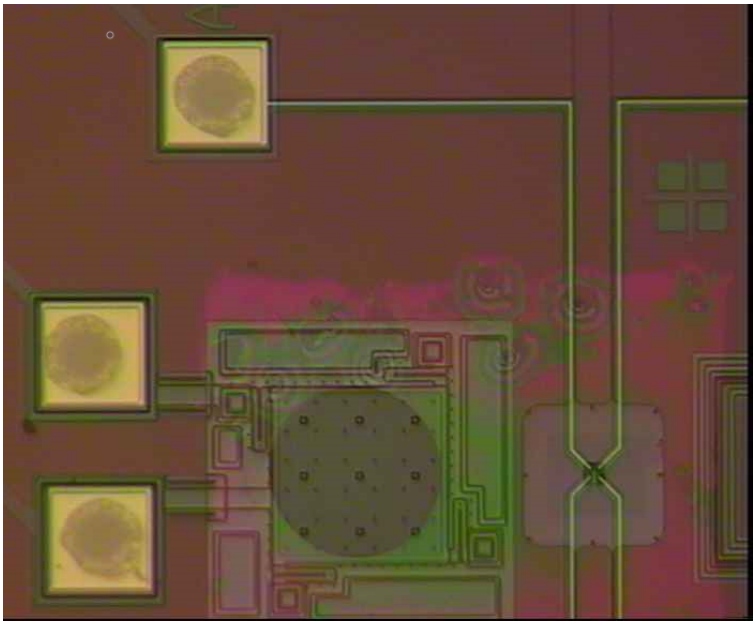

Figure 5·11: Closeup Image of the aligned die

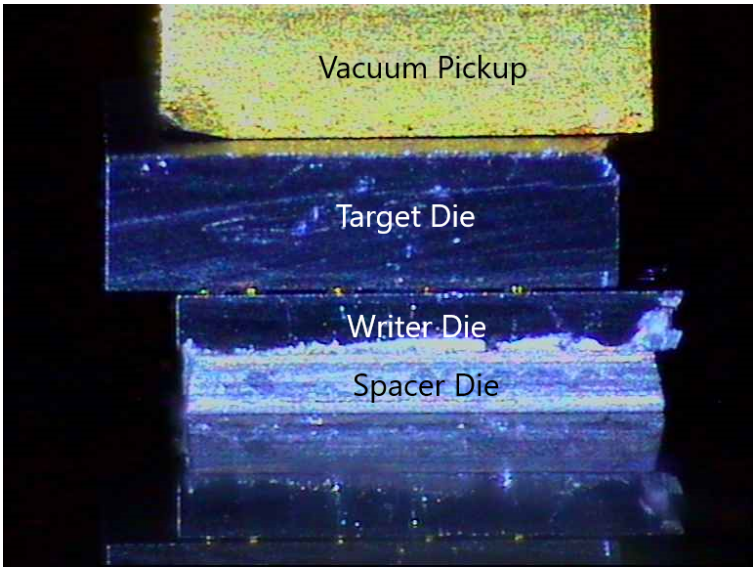

Figure 5·12: Side view image of the aligned die

required temperature and force has been applied for the appropriate time, the spacer die can be added to the stack. The combined source/writer stack is lifted above the stage while the spacer is positioned on the stage. A coarse alignment is made by matching the BSE opening of the spacer die over the writer plate and the side edges

of the spacer die with that of the writer die. Here, no bonding material has been placed between the two die to be bonded. Instead, a viscous non-conducting adhesive is applied between the outer edges of the two die. Use of the high viscosity super glue keeps the glue from wetting large portions of the writer die. Unintended wetting and spread of the super glue can cause the comb drive and writer plate to become inoperable. The side camera allows the application of the super glue to be applied with a probe tip as shown in figure 5·13.

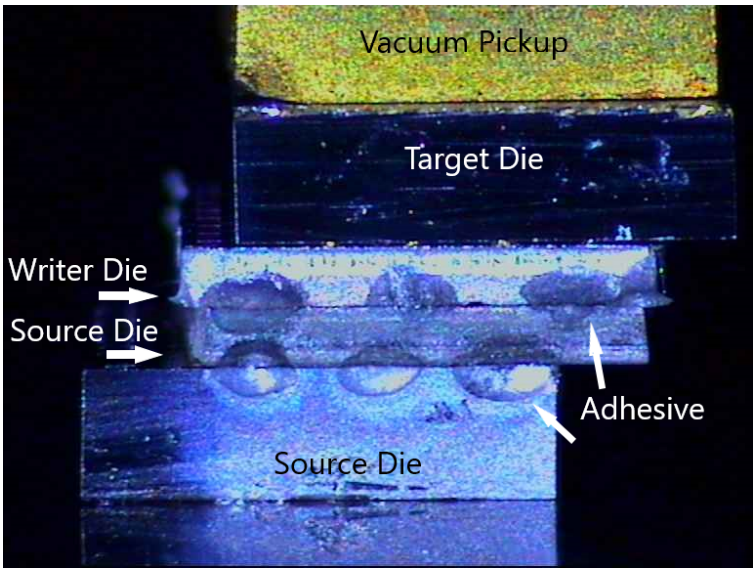

Figure 5·13: Side view image of the 3 die alignment showing the added adhesive.

After five minutes, the die can be rotated 180 degrees to bond the opposite side using the same technique. The last die, the source die, is bonded exactly as the spacer die was added. There is an alignment line along the front of the source die to prevent encroaching on the ball bonding pads space as discussed earlier. No heat or force is applied during this bonding process, which means the loaded material on the source die remains unchanged. With the addition of the source die the stack is complete and as depicted in figure 5·1.

Besides the FC bonding, the die stack requires ball bonding to a package so that it can be connected to the cryostat leads. The base of the stack can be attached to a leadless chip carrier (LCC) with Ag paint which allows thermal conduction from the cold finger of the cryostat. The electrical connections are formed with ball bonds as seen in figure 5·14. For a target die with just the four leads, this configuration is

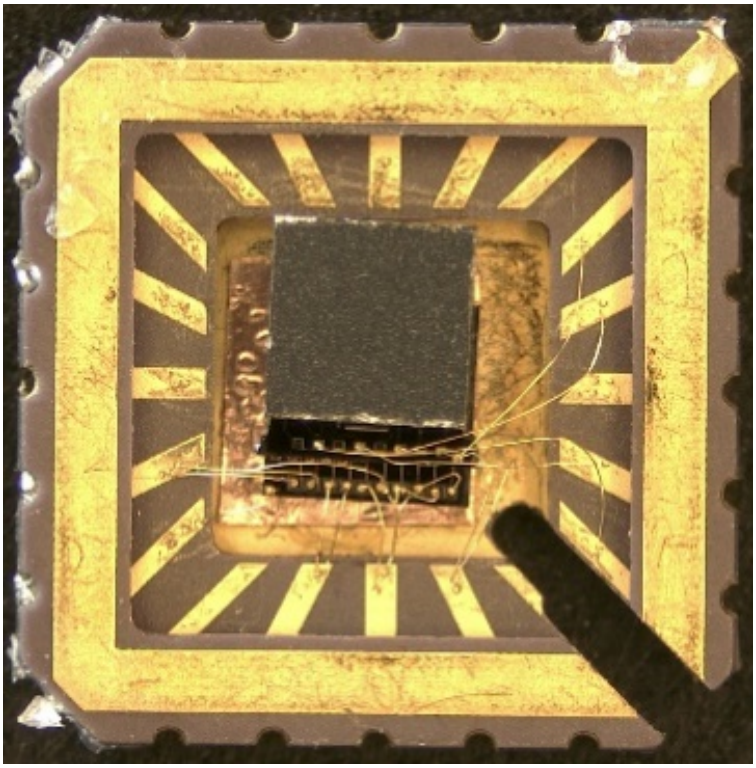

Figure 5·14: Overhead view of the die stack bonded to the LCC.

compatible. However, with the addition of the mass sensor and temperature sensor, the additionally required pads are impossible to access based on the orientation of the LCC bonding pads. To resolve this issue a printed circuit board (PCB) was designed and fabricated as seen in appendix A and figure 5·15. In this figure you notice that all the PCB bonding pads are oriented directly across from the die stack's bonding pads. This provides easy access during the ball bonding process. Table 5.1 displays

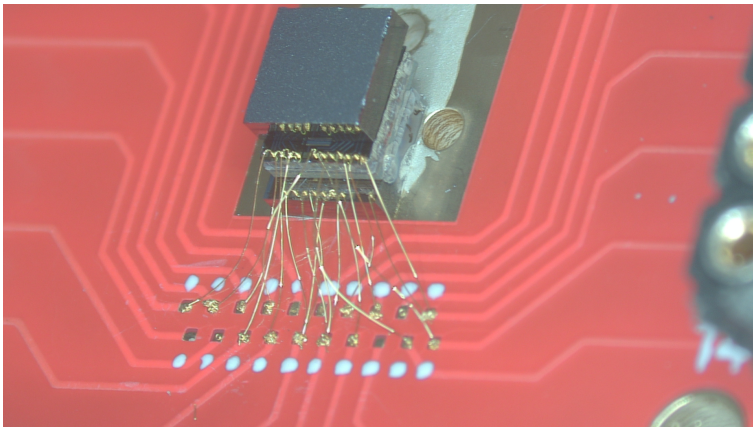

Figure 5·15: Overhead view of the die stack bonded to the PCB.

connections required and the applicable bonding sitse on this PCB. With this PCB configuration, the top die in the stack is the target die and it is in contact with the cold finger of the cryostat. A schematic of the atomic scale 3D printer layout is shown in figure 5·1.

5.5 Equipment Setup

Each MEMS device interfaces with electronics which are sensed by or controlled by a LabVIEW program. One program permits the user to adjust the bias on the source plates, adjust the current for the sensing leads of the target probes and the temperature sensor, and record over a dozen parameters including the cryostat temperature, mass sensor frequency, and various resistances associated with the other MEMS devices. There are two separate LabVIEW programs that are used in conjunction with this program. The first sweeps the frequency to help find the resonant frequency of the mass sensor. The second program drives the writer plate.

Once all the leads are properly connected as per table 5.1, some of the MEMS devices can be checked prior to the cool down in the cryostat. It takes ≈ 3 hours to reach ≈ 3 K. To return to room temperature (RT), it takes another 3 hours. Therefore, ensuring

Table 5.1: Cryostat Connections Table

Atomic Scale 3D Printer Connections		
Cryostat Connection Pin #	Source Type	MEMS Device
1	NA	NA
2	AC	Not Connected
3	AC	Probe Lead (V-)
4	AC	Temp. Sensor (V-)
5	AC	Not Working
6	DC	Common Ground
7	DC	Temp. Sensor (I-)
8	DC	Temp. Sensor (I+)
9	Ground	Writer Plate
10	DC	Temp. Sensor (V+)
11	DC	Source (I2)
12	DC	Source (G)
13	DC	Source (I1)
14	DC	Probe Lead (I+)
15	DC	Writer Plate
16	NA	NA
17	AC	Probe Lead (V+)
18	AC	Mass Sensor (1)
19	AC	Mass Sensor (2)
20	AC	Probe Lead (I-)

proper connections and working MEMS devices before cool down is preferred. The resistances for both zones on the source die loaded with metal is between 15 and 50 ohms. The source die has some redundant bonding options so adding another ball bond could resolve any connection issues. The temperature sensor can likewise be checked with a RT resistance value of around 450 ohms. The last check is to confirm that the leads on the sample probes are open. Appendix A shows the sensing scheme for the sample probes. This particular step ensures that the writer plate is not shorting out the leads or that during the FC bonding process, polysilicon debris from the DRIE has not created a similar connection. At RT the cryostat is not under vacuum so testing the mass sensor is not an option.

This completes the assembly of the atomic scale 3D printer and some of the techniques that permit a successful outcome.

Chapter 6

Atomic Scale 3D Printer Performance

This chapter reviews the performance of a fully assembled atomic scale 3D printer. Thus far, each die was evaluated independently in most cases. Here, we will review again each die but as part of an assembled printer. The target die will be reviewed last since it records the overall performance of the printer. It was noted that the designs for each die have been through a number of iterations and have evolved over time. What is presented in this chapter are the most recent designs and performance.

6.1 Source Die Performance

As discussed in the last chapter, with the initial assembly of the die set, substantial blurring occurred. The solution was to increase the distance, by a factor of two, between the writer plate and the source array. However, the atomic flux is inversely proportional to the squared distance between source and sample. Therefore, by doubling the distance we reduced the atomic flux by a factor of four. So improving ways to maximize the amount of material that can be evaporated was essential. An easy solution would be to increase the amount of material loaded on the source plates. The available Pb thermal evaporator had a small crucible, which could only load 500 nm onto the source plates at a time. Using the Ni masks, a source die was loaded multiple times and evaluated. The first observation was that in some cases it appeared that the Pb layers had slid off the source plate and shorted the adjacent plate, the source springs or with the substrate. In other cases, the Pb layer on the source

plate merely cracked on the surface. Repeating this same deposition while observing the evaporation confirmed the sliding Pb layers and the heating which only cracked the surface of the Pb. During these deposits the same technique and parameters had been used as with the thinner samples. A PWM of a 10 ms pulse with a 2 second delay between pulses was used while increasing the voltage 0.1 $\frac{V}{min}$. Due to the thickness of the loaded Pb (> 1.75 μm), only the bottom portion of the Pb sample had time to melt due to the latent heat and the source plate response time. Increasing the pulse width to 20 ms or greater provided sufficient time for the metal to evaporate.

With the increased pulse width, the Pb evaporated but left large Pb spheres on the plates. Estimates placed the amount of Pb remaining on the plates between 50 - 75 percent. The spheres remained even with higher applied voltages and increased pulse widths. A combination of surface tension and latent heat is believed to be the reason the spheres do not evaporate once formed. With longer pulse widths, one can observe the sphere pulsing and transitioning from solid to a liquefied sphere. A series of evaporations were conducted varying the amount of Pb loaded on the source plates from 0.5 μm to 1.75 μm in 0.25 μm increments. The same parameters were used throughout and the amount of Pb remaining on the source plates were recorded. The result was that loading 1.0 μm maximized the amount of Pb that could be evaporated. The result was the same for both the 3 x 4 array of source plates as well as the 5 x 6 array.

Another observation during these evaporations was that the Pb deposited with a Ni Mask still occasionally slid off the source die. The Ni mask was designed with a 90 μm x 90 μm opening to provide a 10 μm offset while aligning the mask with the source die. Alignment of the Ni mask typically results with deposited Pb overlapping one

edge of the source plate but being indented on the other side. The indented Pb edge on the source plate heats up faster than the remaining portions of Pb. This thermal energy is transferred across the bottom of the layer and the Pb shifts towards the side with the overlapping Pb. With the amount of Pb being reduced to 1.0 μm, the need for the Ni mask was also reduced. Instead, a simple mask to cover the bonding pads was used.

Based on the 1.0 μm loading results, an assembled die set was tested. A 5 x 6 source array loaded with 1.0 μm of Pb, was used with a U shaped aperture. The legs of the U shaped aperture are 7 μm x 22 μm with a 7 μm x 7 μm interconnect. After evaporating all sources under cryogenic conditions, the die stack was disassembled. The sample was then measured with an atomic force microscope (AMF). Nine measurements in various locations on the sample indicated that 58 $\pm$ 5 nm of Pb had been deposited. Figure 6·1 illustrates one of these measurements with spikes caused by Pb clusters.

Samples of $\approx$ 60 nm are more than sufficient to evaporate two different metals. Assuming roughly the same atomic flux of 30 nm per set of source plates, two metals could be evaporated through a static mask. However, for a dynamic mask a larger source is needed. Using the 400 μm x 400 μm source described in Chapter 3, more metal can be loaded on the source plate. Figure 6·2a shows the spacer die affixed to the source die. The spacer die opening is aligned with source plate and in figure 6·2b you can see the loaded source plate. The remaining die are bonded as described in Chapter 5.

A voltage of 9.5 V was applied to the source plate for 30 minutes and PWM was

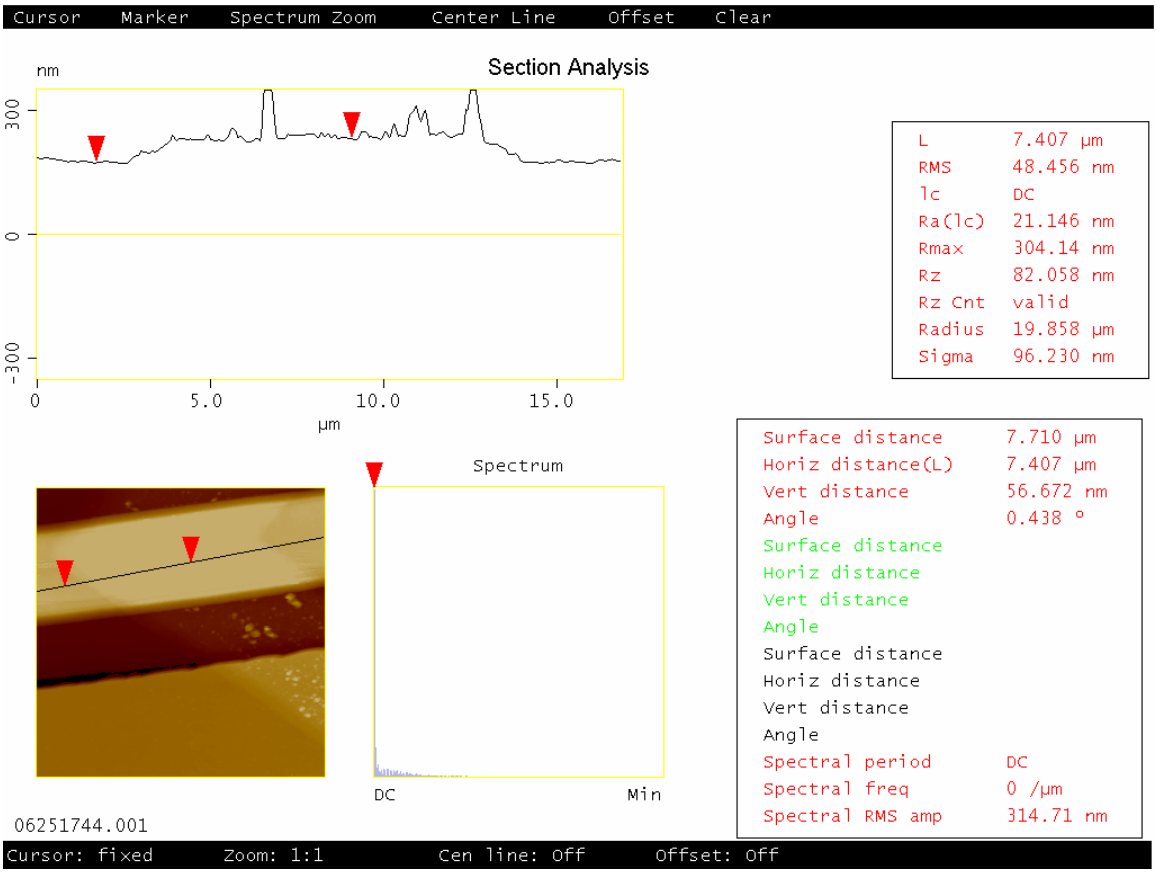

Figure 6·1: This figure shows that ≈ 60 nm of Pb was deposited through an aperture onto the target die with spikes caused by Pb clusters.

not employed. With a 3D optical profiler, the amount of Pb deposited by the 400 μm x 400 μm source plate was determined to be 156 nm. Figure 6·3 provides the profile measurement for this deposit.

A second evaporation was conducted with a different 400 μm x 400 μm source plate and die set. The purpose was to determine a higher evaporation rate and increase the amount of deposited material. This evaporation again started with a continuous 9.5 V applied to the source plate. After 30 minutes the voltage was increased by 0.5 V. This pattern was repeated until the source plate spring melted at 11.0 V. The evap-

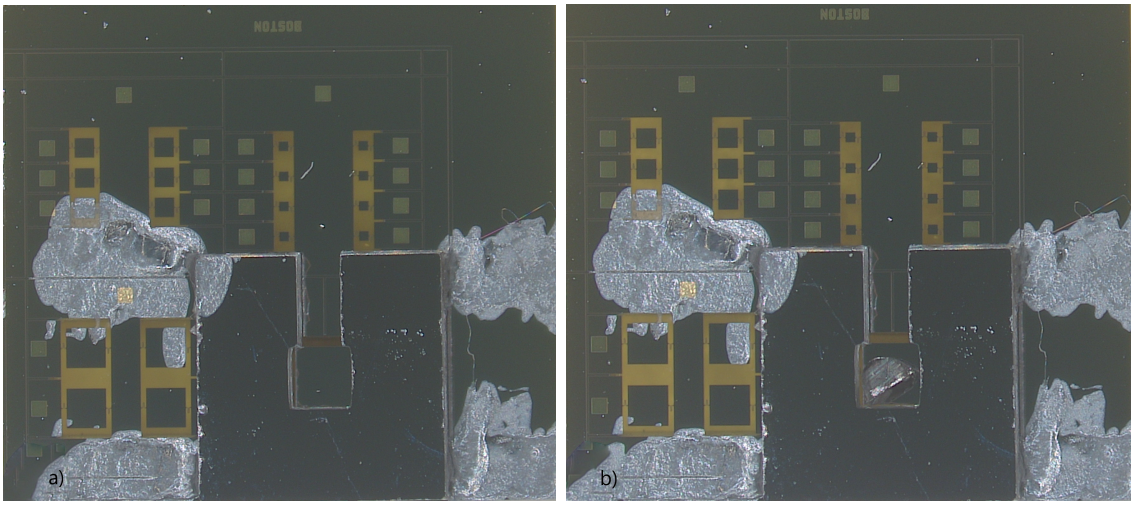

Figure 6·2: Images of the 400 μm x 400 μm source plate: a) spacer die aligned and attached to the source die b) Pb loaded onto the source plate and in the spacer void.

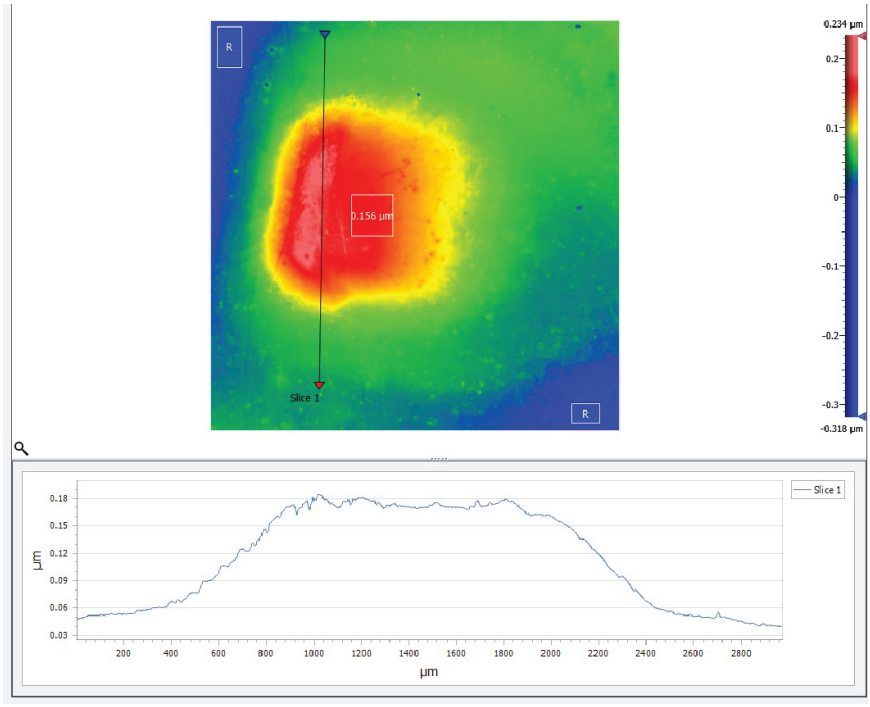

Figure 6·3: Image illustrates that 156 nm was deposited by a 400 μm x 400 μm source plate.

oration was conducted over $\approx$ 2 hours. During this time the cryostat temperature reached $\approx$ 6.5 K having started at $\approx$ 3 K. This sample was also evaluated with the

3D optical profiler and ≈ 3 μm had been deposited. The sample profile is in figure 6·4. Inspection of this target die indicated thermal damage to the mass sensor and the gold sensing leads.

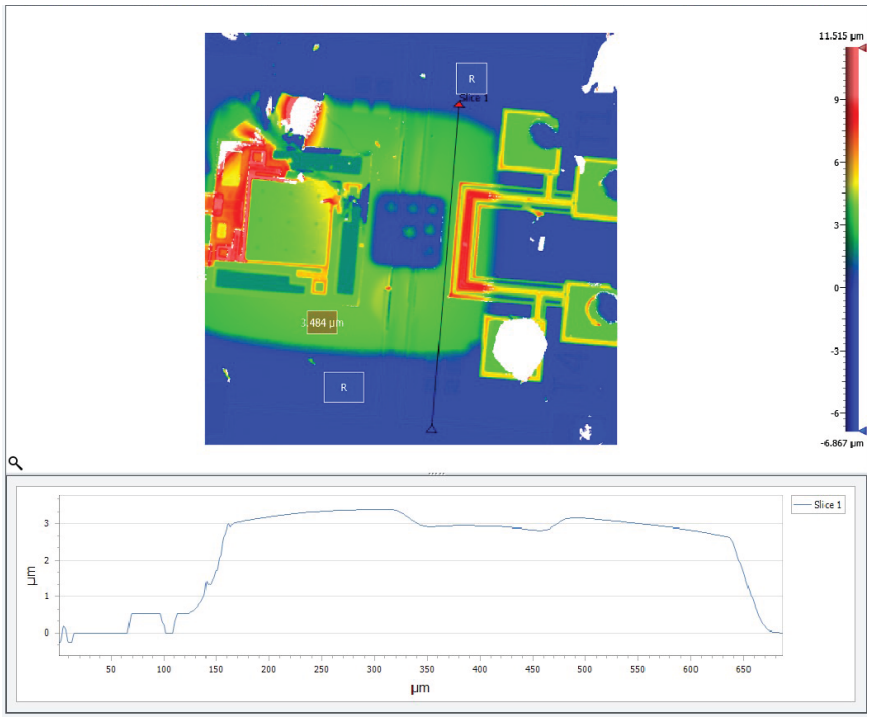

Figure 6·4: Image illustrates that ≈ 3 μm was deposited by a 400 μm x 400 μm source plate.

The 5 x 6 array was created to be able to deposit from two zones each with a different metal without damaging the other zone's metal. Ideally, metals could be evaporated either simultaneously or sequentially. Therefore, the separate source plate zones were analyzed. The analysis consisted of before and after optical images and source plates resistance comparisons of the loaded plates of the adjacent zone. Figure 6·5 shows there is no discernable change in the adjacent die color or grain composition.

A resistance comparison of the adjacent zone before and after the deposition showed no change. While two different metals have not been deposited from the same source

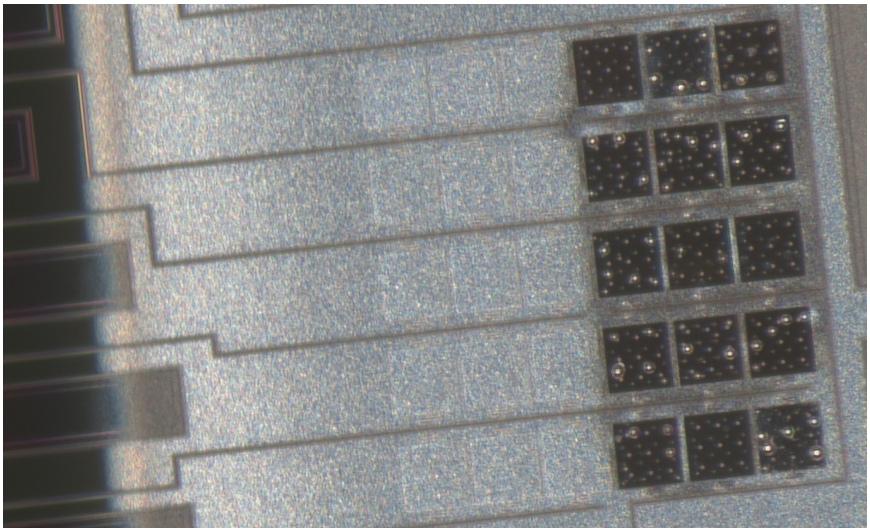

Figure 6·5: Image shows 5 x 6 array where half have evaporated Pb. The remaining source plates with Pb remain unaffected.

die yet, it is expected to have no effect on the adjacent source plates as the thermal images in Chapter 2 had shown.

The 5 x 6 array source die and the 400 μm x 400 μm source are capable of providing sufficient sample material in a variety of applications. The 5 x 6 array can be used when requiring controlled evaporations of small amounts with reduced thermal output. The larger source die is well suited for dynamic writing and thicker samples.

6.2 Writer Die Performance

In Figure 3·3 we showed that the writer plate can traverse +/- 10 μm in the XY plane. These measurements were taken with a single die without the BSE procedure or milled aperture. Consequently, it was the ideal situation. We now discuss the writer die as part of a 3 die stack. The writer die has two important features, its ability to move to a known spot and aperture alignment. These two features are evaluated here.

When the 3D atomic scale printer is fully assembled, one comb drive is still visible. The offset that allows access to the bonding pads also permits observation of the comb drive. A writer die and target die were FC bonded with Ag epoxy. Ag epoxy has the smallest standoff distance between writer plate and target die. The die set was configured under an optical microscope and various voltages (10 V - 70 V) were applied. The comb drive actuated and its displacement was measured. These measurements were consistent with those of Figure 3·3. To verify that the plate was actually moving and not just the comb drive another die set was prepared. Prior to FC bonding, a unique pattern was milled into the writer plate as seen in figure 6·6a. The full die set was assembled and half of the Pb was evaporated from a 3 x 4 array of source plates loaded with $\approx$ 500 nm of Pb. The deposition was paused and 20 V was applied to the writer die comb drive. After the evaporation, the die set was disassembled and SEM images were taken of the target die. Figure 6·6b shows the two sets of deposits separated by $\approx$ 1 μm. The unique shapes and the distance of 1 μm were the expected results.

There are a number of factors that affect the ability to deposit exactly where you want to with the atomic scale 3D printer. Perhaps the two most important are die to die alignment and aperture placement. Technically, the precision of the FC bonder ($\pm$ 0.5 μm) should be the limiting factor in the alignment process. However, the bonding material (gold ball bumps or Ag epoxy) can cause shifting in the FC bonding. This is especially true with Au ball bumps. Using holders and available FC bonder vacuum sources minimizes these effects. An aperture created with a FIB can be milled very accurately. However, positioning the aperture exactly in the middle of the writer plate (or anywhere else) may not be as precise. Besides the user error involved in aperture placement, other factors such as a slightly angled writer plate or a drifting

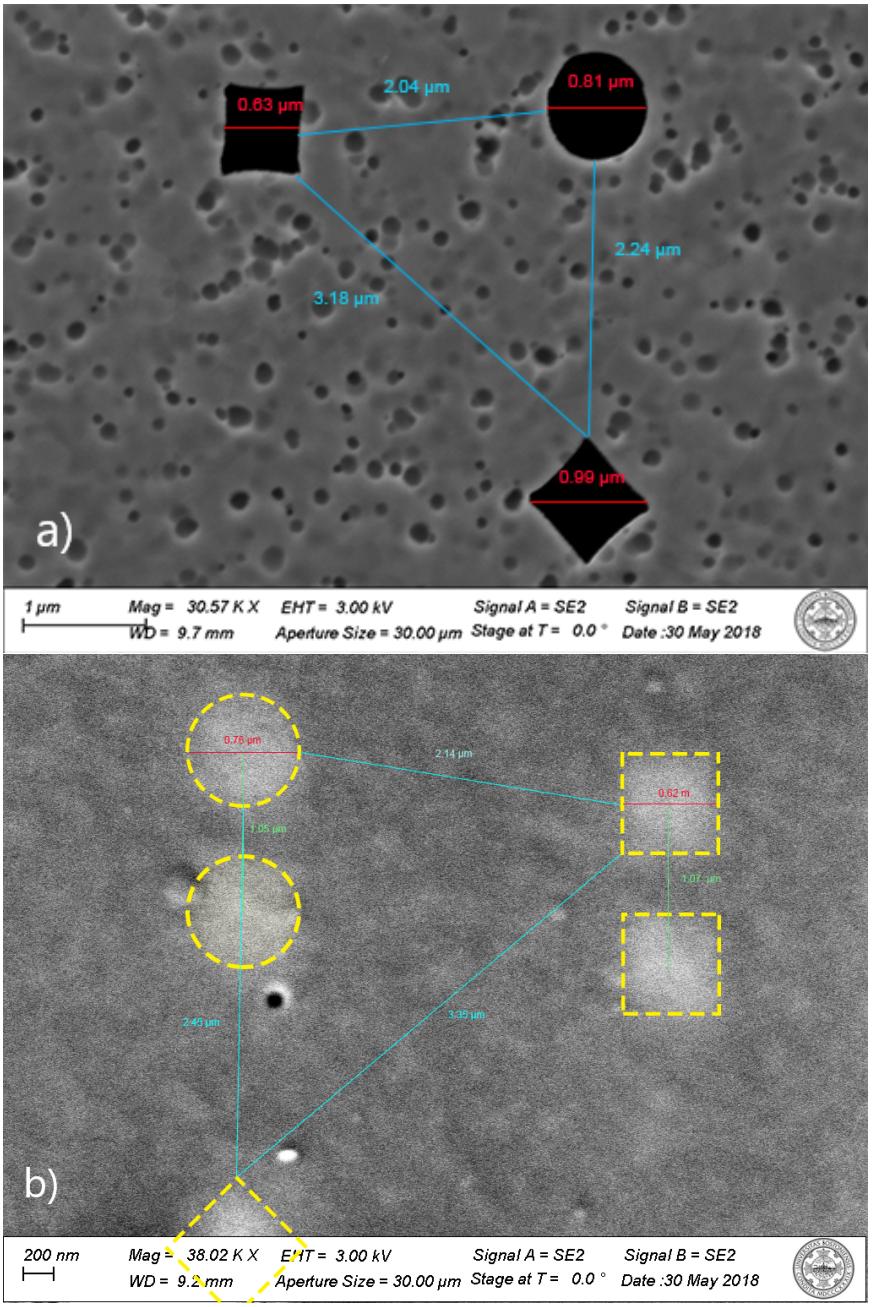

Figure 6·6: Image shows writer plate aperture and resulting deposit: a) Image of the aperture that was milled into writer plate b) Image shows the deposited Pb pattern from aperture after moving 1 μm.

FIB will also cause misalignment. Most of these situations can be controlled and the precision of the FC bonding remains the limiting factor. Figure 6·7 shows a series of

deposits with varying alignments issues. However, it is possible to align the aperture and deposit on the leads as seen in figure 6·8.

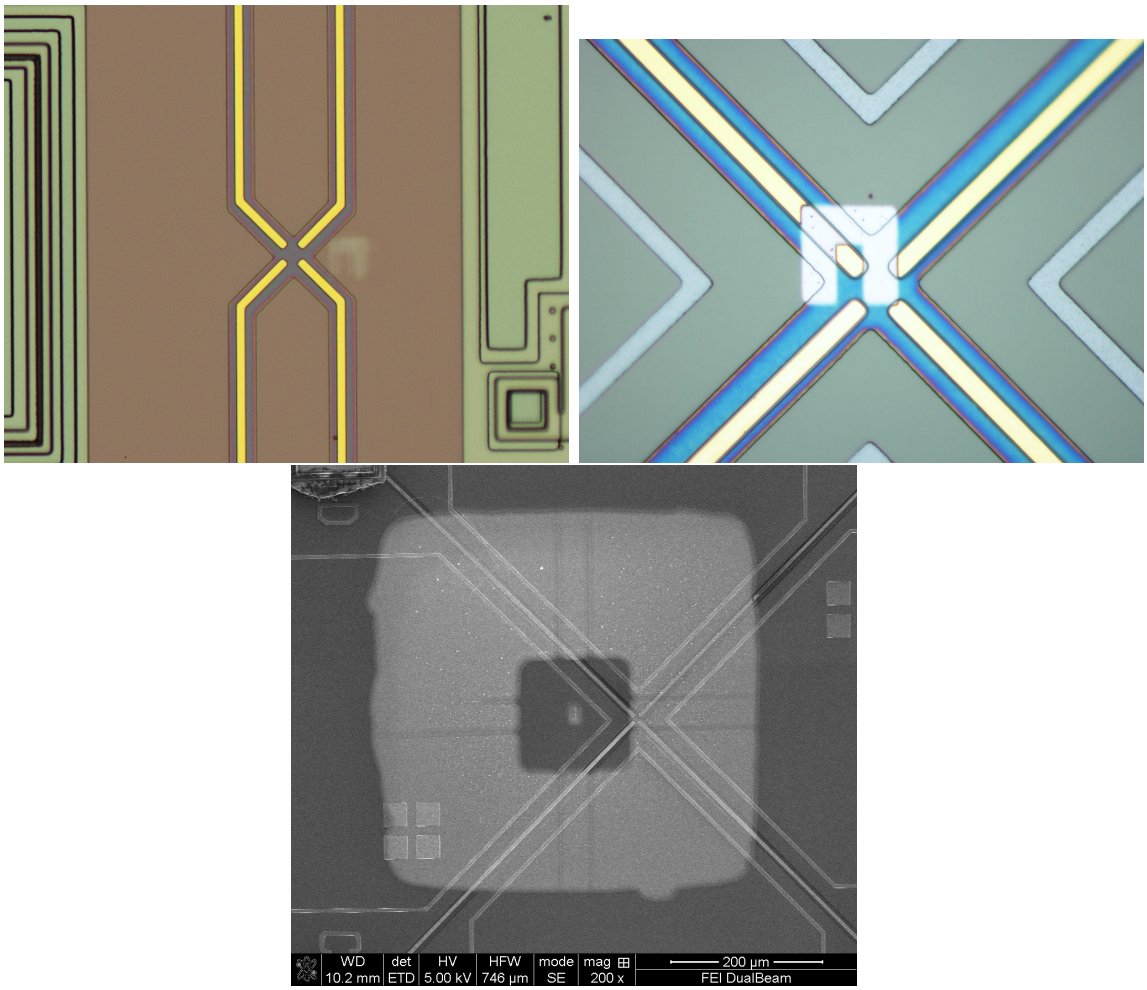

Figure 6·7: Images showing misaligned deposits

Two additional challenges are associated with the writer die. Both are related to the DRIE process. The first pertains to over etching by the DRIE process. The nitride layer is a good etching stop but only reduces the rate of etching compared to the silicon substrate. Continued etching either removes the nitride layer completely or can cause buckling. Neither situation is advantageous for use in the die set. Without

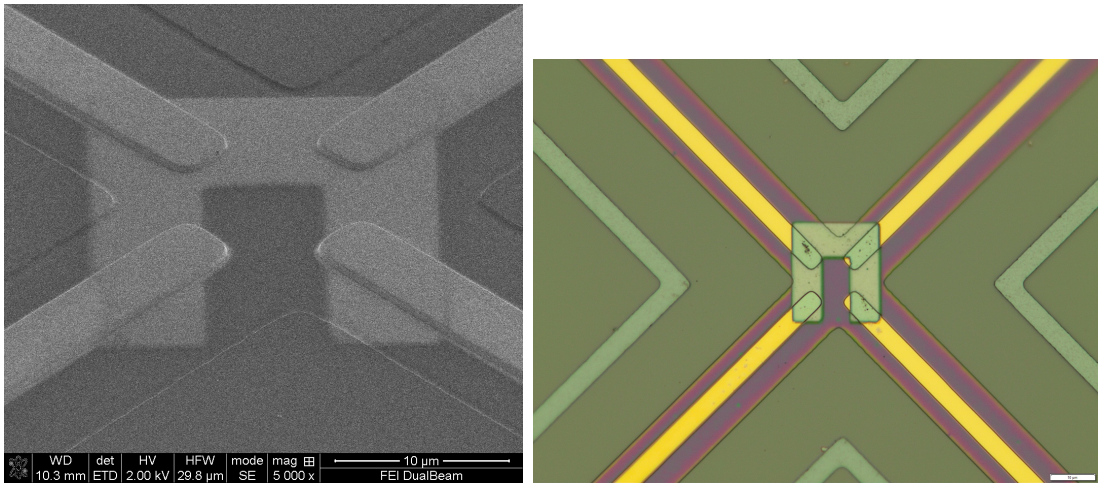

Figure 6·8: Images show proper alignment between the deposition and the sensing probes.

the nitride layer, sensing probe leads may connect outside the plate area. The edges of the polysilicon tend to turn up when milling breaches the nitride layer. This extra lip interferes with the writer tethers causing damage, elevating the plate, or severing the plate. The buckling of the nitride layer upon release can have the same effects. Therefore, care must be taken during the DRIE process.

While there can be challenges for the writer die, the writer plate has been shown to move and deposit in a predetermined spot.

6.3 Target Die Performance

With the source die evaporation maximized and the writer plate alignment optimized, the target die performance is now reviewed. The target die's three sensors will be discussed and then evaluated simultaneously. We begin with the mass sensor.

The mass sensor, besides being very sensitive to changes in mass, is equally sensitive to temperature changes. Figure 6·9 is a plot of the mass sensor frequency versus the

cryostat temperature. Data was collected from 3 K to 9 K in both directions. The

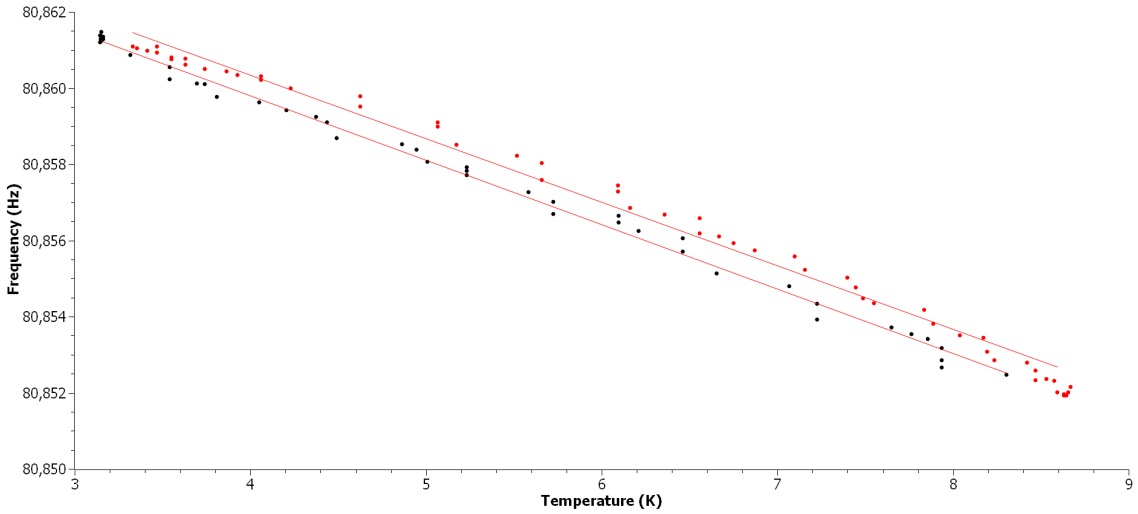

Figure 6·9: Graph shows how the mass sensor frequency changes with temperature.

warmup data is in red and the cool down data is in black. As seen in the graph there is a linear fit between frequency and temperature for the mass sensor. This indicates a change of $\approx 1.7\ \frac{Hz}{K}$.

The cryostat used for these measurements has a base temperature of 2.92 $\pm$ 0.02 K . To maintain a 3 K temperature, the cryostat is required to continuously transfer heat. The cycling of this heat exchange has a period of roughly 7 seconds. Figure 6·10 is a plot of the cryostat temperature over time. Here, the baseline temperature background is recorded. During this 7 second cycle, the cryostat temperature fluctuates by $\pm$ 8 mK in a sinusoidal pattern. The response of the mass sensor is also plotted on the same graph. The cryostat fluctuations in temperature causes a similar response from the mass sensor with a $\pm$ 200 mHz change over the same period.

Since the mass sensor is very sensitive to temperature changes, the response to the heat from the source plates was of interest. Unloaded source plates were used with

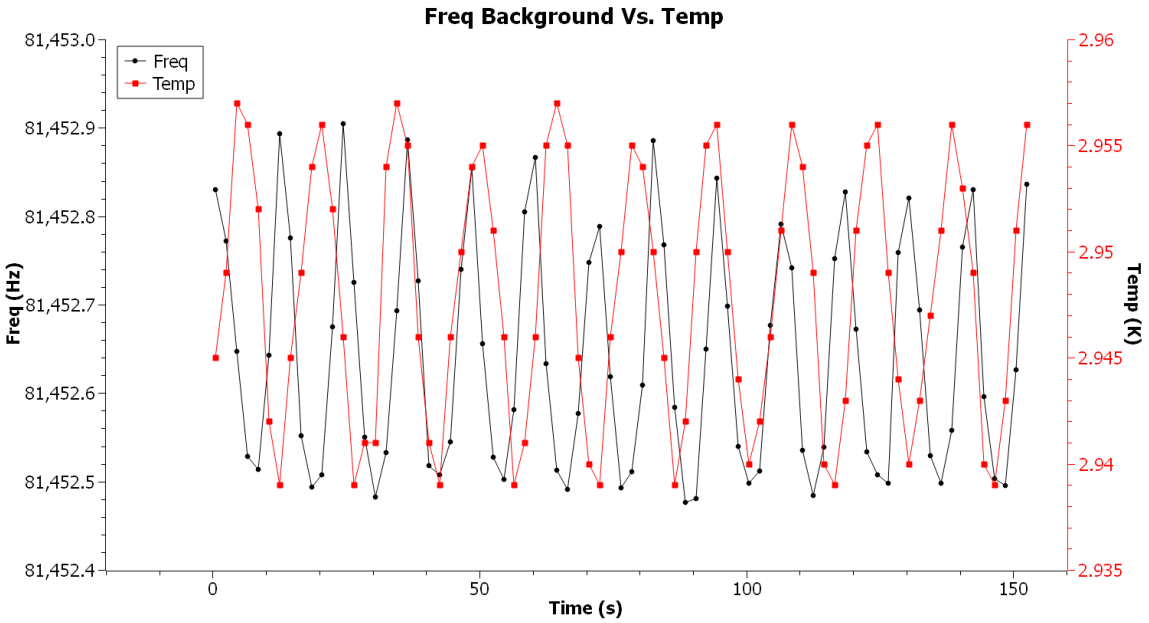

Figure 6·10: Graph shows the cycling of the cryostat and its effects on the mass sensor and temperature.

5 V applied using a 15 ms pulse with a 2 second rest period. The response of the mass sensor is recorded in figure 6·11. The PWM basis was applied for 3 minutes and

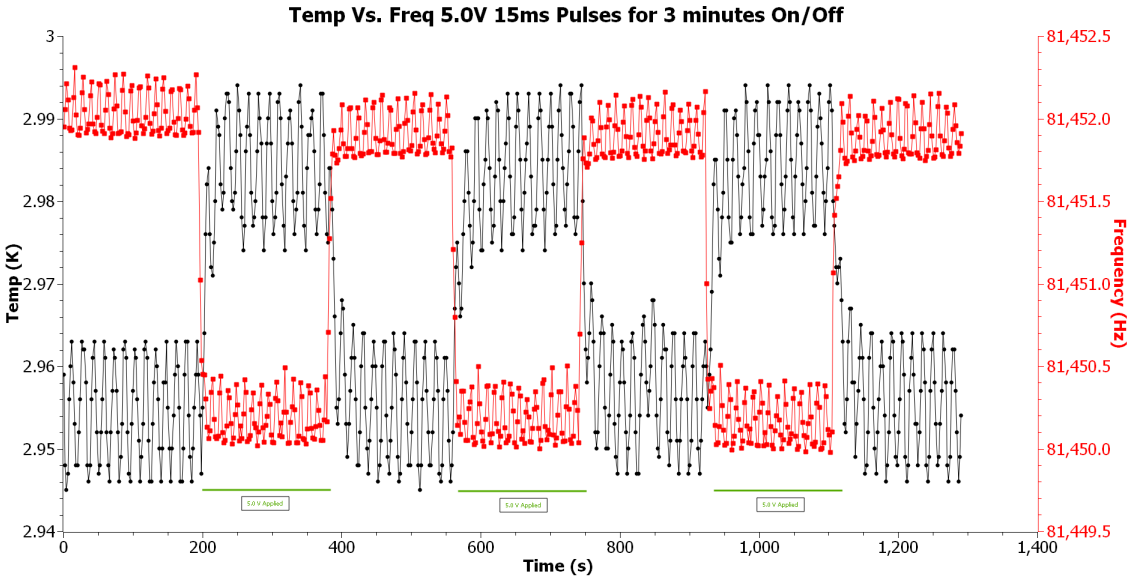

Figure 6·11: Graph shows the cycling on and off of source plates and the effect on mass sensor and cryostat temperature.

then turned off for 3 minutes and this cycle was repeated for $\approx$ 20 minutes. From the graph, you can see turning on or off the pulse has a frequency shift of roughly 2 Hz and a corresponding cryostat temperature change of only 40 mK. Based on the rate of change in frequency from figure 6·9, we would expect a change in temperature of 1.7 K. This difference will be discussed shortly.

The temperature range we are most interested in is between 3 K and 10 K. There are a number of metals, which are superconducting within that range. The temperature sensor located on the substrate of the target die is accurate even at these lower temperatures. Figure 6·12 shows the graph of the temperature sensor resistance versus the cryostat sample temperature. Here the temperature of the cryostat was increased slowly from 3 K to 10 K. The result of figure 4·8 shows a linear function where the resistance increases by 0.585 $\frac{\Omega}{K}$. As we saw in figure 4·9, the same linear fit does not apply outside this range.

For the atomic scale 3D printer to be used for research purposes, the four probes on the target die are perhaps the most important feature. They are capable of sensing single digit nanometer films due to the thinning and smoothing process of the nitride layer. Typically, the PolyMUMPs process is extremely reliable and produces MEMS devices with repeatable characteristics due to their high quality process. However, after troubling measurements of the target die, it was determined that the thinning process had breached the nitride layer. This caused all the gold leads and gold pads (including the structural ones) to be connected through the substrate. This defect was present on four consecutive PolyMUMPs runs. The time between runs is about four months. Therefore, for well over a year, new versions of the target die were defective. A failing furnace at PolyMUMPS was replaced and the process recalibrated

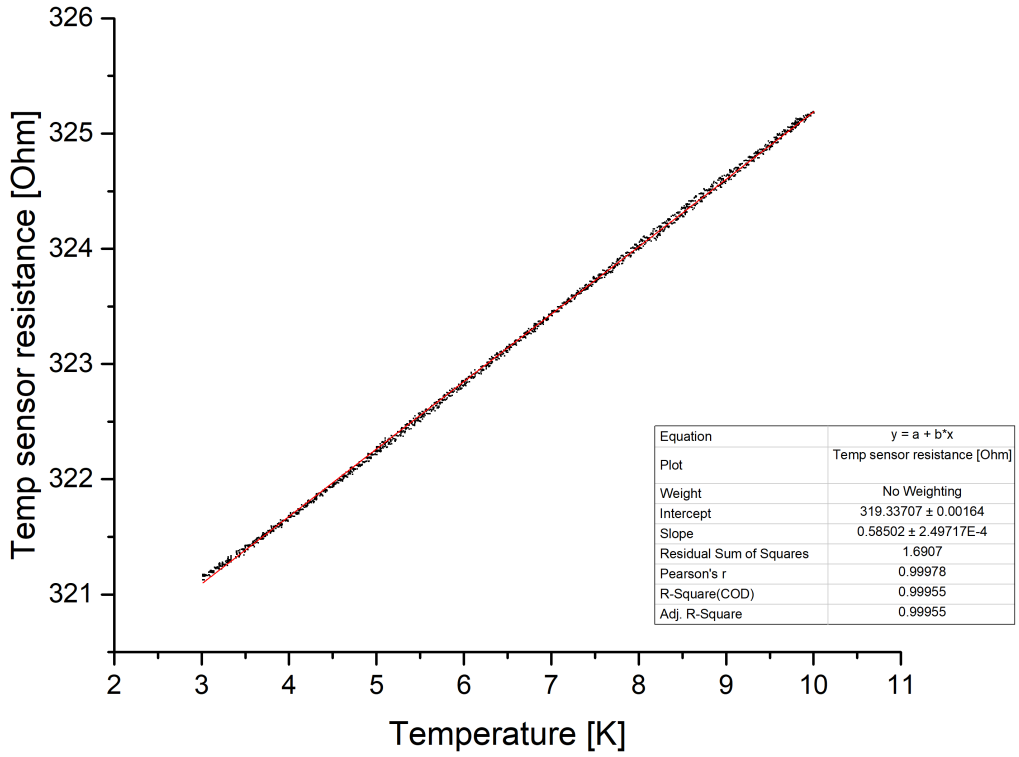

Figure 6·12: Graph of the temperature versus the cryostat temperature.

and the problem corrected.

Similar to the writer die the target die has had a few challenges also beside the PolyMUMPs issue. After the evaporation was completed on a fully assembled 3D printer, there were issues with either no connection or very high resistance not indicative of a Pb metal connection. Due to the Poly 0 leads on the writer die, a 2 point resistance measurement will be in series with the two Poly 0 leads that have a combined resistance of between 4 $k\Omega$ to 8 $k\Omega$. Additionally, in the cases where the resistance was extremely high, the resistance decreased with an increase in temperature. The failure mechanisms were traced to three conditions. The first was the

contact resistance between the thin film and the edge of the Au leads. Figure 6·13 shows how shorting can occur through stray currents passing through the film during deposition or after. Another type lock-in amplifier along with grounding mechanism

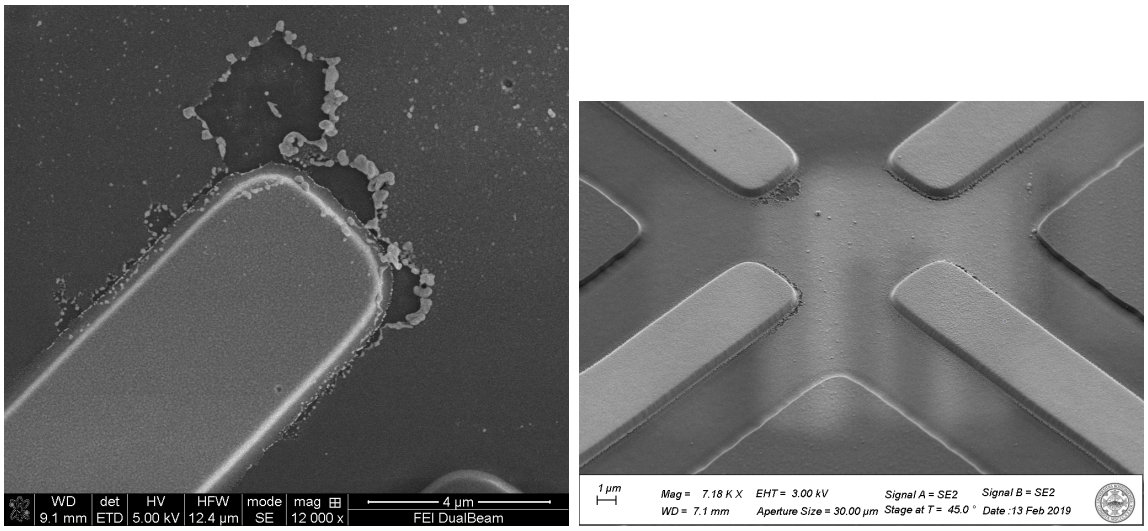

Figure 6·13: Images of sample leads shorting.

resolved this issue. The possibility of the writer plate contacting and shorting the leads was another issue. Measurements were made with a 3D optical profiler before bonding the writer die with the target die. Optical measurements were also made through the BSE after bonding to confirm the plate was not contacting the leads. The last issue concerned the Ag epoxy. Unexpected measurements at times pointed towards an issue with the Ag epoxy. The exact mechanism for failure is unknown. However, the Ag epoxy became unreliable whether due to improper mixing, age of the epoxy, or the effects of cryogenic cooling is still to be determined. When the Ag epoxy was replaced with the gold ball bumps, the lead connection issues were resolved.

As stated one of the goals is to use this atomic scale 3D printer for research and examine various materials at cryogenic temperatures. Therefore, to validate this approach, the assemble stack of die needed to deposit a thin film and record a su-

perconducting transition. During the evaporation process, we would also need to measure with the mass sensor and the temperature sensor. Initially, only a two point resistance measurement was achieved. Eventually, a four-point measurement of Pb undergoing a superconductive transition was documented. Figure 6·14 shows this outcome. In figure 6·14, by slowly varying the cryostat temperature, a superconducting

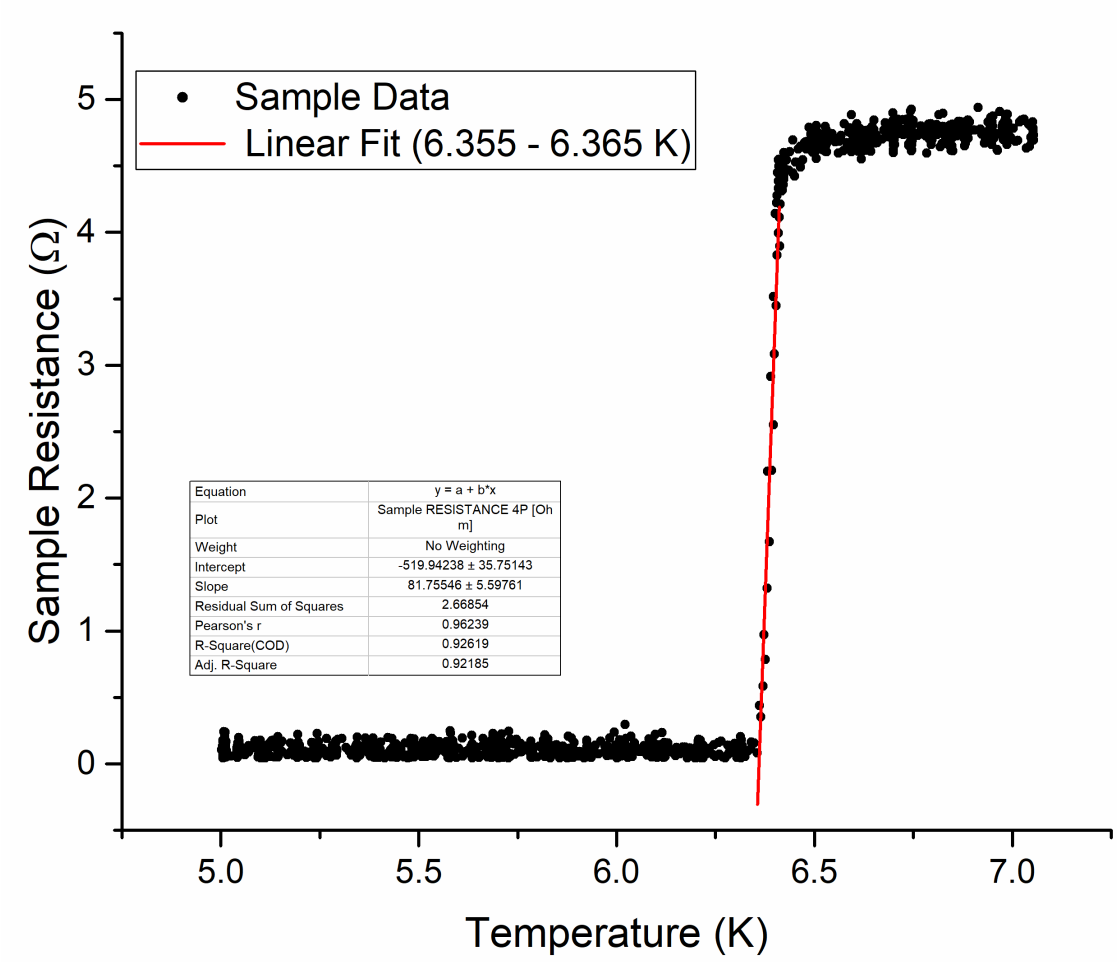

Figure 6·14: Graph of superconducting transition of Pb

transition temperature (Tc) takes place at 6.35 K ± 35 mK. The AFM measurement of this sample revealed it to be ≈ 20 nm. During the deposition of this film the pulse level, the cryostat temperature, the mass sensor and temperature sensor data were all recorded and can been seen in figure 6·15.

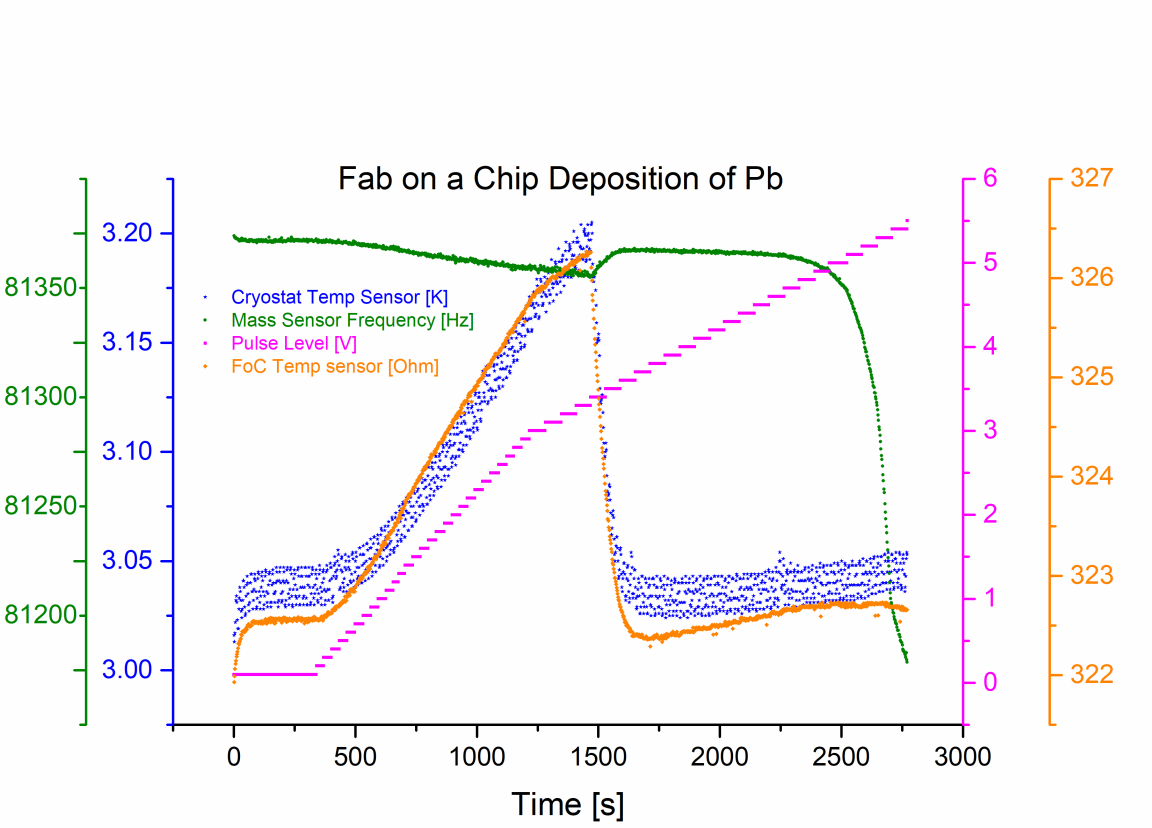

Figure 6·15: Graph shows the data that was recorded during the deposition of 20 nm of Pb

Being able to anneal a thin film by controlled heating is another desirable feature in such a device. Source plates are obviously excellent heaters. Unloaded source plates or expended source plates are capable of serving in this role. Figure 6·16 shows the heating of the superconducting film with the expended source plates. By increasing either the voltage of the pulse by 10 mV increments or the pulse width by 1ms, one can fine tune the emitted heat. In figure 6·16 by using this fine tuning of the heaters, one can pause on the shoulder of the superconducting transition. Another interesting observation in figure 6·16 is that the cryostat temperature maximum was $\approx$ 3.13 K. However, the Tc was established earlier to be $\approx$ 6.35 K. Therefore, it is

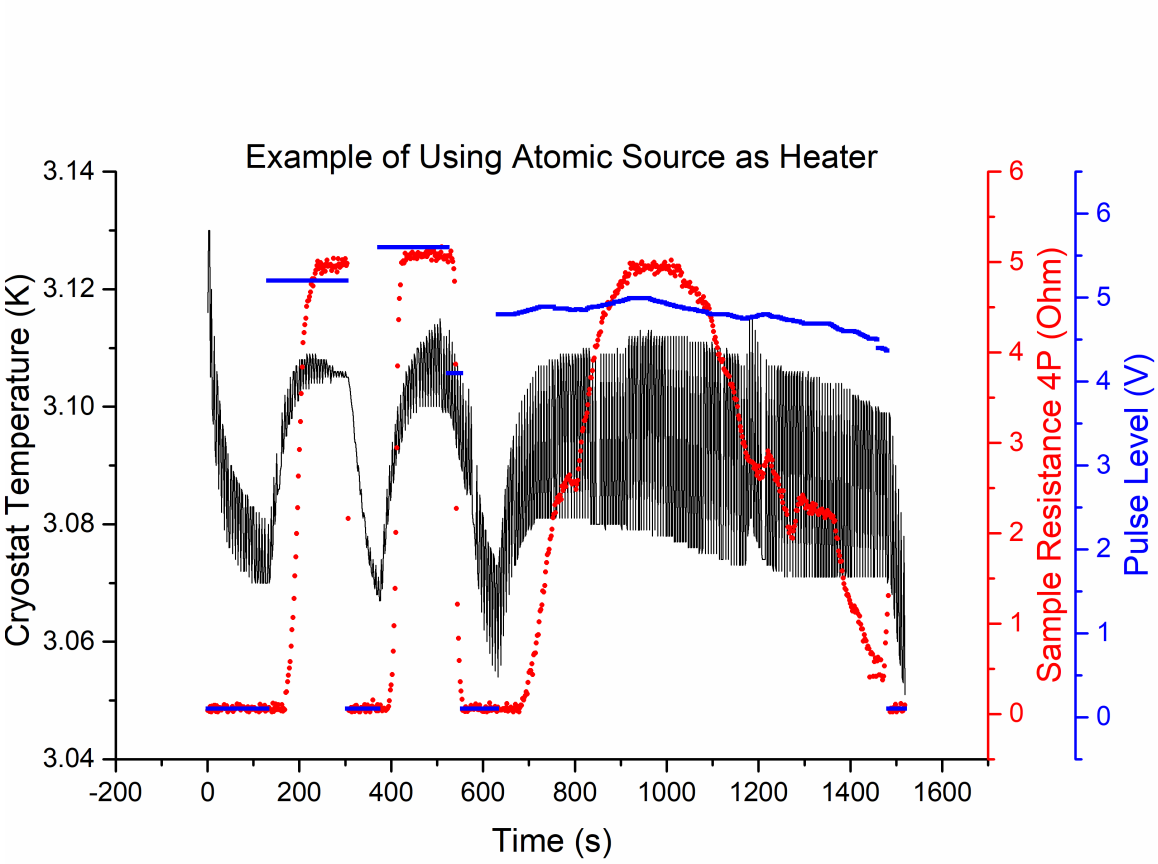

Figure 6·16: Graph shows the source plates being used as heaters. Sample is heated with source plates with precise control.

assumed that the source plates heated the Pb film above 6.35 K. Earlier in this sections a similar situation was observed when the mass sensor frequency change due to the source plates heating indicated a greater change than the cryostat showed. This difference is most likely created by the proximity of the source plates to the mass sensor and temperature sensor ($\approx$ 600 μm away). The radiant heat from the source plates is shielded from the cryostat temperature sensor by the silicon substrate and the thermal conductance is sufficiently reduced by the cold finger location on the opposite side of the target die substrate as in figure 5·1.

The atomic scale 3D printer has been fabricated and tested and is capable of de-

positing thin films at specific locations while monitoring the mass deposition and the accompanying temperature. Annealing is also possible using the source plates. The great advantage of this system is that it can deposit quenched condensed thin films *insitu*. We have shown that this system is compatible with cryogenic environments and multiple metals can be evaporated from the source plates either sequentially or consecutively. Ultimately, it mirrors the abilities of a fabrication facility, but is on a chip.

Chapter 7

Conclusion and Future Outlook

7.1 Summary of Atomic Scale 3D Printer

The atomic scale 3D printer has been shown to have unique fabrication capabilities due to its system of MEMs devices. The reaction speed, reliability, and precision of the actuators enhances the printer's performance over macro scaled systems. Likewise, the response time and accuracy of the sensors are unsurpassed. In chapter 2 we discussed the ability of the source die to evaporate thin films at low temperatures. With resistive heating from the springs, the source plates were heated sufficiently to evaporate the 1 μm of loaded lead. The evaporation from a 5 x 6 array resulted in $\approx$ 60 nm thick film. Substituting the larger 400 μm x 400 μm source plate allowed a larger quantity of lead to be load on the plate. The evaporation from this source plate produced $\approx$ 3.0 μm thick film or 50 times the amount of the 5 x 6 source array.

The heart of the atomics scale 3D printer was shown to be the writer plate. Powered by the electrostatic comb drives, the plate can be move in a 20 μm x 20 μm area. Micrometer to nanometer-sized apertures can be milled through the plate with a FIB. Movement of the plate proportionally responds to the square of the applied voltage. Precision film placement has been achieved with the writer die.

The available sensors on the target die provide all the necessary tools to analyze the deposited film. The temperature sensor has a linear response to the cryostat tem-

perature changes within the range of interest (3 K to 9 K). The temperature sensor is also responsive outside this range for longer annealing processes up to 30 K or more. The location of the temperature sensor on the die substrate allows it to be more sensitive than the cryostat when evaporating with the micro array of sources. The mass sensor was shown to be equally sensitive to the source array when heated. However, the mass sensor's main contribution remains accurately measuring the amount of metal deposited. It was shown that the frequency change of the mass sensor is proportional to the mass deposited on the mass sensor. This was illustrated in figure 6·15.

The sensing probes are configured to allow various type thin film measurements. The low profile of the leads connection to the nitride layer serves as an excellent conduit for the deposited material. As stated, thin films of only $\approx$ 2 nm have been measured with these fabricated type leads. When assembled the three die and a spacer die provide a novel capability. It was shown in figure 6·15 how a superconducting film of $\approx$ 20 nm was fabricated and then measured with the atomic scale 3D printer. The *in situ* capability leverages the collection of MEMS devices and their performance in creating a FoC.

7.2 Engineering Enhancements

Scott Adams is credited with coining the phase, "Engineers like to solve problems. If there are no problems handily available, they will create their own problems". While the atomic scale 3D printer has achieved its desired goals, further enhancements could be on the design horizon. Reducing the blurring of any evaporation is always a high consideration. One readily available solution is the pop up writer plate design with five degrees of freedom. [Barrett et al., 2019] The writer plate is elevated with bimorphs and the z direction can be controlled with capacitive sensing. This feature

would reduce writer plate to sensing probe distance to zero if desired. Alternatively, one could increase the size of the writer plate die gold pads for the interconnection of the die. This could allow the FC bonding to be achieved, without the gold ball bump, which decrease the z axis distance.

If the larger 400 x 400 source die were to be used, there is no reason why the writer plate die design could not be comprised with a similar footprint of two to four currently sized writer die. This design would allow for the pop-up writer plate, a shutter, a second mass sensor, and independent heaters along with the associated increase in bonding pads. Perhaps not all these design changes could be achieved with the PolyMUMPs. If a custom fabrication was to be considered, the BSE procedures might be part of the foundry's fabrication process.

These enhancements would extend the capability of the printer and increase the ease of use. Or maybe, Scott Adams is right.

7.3 Future Outlook

Where does the atomic scale 3D printer fit in the nanofabrication community? How can its capability be best utilized? These are two very good questions, which can now be addressed knowing the capabilities of this fabrication technology. Reviewing figure 7·1 [Imboden et al., 2014a] one quickly realizes the name of this capability "atomic scale 3D printer" is at two ends of the spectrum. Traditional 3D printers are on the upper right side of the graph indicating larger printed materials at a fast throughput. The atomic scale portion of the name places it in the bottom left side of the graph, where we are at the nanometer scale size but the areal throughput is very small. It is not surprising that we find atomic calligraphy centered between those two ends

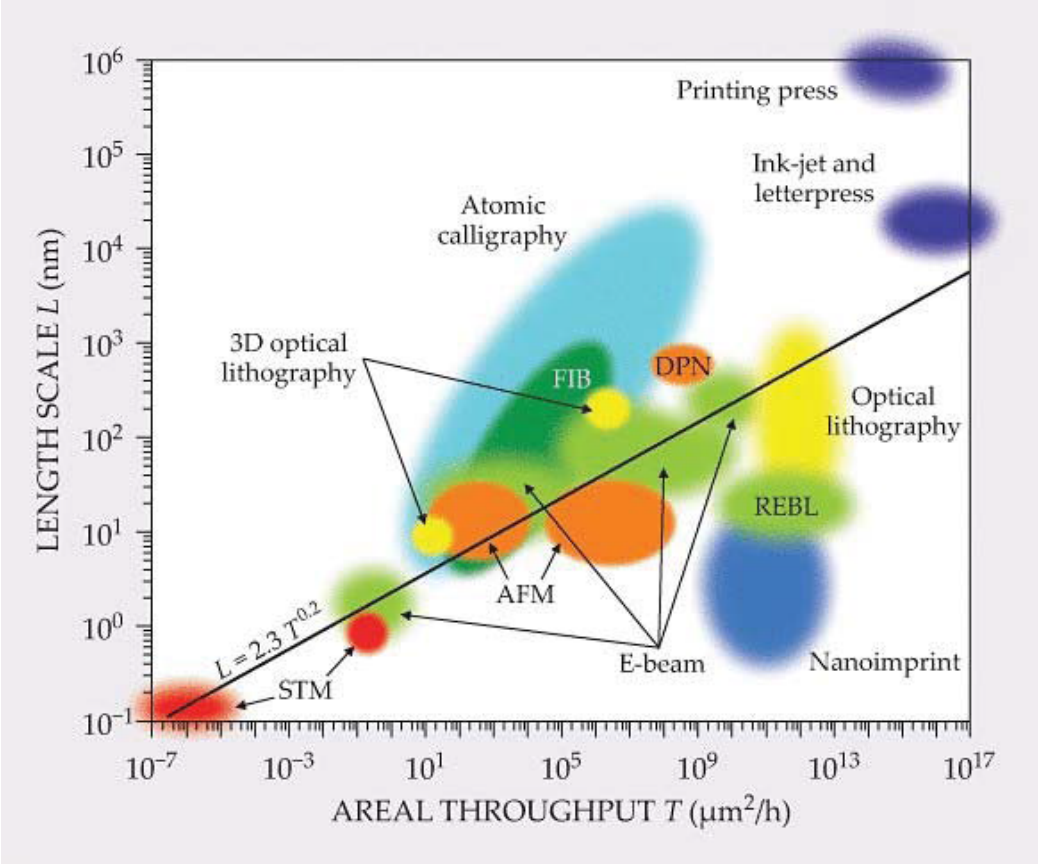

Figure 7·1: Graph of Tennant's law showing the relationship between the size of the printer materials with the speed of its printing. [Imboden et al., 2014a]

of the spectrum. Could this technology break the paradigm and shift the size and throughput relationship? Perhaps, this is a viable technology to crack the code so to speak. Nothing would prevent the MEMS technologies from being scaled from three integrated die to three integrated wafer sized components with tens of thousands of printers. This parallel processing would immensely increase the throughput. The limiting factor in this process would be the size of the aperture and how they would be created. Nevertheless, if the writer system is reusable, much as a mask in convention lithography, this approach becomes more feasible. Although this would be a natural evolution for any breakthrough technology, it may not be the most suitable for the

atomic scale 3D printer.

Each technology on figure 7·1 can be identified as an enabling technology. Here, the atomic scale 3D printer's niche is probably for researchers desiring to conduct small scale, low cost, multiple iterations fabricating samples on a variety of substrates at cryogenic or non-cryogenic environments. Ultimately, any marketable discoveries would be leveraged by industry for higher throughputs. Any scientific discoveries would probably be repeated with more precision with a lower throughput technology. This leaves us with the "what". What type problems can this technology address that capitalizes on its unique capabilities. Three specific areas can be addressed with the atomic scale 3D printer: applying patterns or circuits to existing structures, investigating combinatorial materials, and conducting superconducting quantum circuit experiments.

Connecting just the source die with the writer die as seen in figure 7·2, expands the capability of this technology. This writer/source combination can then be fixed to a different type substrate for patterning. Applying split ring resonator patterns to a meta material or the end of an optical fiber are examples of this. ([Reeves et al., 2019] Certainly, there are other existing materials which could be modified with metallic patterns that would enhance their current features. Medical and optical applications would seem an obvious fit using the two-die system since it is small and flexible enough for physically unique locations. Again, these applications would be focused at the experimental level.

One of the strong advantages of the atomic scale 3D printer is the ability to evaporate multiple metals or non-metals simultaneously or sequentially. This enabling feature

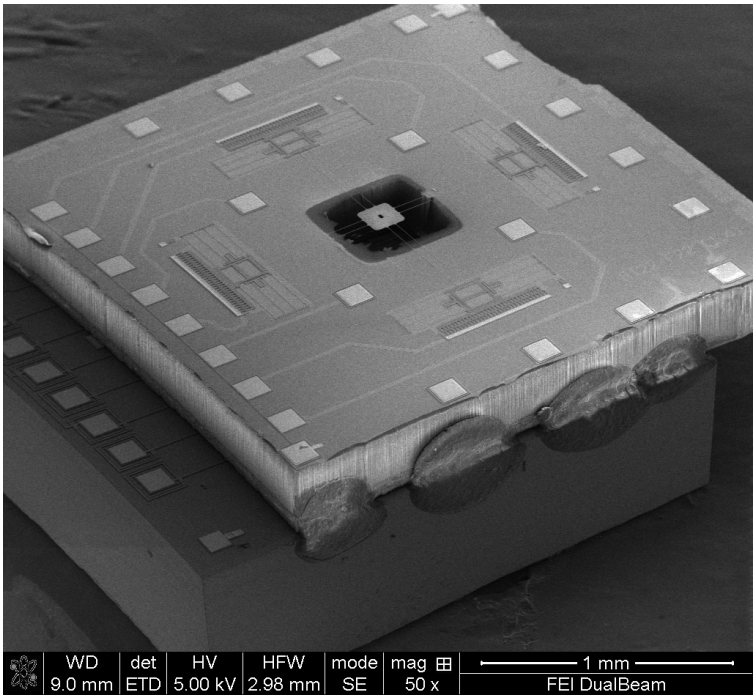

Figure 7·2: Image showing how the writer and source die can be assembled together and applied to different substrates.

provides a unique platform for 2D combinatorial materials which remain of much interest. [Xiang, 1999] Material libraries and computational material design provide insights to these materials, but experimentation must augment this capability. Many large-scale, tailored, expensive systems are employed to investigate 2D layered materials. However, most combinatorial material fabrication is not being conducted at cryogenic temperatures, which results in another distinctive role for the atomic scale 3D printer.

Lastly, and probably the most intriguing application is with superconducting quantum circuits. [Goh et al., 2022] Obviously, quantum computing is at the forefront of these applications. Creating superconducting qubits is perfectly suited for the atomic scale 3D printer. Investigating coherence loss due to materials interfaces in superconducting Josephson Junction structure would be an ideal application for this

technology. All of the enabling leads and structures for quantum computing require specific tolerances and defect purity. Again, these are areas one could develop experiments using the atomic scale 3D printer. Should one decide to modify the target die, with etched cavities or raised platforms, this would extend the range of cryogenic quantum problems that could be address with this technology.

So, we have expressed "where" this technology fits into the wide range of enabling technologies and the "how" it could have a significant impact in investigating certain problems. The "when" will hopefully be soon, so that this platform fulfills is unique niche in the nanofabrication community.

Appendix A

Supplementary information for Atomic Scale 3D Printer Assembly

A.1 Supporting Designs for Deposition

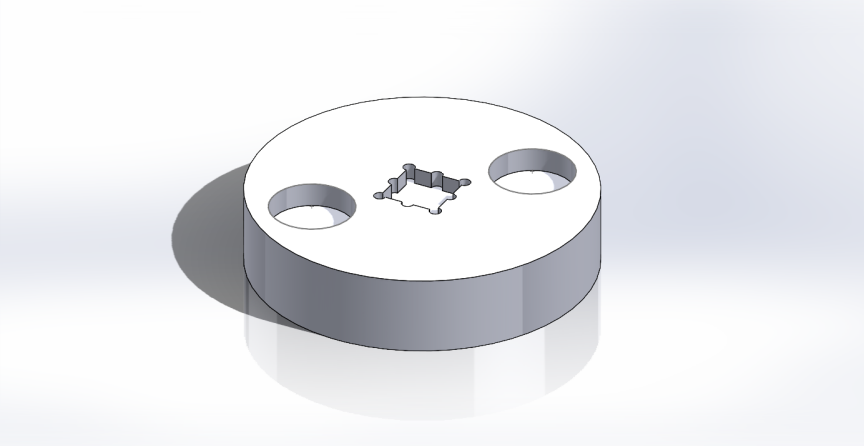

Figure A·1: Die holder designed for source die to be held in place. The source die is placed in the center opening. Two magnets are glued into the other two openings.The magnets are used to keep the Ni mask in place during alignment and deposition.

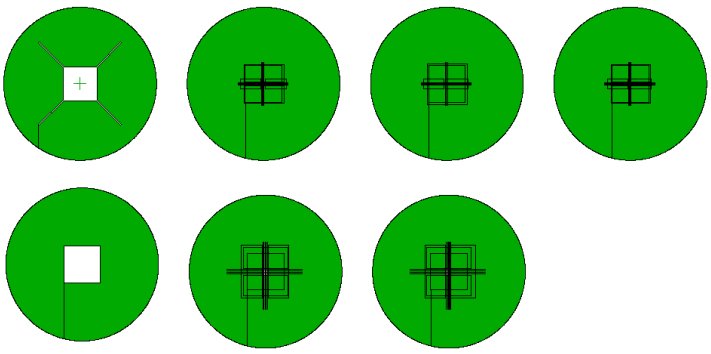

Figure A·2: Image of various Ni masks created to keep deposited materials off the bonding pads and only on the source plates. This mask is used with the holder seen above.

A.2 Connecting to the Cryostat

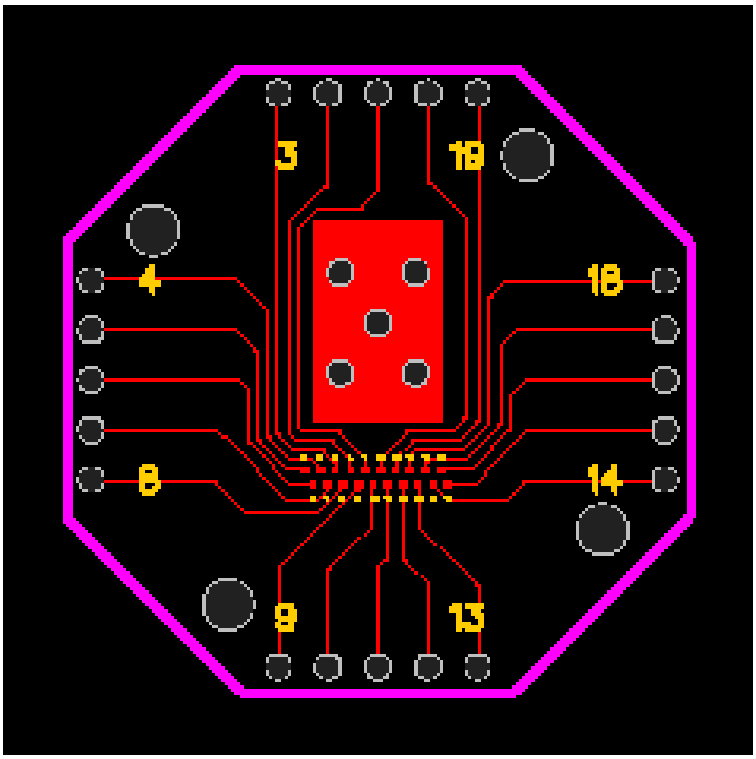

Figure A·3: Design of the PCB used to connect with the cryostat. The routing of the bonding pads allows for direct connections between all the bonding pads on the Atomic Scale 3D printer to the PCB and ultimately the cryostat feed-throughs.

A.3 Sample Sensing Diagram

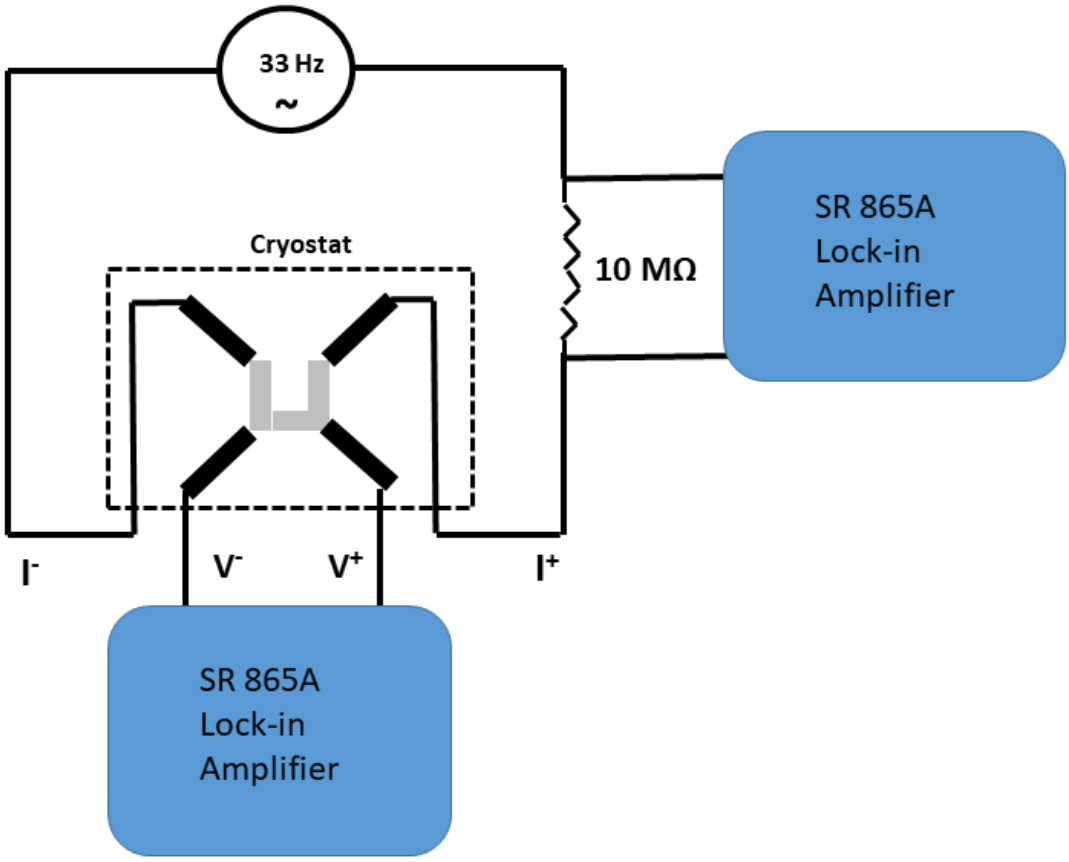

Figure A·4: Diagram shows the layout for sensing deposited sample. With the use of a 1M Ω resistor, nano amp levels of current is provided to the sample. Lock-in amplifiers are used to determine the existing current and voltage across the sample.

References

(2010). Chapter 3 - surface preparation for film and coating deposition processes. In Martin, P. M., editor, *Handbook of Deposition Technologies for Films and Coatings (Third Edition)*, pages 93–134. William Andrew Publishing, Boston, third edition edition.

Ang, X., Zhang, G., Wei, J., Chen, Z., and Wong, C. (2006). Temperature and pressure dependence in thermocompression gold stud bonding. *Thin Solid Films*, 504(1):379–383. Proceedings of The International Conference on Materials for Advanced Technologies (ICMAT 2005) Symposium H: Silicon Microelectronics: Processing to Packaging.

Barrett, L. K., Lally, R. W., Fuhr, N. E., Stange, A., and Bishop, D. J. (2020). A chip-scale, low cost pvd system. *Journal of Microelectromechanical Systems*, 29(6):1547–1555.

Barrett, L. K., Stark, T., Reeves, J., Lally, R., Stange, A., Pollock, C., Imboden, M., and Bishop, D. J. (2019). A large range of motion 3d mems scanner with five degrees of freedom. *Journal of Microelectromechanical Systems*, 28(1):170–179.

Barrow, G. M. (1953). Vapor heat capacities determined by the use of vapor pressure equations. *The Journal of Chemical Physics*, 21(11):1912–1913.

Bell, D. J., Lu, T. J., Fleck, N. A., and Spearing, S. M. (2005). MEMS actuators and sensors: observations on their performance and selection for purpose. *Journal of Micromechanics and Microengineering*, 15(7):S153–S164.

Burg, D. and Ausubel, J. H. (2021). Moore's law revisited through intel chip density. *PloS one*, 16(8):e0256245.

Chwang, R., Smith, B., and Crowell, C. (1974). Contact size effects on the van der pauw method for resistivity and hall coefficient measurement. *Solid-State Electronics*, 17(12):1217–1227.

Cowen, A., Hames, G., Monk, D., Wilcenski, S., and Hardy, B. (2011). Soimumps design handbook. *Memscap Inc*, pages 2002–2011.

Cowen, A., Hardy, B., Mahadevan, R., and Wilcenski, S. (2013). PolyMUMPs Design Handbook a MUMPs® process. *MEMSCAP Inc.*

de Leon, N. P., Itoh, K. M., Kim, D., Mehta, K. K., Northup, T. E., Paik, H., Palmer, B., Samarth, N., Sangtawesin, S., and Steuerman, D. (2021). Materials challenges and opportunities for quantum computing hardware. *Science*, 372(6539):eabb2823.

Esashi, M. (2021). Mems development focusing on collaboration using common facilities: a retrospective view and future directions. *Microsystems & Nanoengineering*, 7(1):1–9.

Ferrando, F., Zeberli, J.-F., Clot, P., and Chenuz, J.-M. (2000). Industrial approach of a flip-chip method using the stud-bumps with a non-conductive paste. In *4th International Conference on Adhesive Joining and Coating Technology in Electronics Manufacturing. Proceedings. Presented at Adhesives in Electronics 2000 (Cat. No.00EX431)*, pages 205–211.

Garcia, R., Knoll, A. W., and Riedo, E. (2014). Advanced scanning probe lithography. *Nature Nanotechnology*, 9(8):577–587.

Goh, K. E. J., Krivitsky, L. A., and Polla, D. L. (2022). Quantum technologies for engineering: the materials challenge. *Materials for Quantum Technology*, 2(1):013002.

Han, H., Imboden, M., Stark, T., Del Corro, P. G., Pardo, F., Bolle, C. A., Lally, R. W., and Bishop, D. J. (2015). Programmable solid state atom sources for nanofabrication. *Nanoscale*, 7(24):10735–10744.

Hemenger, P. M. (1973). Measurement of high resistivity semiconductors using the van der pauw method. *Review of Scientific Instruments*, 44(6):698–700.

Hołyst, R. and Litniewski, M. (2009). Evaporation into vacuum: mass flux from momentum flux and the hertz–knudsen relation revisited. *The Journal of chemical physics*, 130(7):074707.

Imboden, M. and Bishop, D. (2014). Nanomanufacturing. *Physics Today*, 67(12):45.

Imboden, M., Han, H., Chang, J., Pardo, F., Bolle, C. A., Lowell, E., and Bishop, D. J. (2013). Atomic calligraphy: The direct writing of nanoscale structures using a microelectromechanical system. *Nano letters*, 13(7):3379–3384.

Imboden, M., Han, H., Stark, T., and Bishop, D. (2017). Cryogenic Fab-on-a-Chip Sticks the Landing. *ACS Nano*, page acsnano.7b01808.

Imboden, M., Han, H., Stark, T., Lowell, E., Chang, J., Pardo, F., Bolle, C., del Corro, P. G., and Bishop, D. J. (2014a). Building a Fab on a Chip. *Nanoscale*, 6(10):5049.

Imboden, M., Morrison, J., Lowell, E., Han, H., and Bishop, D. J. (2014b). Controlling levitation and enhancing displacement in electrostatic comb drives of MEMS actuators. *Journal of Microelectromechanical Systems*, 23(5):1063–1072.

Isaacoff, B. P. and Brown, K. A. (2017). Progress in top-down control of bottom-up assembly. *Nano Letters*, 17(11):6508–6510.

Ito, T. and Okazaki, S. (2000). Pushing the limits of lithography. *Nature*, 406:1027–31.

Jesse, S., Borisevich, A. Y., Fowlkes, J. D., Lupini, A. R., Rack, P. D., Unocic, R. R., Sumpter, B. G., Kalinin, S. V., Belianinov, A., and Ovchinnikova, O. S. (2016). Directing matter: toward atomic-scale 3d nanofabrication. *ACS nano*, 10(6):5600–5618.

Judy, J. W. (2001). Microelectromechanical systems (mems): fabrication, design and applications. *Smart materials and Structures*, 10(6):1115.

Lin, L., Kollipara, P. S., and Zheng, Y. (2019). Digital manufacturing of advanced materials: challenges and perspective. *Materials Today*, 28:49–62.

Lin, Y.-J., Chiu, Y., Shih, H.-F., and Chiou, J. C. (2012). Fabrication and verification of a small-form-factor blue-light optical pickup head with holographic optical element. *IEEE/OSA Journal of Lightwave Technology*, 30:38–42.

Mamilla, V. R. and Chakradhar, K. (2014). Micro machining for micro electro mechanical systems (mems). *Procedia Materials Science*, 6:1170–1177. 3rd International Conference on Materials Processing and Characterisation (ICMPC 2014).

Moore, G. E. (2006). Progress in digital integrated electronics. *IEEE Solid-State Circuits Society Newsletter*, 11(3):36–37.

Oh, D. K., Jeong, H., Kim, J., Kim, Y., Kim, I., Ok, J. G., and Rho, J. (2021). Top-down nanofabrication approaches toward single-digit-nanometer scale structures. *Journal of Mechanical Science and Technology*, 35(3):837–859.

Park, K., Kim, N., Morisette, D. T., Aluru, N., and Bashir, R. (2012). Resonant mems mass sensors for measurement of microdroplet evaporation. *Journal of Microelectromechanical Systems*, 21(3):702–711.

Reeves, J. B., Jayne, R. K., Barrett, L., White, A. E., and Bishop, D. J. (2019). Fabrication of multi-material 3d structures by the integration of direct laser writing and mems stencil patterning. *Nanoscale*, 11(7):3261–3267.

Shakor, P., Nejadi, S., Paul, G., and Malek, S. (2019). Review of emerging additive manufacturing technologies in 3d printing of cementitious materials in the construction industry. *Frontiers in Built Environment*, 4.

Słowik, O., Orłowska, K., Kopiec, D., Janus, P., Grabiec, P., and Gotszalk, T. (2016). Quantum mechanical aspects in the mems/nems technology. *Measurement Automation Monitoring*, 62.

Stange, A., Imboden, M., Javor, J., Barrett, L. K., and Bishop, D. J. (2019). Building a casimir metrology platform with a commercial mems sensor. *Microsystems & nanoengineering*, 5(1):1–9.

Tas, N., Sonnenberg, T., Jansen, H., Legtenberg, R., and Elwenspoek, M. (1996). Stiction in surface micromachining. *Journal of Micromechanics and Microengineering*, 6(4):385.

Vazquez-Mena, O., Villanueva, L. G., Savu, V., Sidler, K., Langlet, P., and Brugger, J. (2009). Analysis of the blurring in stencil lithography. *Nanotechnology*, 20(41):415303.

Vyatskikh, A., Delalande, S., Kudo, A., Zhang, X., Portela, C. M., and Greer, J. R. (2018). Additive manufacturing of 3d nano-architected metals. *Nature communications*, 9(1):1–8.

Wasserman, J., Lucas, K., Lee, S. H., Ashton, A., Crowl, C., and Marković, N. (2008). Fabrication of one-dimensional programmable-height nanostructures via dynamic stencil deposition. *The Review of scientific instruments*, 79 7:073909.

Wen, X., Zhang, B., Wang, W., Ye, F., Yue, S., Guo, H., Gao, G., Zhao, Y., Fang, Q., Nguyen, C., et al. (2021). 3d-printed silica with nanoscale resolution. *Nature Materials*, 20(11):1506–1511.

Wu, Q., Miao, W.-s., Gao, H.-j., Hui, D., et al. (2020). Mechanical properties of nanomaterials: A review. *Nanotechnology Reviews*, 9(1):259–273.

Xiang, X.-D. (1999). Combinatorial materials synthesis and screening: An integrated materials chip approach to discovery and optimization of functional materials. *Annual Review of Materials Science*, 29(1):149–171.

Zhang, X., Sun, C., and Fang, N. (2004). Manufacturing at nanoscale: Top-down, bottom-up and system engineering. *Journal of Nanoparticle Research*, 6(1):125–130.

CURRICULUM VITAE